TECHNISCHE
UNIVERSITÄT
WIEN
Vienna University of Technology

GEOWISSENSCHAFTLICHE MITTEILUNGEN

Heft Nr. 103, 2019

VLBI Celestial Reference Frames and Assessment with Gaia

David Mayer

GEOWISSENSCHAFTLICHE MITTEILUNGEN

VLBI Celestial Reference Frames and Assessment with Gaia

David Mayer

Die Kosten für den Druck wurden vom Department für Geodäsie und Geoinformation übernommen.

Diese Arbeit wurde an der Fakultät für Mathematik und Geoinformation der Technischen Universität Wien zur Erlangung des akademischen Grades eines Doktors der technischen Wissenschaften eingereicht.

Begutachter:

Univ.-Prof. Dipl.-Ing. Dr.techn. Johannes Böhm
Department für Geodäsie und Geoinformation
Technischen Universität Wien
Gußhausstraße 27-29, 1040 Wien, Österreich

Priv..Doz.Dr. Axel Nothnagel
Institut für Geodäsie und Geoinformation
Universität Bonn, Deutschland

Dr. Sébastien Lambert
SYRTE, Observatoire de Paris, Frankreich

Tag der mündlichen Prüfung: 22.01.2019

Auflage: 10 Stück

Prüfungssenat:

Univ.-Prof.Dipl.-Ing.Dr.techn. Johannes Böhm
Technische Universität Wien

Priv.Doz.Dr. Axel Nothnagel
Universität Bonn

Dr. Sébastien Lambert
SYRTE, Paris

VLBI Celestial Reference Frames and Assessment with Gaia

Ausgeführt zum Zwecke der Erlangung des akademischen Grades eines Doktors der technischen Wissenschaften unter der Leitung von

Univ.Prof. Dipl.-Ing. Dr.techn. Johannes Böhm
E120-4
Department für Geodäsie und Geoinformation
Forschungsbereich Höhere Geodäsie

eingereicht an der Technischen Universität Wien
Fakultät für Mathematik und Geoinformation

von

Dipl.-Ing. David Mayer BSc
Matr.-Nr.: 00825543
Michalekgasse 31/1
1160 Wien

Wien, Dezember 2018

Acknowledgements

Abstract

Finding the exact positions of objects in the sky, also called astrometry, has a long tradition, which dates back thousands of years. For most of that time, the visible stars were used as reference points. However, nowadays observations are accurate enough to observe proper motions of these stars, which makes them inadequate reference points. A new type of extragalactic object, the quasar, revolutionized the field with its discovery in the 1960s. These quasars are billions of light years away, which means that they are very stable and hence the ideal reference point. They are observed with a technique called Very Long Baseline Interferometry (VLBI), which uses an array of radio telescopes to measure the accurate positions of these objects. Only a couple of decades after their discovery a catalog of quasars replaced the most accurate star catalog as recommended reference frame. For three decades the accuracy of this frame was out of reach for techniques operating in the optical part of the electromagnetic spectrum. This has changed with the Gaia satellite mission from the European Space Agency (ESA), which was launched in 2013 with the aim of mapping a billion stars with an unprecedented accuracy. Among the objects measured by Gaia are about half a million quasars with positional accuracies comparable to VLBI. For the first time in the history of VLBI a comparable celestial reference frame exists which can be used to compare positions. The aim of this thesis is to investigate the influence of different modeling and analysis strategies on the celestial reference frame estimated with VLBI. Systematic changes in the VLBI reference frame are assessed with the help of the Gaia reference frame.

Before the influence of models and analysis strategies on the celestial reference frame can be assessed a suitable solution has to be compiled. In this case the Vienna VLBI and Satellite Software (VieVS) was used to derive a catalog of source positions in X/S band with more than 4500 sources. This solution is comparable in scope and accuracy with the official International Celestial Reference Frame 3 (ICRF3) solution. It has a noise floor of about 30 μas and deformations below 15 μas with respect to ICRF3.

In order to compare two astrometric catalogs one has to find intersecting sources and calculate the difference of their coordinates. A robust approach of outlier determination has to be found and utilized. Then a suitable method to extract large-scale systematic effects from this difference scatter has to be applied. The state of the art technique used for comparing astrometric catalogs is the so-called Vector Spherical Harmonic (VSH) decomposition. It expands a vector field using orthogonal basis functions up to a certain degree using the

difference vector field of the two catalogs. The degree of expansion depends on the level of investigated detail. Since large scale systematic effects are of interest in this thesis, the expansion was stopped after degree 2. Degree 1 can be further split into a global rotation and deformation (also called glide).

Investigating large-scale systematics in the VLBI technique with the help of the Gaia reference frame revealed that certain choices made by the analyst are affecting source coordinates significantly. First, it was found that the correction of galactic aberration removes most of the glide between the VLBI and the Gaia reference frame. Second, the D_3 parameter which is directly connected to the source declination was found to be affected by many models and estimation choices. This indicates that this parameter is rather unstable, which has to do with the weak VLBI observing network in the Southern Hemisphere. Third, it was found that using ray-tracing to calculate a priori tropospheric delays succeeds in reducing the most significant VSH parameter (the $a_{2,0}^e$ parameter of degree 2) between these reference frames. In conclusion one can say that the VLBI and the Gaia reference frame do agree on a level, which will facilitate future studies about the reference points.

Kurzfassung

Mit der Entdeckung von Quasaren (extragalaktische Radioquellen) in den 1960ern wurde das Feld der Astrometrie revolutioniert. Durch die große Entfernung dieser Quellen ist die Eigenbewegung vernachlässigbar, wodurch sie zum idealen Referenzpunkt werden. Beobachtet werden diese Quellen mit der Very Long Baseline Interferometry (VLBI), welche ein Netzwerk aus Radioteleskopen benutzt um hochgenaue Positionen zu bestimmen. Nur einige Jahrzehnte nach der Entdeckung von extragalaktischen Radioquellen wurde der bis dato genaueste Sternenkatalog im optischen Frequenzbereich durch einen Katalog von Quasaren im Radiofrequenzbereich als empfohlener Standard abgelöst. Für drei Jahrzehnte war die Genauigkeit der VLBI außer Reichweite für Verfahren im optischen Bereich des elektromagnetischen Spektrums. Das hat sich mit der Satellitenmission Gaia der European Space Agency (ESA), welche 2013 gestartet wurde, geändert. Gaia wurde entwickelt um die Milchstraße zu vermessen, allerdings misst Gaia unter anderem auch Quasare mit einer vergleichbaren Genauigkeit zu VLBI. Erstmals in der Geschichte der VLBI existiert ein Referenzrahmen mit ähnlichem Genauigkeitsniveau, welcher für Vergleiche herangezogen werden kann. In dieser Dissertation wird der Einfluss von unterschiedlichen Modellen und Analysestrategien auf den VLBI Referenzrahmen mit Hilfe des Gaia Referenzrahmens beurteilt.

Bevor der Einfluss der Modelle und der Analysestrategien beurteilt werden kann muss ein VLBI Referenzrahmen geschätzt werden. Dies wurde mit Hilfe der Vienna VLBI and Satellite Software (VieVS) durchgeführt. Das Ergebnis ist ein himmelsfester Referenzrahmen mit 4500 Quellenpositionen im X/S-Band, der im Umfang und der Genauigkeit dem International Celestial Reference Frame 3 (ICRF3) gleicht. Das Rauschen dieser Lösung beträgt 30 µas mit Deformationen bezüglich ICRF3 unter 15 µas.

Um zwei astrometrische Kataloge zu vergleichen müssen idente Quellen gefunden und deren Differenz berechnet werden. Ausreißer müssen an dieser Stelle eliminiert werden und eine Methodik, um großräumige systematische Effekte aus der Differenzenstreuung zu extrahieren, muss angewandt werden. Eine geeignete Methodik um himmelsfeste Referenzrahmen zu vergleichen ist die Zerlegung in Vector Spherical Harmonics (VSH). Hierbei wird das Vektorfeld der Differenzen bis zu einem gewissen Grad in orthogonale Basisfunktionen zerlegt. Je größer der Grad der Zerlegung desto genauer kann das Vektorfeld abgebildet werden. Da hier allerdings nur großräumige Effekte von Interesse sind, wurde die Zerlegung mit Grad 2 abgebrochen. Grad 1 kann weiter in eine globale Rotation und Deformation (auch Glide

genannt) unterteilt werden.

Werden nun die großräumigen systematischen Effekte im VLBI Referenzrahmen mit Hilfe des Gaia Referenzrahmens untersucht, stellt sich heraus, dass einige Modelle und Analysestrategien die Quellenkoordinaten systematisch beeinflussen. Erstens wurde herausgefunden, dass die Korrektur der galaktischen Aberration den größten Teil der Deformationen von Grad 1 (Glide) zwischen dem VLBI und Gaia Referenzrahmen entfernt. Zweitens wurde entdeckt, dass der D_3 Parameter, welcher nur von der Quellendeklination abhängt, von sehr vielen Modellen und Analysestrategien beeinflusst wird. Das deutet auf eine schlechte Bestimmung der Deklination der Quellen hin, was mit der schlechten Verteilung der VLBI Teleskope auf der südlichen Hemisphäre zusammenhängt. Drittens wurde herausgefunden, dass a priori angebrachte troposphärische Laufzeitverzögerungen, welche mit Raytracing berechnet wurden, den hochsignifikante $a_{2,0}^e$ reduzieren können. Zusammenfassend ist zu sagen, dass der VLBI und der Gaia Referenzrahmen eine gute Übereinstimmung aufweist, was zukünfitge Studien zu Referenzpunkten ermöglichen wird.

Contents

Chapter 1

Introduction

1.1 Motivation

In 1997 the International Astronomical Union (IAU) passed a resolution, which stated that the International Celestial Reference System (ICRS) should be used as IAU celestial reference system. With this decision the astronomical community moved from a reference system, which was realized by stars to a reference system that was defined by extragalactic sources. This breaks with the long tradition of using fundamental star catalogs and was mainly driven by the need for highest astrometric accuracies.

The International Celestial Reference Frame (ICRF; a realization of the ICRS) is mainly used in the fields of astrophysics and astrometry[1], where it is utilized for studies about Active Galactic Nuclei (AGN) or stellar proper motions. However, it also plays a crucial role for geodesy where a precise Celestial Reference Frame (CRF) is needed, among others, for the exact determination of the Earth Orientation Parameters (EOP). Further, the ICRF is used for phase referencing in astronomic Very Long Baseline Interferometry (VLBI) where the compactness of the sources is exploited. The high angular resolution of VLBI is vital for spacecraft tracking where the angular distance of a spacecraft to the stable background CRF helps to accurately fly to Mars and beyond. These applications put high demands on the ICRF with the need for highest astrometric accuracy while spatial coverage should be as dense as possible. For example, spacecraft tracking needs high accuracy in the ecliptic plane, since most spacecraft move within this region. The requirements for phase referencing in astronomic VLBI comprises a dense spatial coverage because a calibrator source in near vicinity of the investigated object is desired.

The first realization of the ICRS was the International Celestial Reference Frame 1 (ICRF1), which consists of the position of about six hundred extragalactic radio sources observed by the VLBI technique. In 2009 the second realization of the ICRS, the International Celestial Reference Frame 2 (ICRF2), was published. It incorporates about 6.5 million group

---

[1]Personal communication Robert Heinkelmann

delays (VLBI observable) from 3414 sources. Since the ICRF2 was published the amount of data has doubled and about 1000 more sources were observed. At the XXVIII General Assembly of the IAU the Division A (Fundamental Astronomy) established an IAU working group with the aim to construct the next generation ICRF, the International Celestial Reference Frame 3 (ICRF3). (Charlot *et al.*, 2018) Several goals were set for the ICRF3. First, is should be completed by 2018 in order to facilitate comparison with the Gaia optical frame. Second, the accuracy should be competitive to Gaia. This means that systematic differences must be assessed and, if possible, corrected. Third, the precision should be spread more evenly among sources, which implies that dedicated observing campaigns should target sources with a small number of observations. Fourth, the spatial coverage should be improved. This implies that more observations to sources in the Southern Hemisphere should be conducted. Fifth, high frequency catalogs should be included in the published frame. Sixth, the set of sources which can be used to tie the VLBI frame to the Gaia frame should be increased.[1]

The author of this thesis worked closely with the ICRF3 working group to assess systematic errors in the VLBI frame. This was mainly realized by preparing several ICRF3 solutions with a variety of different models and analysis strategies. During the creation of ICRF2 such comparisons were conducted as well. However, at that time no independent catalog with comparable accuracy existed. Therefore, all direct comparisons had to be done using other VLBI frames. This has the obvious disadvantage that other VLBI frames are not independent since they are calculated from a similar data set using similar models. A truly independent comparison was only possible with VLBI auxiliary products, such as EOP time series and Terrestrial Reference Frame (TRF) solutions since other space geodetic techniques, such as Global Navigation Satellite System (GNSS), also deliver these products. With the publication of the Gaia Celestial Reference Frame (Gaia-CRF2) this has changed. For the first time in the history of VLBI a technique, which delivers a celestial reference frame with comparable angular resolution, exists. This provides a unique opportunity to find systematic errors in the VLBI frame, understand them and in turn correct them. Further, since the Gaia-CRF2 is not expected to experience large zonal deformations it is possible to assess the so-called declination bias, which is a systematic difference in declination found between ICRF2 and ICRF3.

1.2 Thesis outline

The primary aim of this thesis is to describe the influence of analysis choices on the CRF estimated with the VLBI technique, see Section 1.4 for a short introduction into VLBI. This is accomplished by creating CRF solutions with a variety of different models and estimation techniques, see Section 3 for a description of the analysis procedure of VLBI data. Particular emphasis is placed on models and estimation techniques, which are known to affect

---

[1]Personal communication Christopher S. Jacobs

source position, such as galactocentric acceleration, gradient estimation, a priori ray-traced tropospheric delays and many more. The rotation and deformation of the different CRFs is described using a state of the art tool for astrometric catalog comparison, the so-called Vector Spherical Harmonics (VSH) which are described in Section 4.4.2. Deformations and rotations can be assessed using a different VLBI frame, see Lambert (2014) and Ma *et al.* (2009) for example; however, this reference is never independent since they are resulting from the same technique. Nevertheless, this is how the VLBI CRFs were assessed, since no comparable frame existed until recently. With the publication of the Gaia-CRF2 reference frame a completely independent frame with a similar accuracy level (although in a different part of the electromagnetic spectrum) is available for the first time in VLBI history, see Section 1.6 for a short introduction to the Gaia mission and Section 1.7 for a description of the Gaia-CRF2. This frame is used to describe the deformations and rotations resulting from different models and estimation techniques used in VLBI analysis. Further, since this frame is independent, it is possible to find and describe systematic deformations between the techniques. The deformations and rotations between the different CRFs are discussed in Section 5.

1.3   Fundamental Astrometry

This chapter is based on Walter & Sovers (2000) and Perryman (2012).

Astrometry also known as positional astronomy is the field of astronomy that deals with the positions of celestial objects. One of the products derived with astrometry and of interest in the following chapters is a fundamental catalog of source positions. The term fundamental denotes that absolute observations are used to derive the equatorial coordinates, right ascension and declination. Historically, this is done by comparing the transit of a star across the local meridian with the transit of the Sun to derive absolute right ascension. This measurement connects the right ascension of the celestial object directly to the Sun's ephemeris, which in turn is a realization of the celestial reference system defined by the solar system. In order to compare the measurements the sidereal time has to be tracked. Absolute declinations can be estimated by observing the upper and/or lower culminations at transit time. Further, the celestial pole can be determined by observing circumpolar stars. The equator can be estimated by observing solar system bodies and relating their declinations to their ephemeris. A catalog of absolute coordinates derived with these methods (or other absolute measurement techniques) is called a fundamental catalog. An example of such a catalog is the Fifth Fundamental Catalog (FK5), see Fricke *et al.* (1988), which was the most accurate fundamental catalog until 1998.

A population of catalogs exists which have close to absolute coordinates, the quasi-absolute catalogs. An example would be a catalog, which provides absolute declination but only absolute right ascension differences. In order to relate the absolute right ascension differences to absolute right ascension external information is needed. An example for this type of catalog is a catalog derived from VLBI. The VLBI technique operates in the radio frequency spectrum

and, since useful observations in the radio spectrum of solar system bodies are generally not available, it cannot relate the measured right ascension to the celestial reference system.

The history of astrometry spans more than 2000 years with a variety of techniques. Starting with early catalogs with accuracies at about half a degree (Hipparchus) a steady increase of accuracy over the years can be observed, see Figure 1.1. It is important to note here that different versions of this diagram were published in the literature, see Høg (2017) for a detailed discussion on this diagram. The diagram used here is adopted from Walter & Sovers (2000) with the addition of Gaia (expected accuracy of brightest sources of 10 µas). It agrees well with the recommended diagram from Høg (2017). A very short overview of the milestones
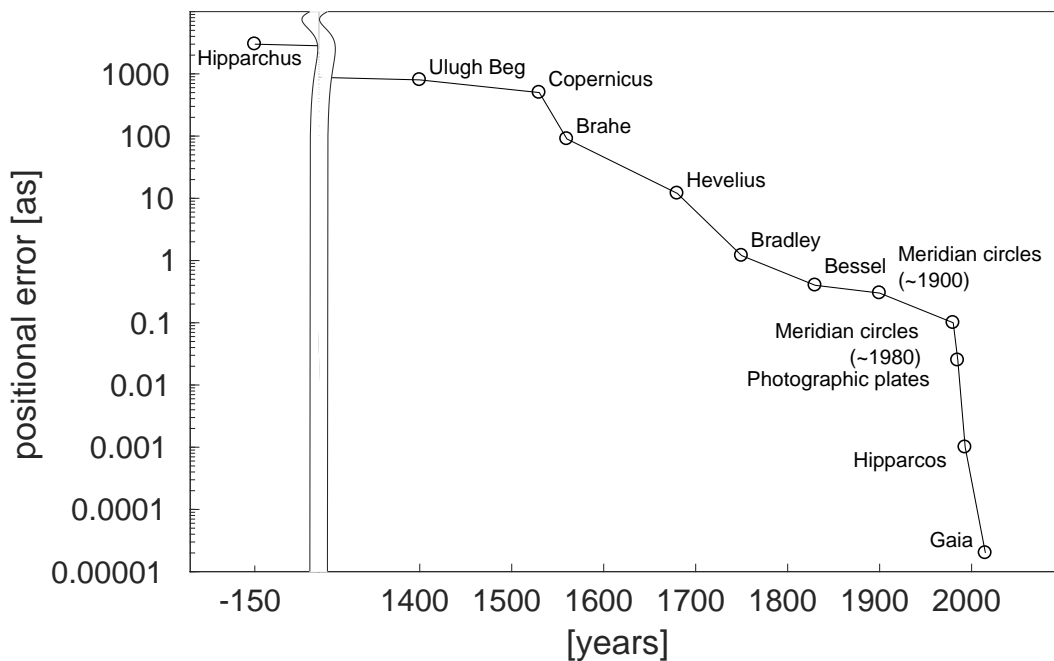
Figure 1.1: The decrease of positional errors in source catalogs with time. This figure is based on Walter & Sovers (2000) with the addition of Gaia.

in positional astronomy as depicted in Figure 1.1 is provided. For a more in depth history of astrometry the author refers to the two references stated at the beginning of the chapter. Not much has happened after Hipparchus published his star catalog around 135 BC with the first independent catalog published more than 1500 years later by Ulug Beg. Nicolaus Copernicus is known for formulating his theory on the heliocentric system. Other than that, he developed a method for the equinox determination, which provided a zero point for right ascension. Tycho Brahe who laid the foundation of Kepler's law of planetary motion achieved a remarkable jump in accuracy. Shortly after Tycho Brahe died, the optical telescope was invented (1609). After about 50 years, the instrument was regularly used in astrometry with Hevelius standing for that period. In the middle of the 17th century, the pendulum clock was invented by Huygens and shortly after the first meridian circle was built by Rømer. These instruments built the foundation of fundamental astrometry starting with Bradley and Bessel

until the end of the 20th century. The invention of photographic plates marks another milestone of positional astronomy which paved the way for yet another jump in accuracy when charge-coupled device (CCD) image sensors were sent to space (Hipparcos and Gaia satellite mission).

In the 1960s, the invention of radio interferometry and the discovery of quasars started a new chapter in astrometry. For the first time sub milliarcsecond accuracies were within reach. In 1998 the FK5 (Fricke *et al.*, 1988), which was the most accurate catalog of positions and proper motions of stars at that time, was replaced as IAU recommended coordinate system by the ICRF1, see Ma *et al.* (1998), a VLBI based catalog of extragalactic radio sources, see IAU (1999).

A new updated celestial reference frame based on VLBI data was published in 2009, the ICRF2, see Ma *et al.* (2009) and Fey *et al.* (2015). Its increase of positional accuracy can be seen in Figure 1.2. Since the population of sources published in the ICRF2 is rather inhomogeneous (most of the sources are only observed a couple of times), the median standard error of all sources would not reflect the quality of the catalog. Therefore, the standard error plotted here is calculated only from sources, which are observed in at least 10 sessions (well-observed sources). A significant improvement in accuracy from ICRF1 to ICRF2 can be observed. The standard error of the best sources (more than ten sessions) in an ICRF3 type solution is provided as well. It is evident that the accuracy w.r.t. ICRF2 increased though not as much as from ICRF1 to ICRF2. Additionally, the median standard errors of the two Gaia data releases (only the sources with ICRF3 counter parts are used to derive these values) is provided, see Gaia Collaboration *et al.* (2016b), Gaia Collaboration *et al.* (2016a) and Gaia Collaboration *et al.* (2018a). A significant increase of accuracy between the two data releases can be observed.
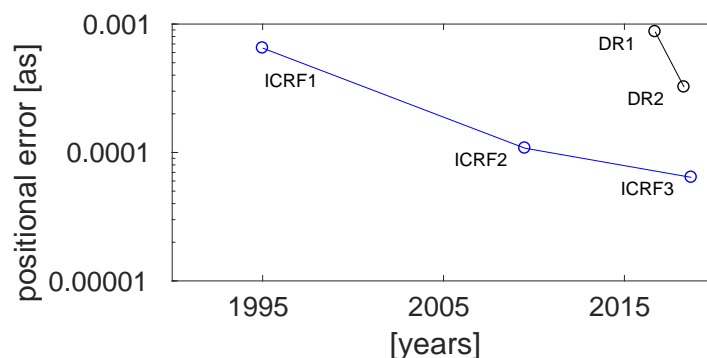
Figure 1.2: Depicted are the median standard error of ICRF1, ICRF2 and ICRF3 over time. Only sources, which were observed in at least ten sessions were used to calculate these values. The standard errors of the two Gaia Data Releases 1 (DR1) and 2 (DR2) is depicted as well. Here all the sources, which have an ICRF3 counterpart are used.

1.4   Very Long Baseline Interferometry

This chapter will introduce the technique of VLBI. The information presented here is taken from Sovers *et al.* (1998), Campbell (2000), Kellermann & Moran (2001) and Schuh & Böhm (2013). The author refers to these papers for a more detailed discussion on the subject.

Karl Jansky did first observations of the sky using a radio telescope in the 1930s with an angular resolution of 30°. The angular resolution of a telescope depends on the telescopes diameter and the observed wavelength ($\Theta_R \sim \lambda/d$). In the 1940s Grote Reber built the first radio telescope with a parabolic dish and was able to push the angular resolution to a couple of degrees by observing shorter wavelengths. Soon after astronomers used interferometry to measure the angular separation of objects on the sky. With the development of the aperture-synthesis technique, which is a type of interferometry that uses a number of telescopes to simulate a telescope the size of the collection of telescopes, the basic technique, which is still used today in VLBI, was established. First steps from antennas, which were connected by cables to truly long baselines, were realized in the mid-1960s. The accuracy of the measurement depends on the observed bandwidth which is a limiting factor for the recording system. With the development of bandwidth synthesis by Rogers (1970) in the early 1970s, which enables the reconstruction of a larger radio frequency band by observing small bands in-between, a further increase of accuracy of the measurements was achieved. With the ability to measure intercontinental distances with high accuracy, the first evidence for contemporary plate motion was rendered by Herring *et al.* (1986). Modern day VLBI plays a crucial role in observing the EOP, contributes to the International Terrestrial Reference Frame (ITRF) and constitutes the ICRF. First tests are being performed with a new generation of VLBI antennas called VLBI Global Observing System (VGOS) telescopes. These telescopes are small, very fast slewing (up to $12^o/s$) and are equipped with a broadband feed (2-14 GHz), see Petrachenko *et al.* (2009). Different frequencies can be observed with the VLBI technique. In geodesy the frequency bands S (2.3 GHz, $\lambda = 13.0cm$), X (8.4 GHz, $\lambda = 3.6cm$), K (22 GHz, $\lambda = 1.4cm$) and K_a (32 GHz, $\lambda = 0.9cm$) are of particular interest.

The geometric principle of VLBI is depicted in Figure 1.3. Two antennas marked as 1 and 2, separated by the baseline vector **b**, are pointing simultaneously at the same radio source at the position **s$_0$**. Usually more than two antennas participate in one experiment but for the sake of simplicity, only one baseline is depicted. Further, the general technique can be described with a single baseline, since adding more stations just adds more baselines, which observe in a similar manner. The radio source emits a noise signal, which, since the radio source is billions of light years away, can be assumed planar when it hits the Earth. When the wave front arrives at the first telescope the signal is digitized, recorded and time stamped using an atomic clock. After the travel time τ the wave front arrives at the second antenna and is recorded as well. The travel time τ, also called group delay, is proportional to the distance between the telescopes **b** projected in direction of the source **s$_0$** and is the fundamental observable of VLBI. Scaling the group delay with the speed of light (c) results

in the fundamental equation of VLBI, which reads:

$$\tau = \frac{\mathbf{b} \cdot \mathbf{s_0}}{c}. \tag{1.1}$$

However, before Equation 1.1 can be evaluated the baseline vector which is provided in an
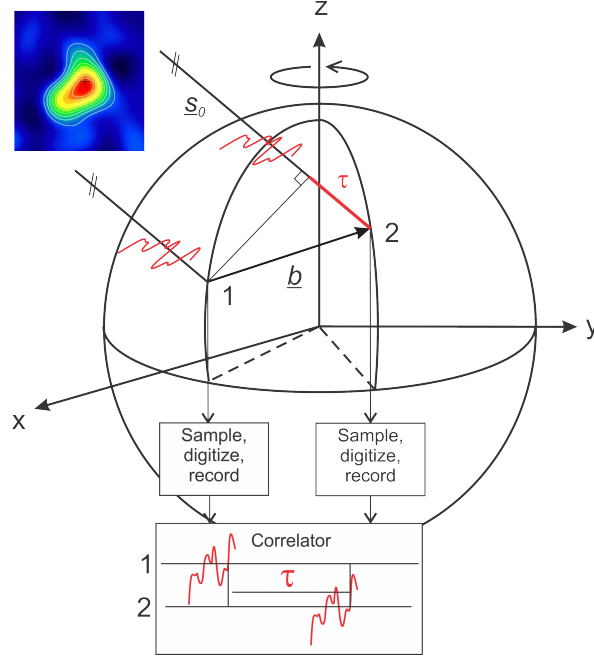
Figure 1.3: Measurement principle of VLBI. A wave front from direction $\mathbf{s_0}$ propagates to stations 1 and 2 separated by the baseline $\mathbf{b}$. The delay between the the two arrival times is denoted as τ. The signals are digitized, sampled and sent to a correlator which calculates the observable τ. This figure was taken directly from Schuh & Böhm (2013).

Earth fixed system has to be transformed into the celestial reference system where the source coordinates are provided. This transformation is realized with the five EOP and is part of the fundamental equation of VLBI:

$$\tau = \frac{\mathbf{b} \cdot \mathbf{W}(t)\mathbf{R}(t)\mathbf{Q}(t) \cdot \mathbf{s_0}}{c}, \tag{1.2}$$

where $\mathbf{W}(\mathrm{t})$ is the transformation matrix for the terrestrial polar motion (x_{pol}, y_{pol}), $\mathbf{R}(\mathrm{t})$ is the transformation matrix for the Earth's rotation around its axis $(dUT1 = UT1 - UTC)$ and $\mathbf{Q}(\mathrm{t})$ is the transformation matrix for the celestial pole which depends on precession and nutation with additional pole offsets (dX, dY). (Petit & Luzum, 2010)

Grote Reber observed a radio bright object (Cygnus A; 3C405) in the sky in 1939, which he thought to be a radio star at the time. In the 1960s, it was found that these emissions are not coming from inside our Galaxy but rather from an object far beyond the Milky Way. These objects were named quasars for quasi-stellar objects. Later it turned out that these quasars are the AGN of a galaxy. AGNs consists of a super massive black hole surrounded

by matter, which falls towards it. The disc, which forms in this process is called accretion disk. This process releases huge amounts of energy, which are discharged in electromagnetic waves across the spectrum directed perpendicular to the accretion disk in a so-called jet. The luminosity is largest and the source appears point-like when the jet is directed directly at the observer, which makes it the perfect source to use as a reference. In reality the sources are not always directly pointed at the observer, therefore, variable jet structures of the sources are part of the VLBI observable.

The network of antennas used in the VLBI technique is very inhomogeneous with a large variety of sizes ranging from 3 m to 100 m. Most antennas are constructed with a Cassegrain design but other types such as prime focus antennas exist. The mounting of the telescopes varies as well with most of the antennas being mounted in an azimuth-elevation mount, however, other mount types such as equatorial mounts do exist.

For the VLBI technique to work many calibration and data correction steps are necessary. The instrumental calibration is handled by a so-called phase calibration unit, which injects tones into the receiver with a known frequency and phase. These tones are then used to derive instrumental effects. Similar to the phase calibration some stations have cable calibration, which provides accurate information about the residual delay due to cable twisting and stretching. The ionosphere interacts with the electromagnetic signal, which travels through it. This effect can be removed by observing in two frequencies (usually X and S band) since the ionospheres effect is dispersive. Further, meteorological data (temperature, humidity and pressure) are tracked at each site. This information is later used to correct effects from the troposphere, thermal expansion etc.

Usually VLBI observations are organized in sessions where a number of VLBI stations (a VLBI network) observe together. The period of such a session is generally set to 24 hours, which helps to reduce daily effects. Since stations in a session have to observe together, an observation schedule has to be drafted beforehand. Dedicated geodetic scheduling software exists with the most commonly used one being SKED, see Gipson (2010). However, in recent years other scheduling tools were developed, see Sun *et al.* (2014) and Schartner & Böhm (2018). The aim of these software packages is to provide a schedule best suitable for the task. This means calculating all possible configurations of stations and sources (a network or sub network observing a source at a time is called a scan) and weighing them according to certain specifications. A commonly used algorithm for weighting is the so-called sky-coverage where the software prefers scans in parts of the sky that were observed infrequently. This strategy fills large holes on the sky above stations, which helps to estimate tropospheric delays in a later stage. However, other strategies such as the source-based strategy (Sun *et al.*, 2014) do exist. Scheduling is an intricate task where many parameters (such as maximum scan length, maximal slew time etc.) have to be considered. For example, a schedule, which was developed to estimate station position might not be optimal for the estimation of source position and vice versa. Therefore, the person responsible for creating the schedule has to know the scientific aims of the session in advance and has to set the parameters accordingly. An example of such

a process is provided by Mayer *et al.* (2015).

In order to derive the observable from the recorded data streams a cross correlation has to be performed. This is done at a dedicated correlator facility, which collects the data (sent via either the Internet or postal services) and correlates the bit streams. There are two types of correlators, hardware and software correlator with the latter one being used more nowadays. Software correlation is performed on a cluster (such as the Vienna Scientific Cluster) and the most commonly used software for correlation is called DiFX, see Deller *et al.* (2007) and Deller *et al.* (2011). In short, the two bit streams which represent the antenna voltages $V_1(t)$ and $V_2(t)$ as a function of time are shifted in time until their cross-correlation function R reaches a maximum:

$$R\left(\tau\right) = \frac{1}{T} \int_0^T dt V_1(t) V_2^* \left(t - \tau\right), \tag{1.3}$$

where T is the averaging interval and V_2^* is the complex conjugate of V_2. Since the Earth's rotation induces a Doppler shift in the signal, special care has to be taken to correct for that effect during the correlation procedure. The correlation process is usually executed in parallel for a number of frequency channels (usually 16 channels are used in geodetic VLBI) with each channel producing amplitudes and phases every set time (1-2 seconds) interval. This is the final correlator output, which will then be analyzed by a separate post-correlation software. The post-correlation software takes the phase samples $\Phi\left(\omega_i, t_j\right)$ for each channel ω_i and time t_j and fits a set of three parameters, the phase ϕ_0, the group delay τ_{gd} and the phase rate $\dot{\tau}_{pd}$, to it, see Equation 1.4.

$$\Phi\left(\omega, t\right) = \Phi_0 \left(\omega_0, t_0\right) + \frac{\partial \Phi}{\partial \omega} \left(\omega - \omega_0\right) + \frac{\partial \Phi}{\partial t} \left(t - t_0\right) \tag{1.4}$$

The fitting is done using a bilinear least squares fit, where the phase delay is defined as $\tau_{pd} = \Phi_0 / \omega$, the group delay is defined as $\tau_{gd} = \partial \Phi / \partial \omega$ and the delay rate is defined as $\dot{\tau}_{pd} = \partial \Phi / \partial t$. Naturally, the uncertainties of these parameters are an additional result of the fitting. The delay rate is not accurate enough to be used for geodetic analysis; however, it is still helpful in consequent analysis since it can be used to solve for ambiguities in the group delay observations, which are a side effect of the bandwidth synthesis technique. Using the phase delay proves difficult since it is affected by 2π ambiguities which are generally not known. In astronomic VLBI, these observations are utilized. However, this is only possible with a differential observing technique where a nearby calibrator source has to be observed in order to connect the phases. The amplitudes are usually not used in geodetic/astronomic VLBI. This analysis is usually (for geodetic applications) done using the fourfit[1] program. However, other software packages such as AIPS (Greisen, 2002) and PIMA[2] can be used for

---

[1] https://www.haystack.mit.edu/tech/vlbi/hops/fourfit_users_manual.pdf
[2] http://astrogeo.org/pima/

this task.

The resulting group delays can then be analyzed by the means of a parameter estimation technique such as the standard Gauss-Markow Least Squares Method (LSM) or a Kalman filter, see Soja (2016). One of the main requirements of the standard LSM is that the observation equation is linear. This is not the case in VLBI analysis; therefore, a linearization has to be performed, which is achieved by a first order Taylor expansion. In order for the Taylor expansion to deliver reasonable results accurate a priori information in the form of measurements and models have to be available. This a priori information is used to calculate the so-called theoretical delay. Effects, which have to be accounted for include geophysical effects such as solid Earth tides, station dependent effects such as thermal deformation, relativistic effects such as gravitational retardation etc. Some effects cannot be modeled and/or predicted with sufficient accuracy, which is why they have to be estimated even though they are not of immediate concern to the analyst. These effects include clock offset, clock drift and the wet part of the troposphere. More detail on the analysis of VLBI data is provided in Section 3.

1.5 The ICRF2

Information in this section is taken from Ma *et al.* (2009) and Fey *et al.* (2015), if not specified otherwise.

The second realization of the ICRS, the ICRF2, was published in 2009. It incorporates 30 years of VLBI data (4540 sessions) and provides positions of 3414 radio sources. Almost all the available data from 1979 up to March 2009 (about 6.5 million group delays) were used to derive the ICRF2. VLBI is a global endeavor, which includes many different stations, hence, the basis of networks used for the ICRF2 determination is very heterogeneous. A large amount of data (about 28%) was collected by the Very Long Baseline Array (VLBA). The VLBA is a ten-station network located in the United States of America. Its stations are equally constructed 25 m dishes, which are among the most stable instruments in VLBI. A large contribution of the VLBA to the ICRF2 are the so-called VLBA Calibrator Survey (VCS) sessions. The purpose of these six campaigns with multiple sessions (in total 24 sessions) was the densification of the reference frame as well as increasing the number of sources which can be used as phase-reference calibrators for astronomical imaging, see Beasley *et al.* (2002), Fomalont *et al.* (2003), Petrov *et al.* (2005), Petrov *et al.* (2006), Kovalev *et al.* (2007) and Petrov *et al.* (2008) for more detail. Most of the sources published in the ICRF2 are the so-called VCS sources, which means that they were only observed in these sessions. Various antennas around the globe collected the rest of the data. These antennas vary in size with the smallest at 3 m diameter and the largest at 100 m diameter.

Unfortunately, most of the VLBI antennas are located on the Northern Hemisphere. Which is why the sources on the southern celestial sphere are less observed. Further, the sources in the south are mostly observed by northern stations which results in bad observational geometry

(many low declination scans). When the distribution of sources is plotted on the celestial sphere the lack of southern sources is immediately eminent, see Figure 1.4. As mentioned above the majority of sources in the ICRF2 are observed only in the VCS sessions by the VLBA. This is also the reason why the density of sources is much lower below about -40° declination since this is about as far south as the VLBA can observe.
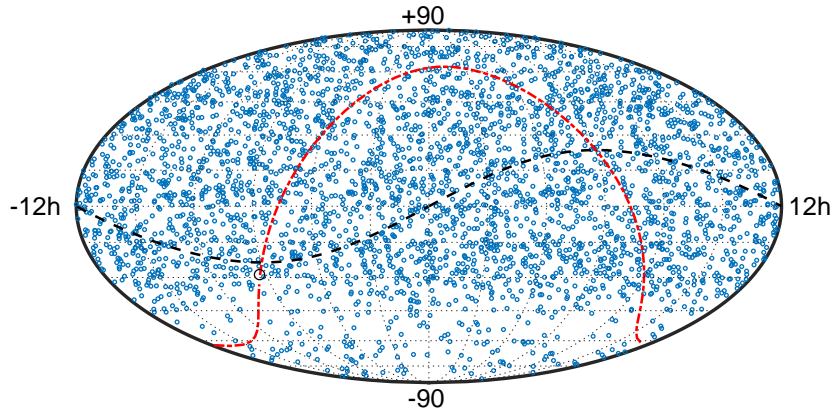
Figure 1.4: Distribution of 3414 sources, which were published in ICRF2. The galactic plane is depicted in red with the center of the Galaxy denoted as a black circle. The ecliptic is depicted as a black dashed line.

The software used to determine the ICRF2 is CALC/Solve, see Ma *et al.* (1986) for more details on the analysis methods. A combination with other solutions using different analysis software packages was envisaged but in the end, it was decided to provide only the solution made by the Goddard group using CALC/Solve. However, the other software packages were used to validate this solution.

In general, the geophysical modeling and precession/nutation for the ICRF2 follows the IERS conventions (2003), see McCarthy & Petit (2004). The troposphere was modeled using the Vienna Mapping Function 1 (VMF1), see Böhm *et al.* (2006), atmospheric pressure loading was corrected according to Petrov & Boy (2004), and antenna thermal deformation was corrected with Nothnagel (2009).

Data was weighted in each session separately by iteratively adding noise per baseline to the uncertainties from the correlator output until the χ^2 factor of each baseline is close to unity.

When setting up a global solution one has to decide which parameters to reduce (the so-called arc parameters) and which parameters to estimate (the so-called global parameters). More detail on the general geodetic data analysis procedure can be found in Chapter 3. The global parameters estimated in the ICRF2 are source positions as well as station positions and velocities. Additionally, antenna axis offsets are estimated as global parameters. In each session, the following arc parameters were estimated:

- Clocks as quadratic polynomial function in addition to Piece-Wise Linear Offsets (PWLO) every 60 minutes,

- Station wet troposphere as PWLO with zenith wet delays every 20 minutes and gradients every six hours with a priori gradients from MacMillan & Ma (1997),

- dUT1 and polar motion once per session with offset and rate at the midpoint of the session and nutation as one offset at the midpoint of the session and

- 39 special handling sources.

Some sources were not included into the ICRF2. For example, radio stars which experience proper motion or gravitational lenses, which have more than one component. Another population of sources, which are not directly included in the ICRF2 solution are the special handling sources. With the help of source position time series the most positional unstable sources were selected as special handling sources. This means that they are not estimated as a global parameter but rather as an arc parameter estimating one position per session where it was observed. The average and the Weighted Root Mean Square (WRMS) of the resulting positions can then be used as position and formal error of these sources.

When estimating source coordinates in a global adjustment the station positions can be either treated as global parameters, this is called the TRF type solution, or as arc parameters (this is called a baseline type solution). In order to keep consistency with the corresponding ITRF solution and EOP time series a TRF type solution was chosen for the ICRF2. This means that the station positions and velocities were estimated as global parameters and the EOP were estimated per session.

The resulting formal uncertainties from the ICRF2 solution were scaled by 1.5 and a noise floor of 40 µas was added. These values can be calculated from two independent solutions, see Section 3.1.2 for more information. The distribution of the formal uncertainties of ICRF2 is depicted in Figure 1.5. Smaller errors are found in right ascension than declination with
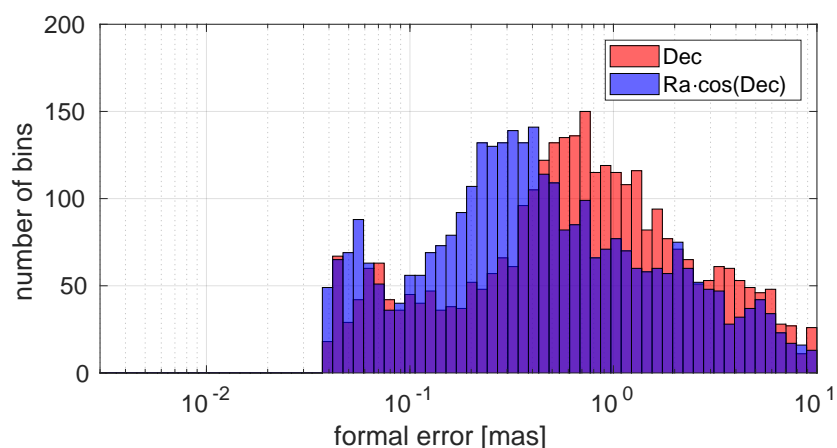
Figure 1.5: Distribution of formal uncertainties in ICRF2. The limits of the x-axis are deliberately kept consistent with Figure 1.13 and 5.2 in order to facilitate comparisons.

median formal uncertainties of 397 µas and 739 µas respectively.

Several other tests were performed by the working group to investigate the impact of different models, data sets and analysis strategies. It was found that the impact of these changes was well within the estimated noise floor.

The ICRF2 was not evaluated directly because at that time there was simply no astrometric catalog with comparable accuracy. However, ICRF2 was evaluated using auxiliary products which were estimated alongside ICRF2, namely the TRF and the EOP. The polar motion was compared against a time series provided by the International GNSS Serivce (IGS), but the dUT1 and nutation series were compared against other VLBI solutions since no other techniques are able to estimate these parameters. It was found that the overall agreement is on the 100 µas level. The TRF which was estimated alongside the ICRF2 was rotated onto a reference TRF, the VLBI Terrestrial Reference Frame 2008 (VTRF2008), see Böckmann *et al.* (2010), using a Helmert transformation. The orientation w.r.t. VTRF2008 was found to be within about 40 µas with a rate of a few µas per year.

Additionally, the astrometric quality of as many sources as possible was estimated. This was done using the so-called structure index (SI), see Fey & Charlot (1997). The SI is calculated by deriving the expected magnitude the intrinsic source structure has on VLBI group delay measurements. An algorithm to derive the SI is described in Charlot (1990). The median values of structure delay corrections for all possible VLBI baselines, τ_{median} are calculated and then the SI is calculated using Equation 1.5.

$$SI = 1 + 2\log\left(\tau_{median}\right) \tag{1.5}$$

The VLBI data set is very inhomogeneous with some sources barley observed while others are observed in almost every session. In order to get the most stable frame possible it is desirable to select only the best sources to define the axes and use the rest for densification. For the ICRF2 a first selection was done using a time series of source positions to calculate the positional stability as well as the formal uncertainty derived from the global solution. These values are combined with a method described in Fey *et al.* (2001) to come up with a list of stable sources. This list was further reduced by introducing a threshold for SI of three. In the end, 295 sources remained. These sources were used to define the ICRF2.

The ICRF1 (as realized by ICRF-Ext.2) was used to rotate the ICRF2 onto the ICRS. This was done using 138 common sources between these catalogs. Care was taken to use only rotations in order to avoid transferring deformations onto the ICRF2. Using different subsets of sources the axis stability was estimated to be around 10 µas.

1.6   The Gaia mission

This chapter is based on Gaia Collaboration *et al.* (2016b) and Lindegren & Bastian (2011), For more detail on the Gaia mission the author refers to these papers and the references therein.

Gaia is a satellite mission by the European Space Agency (ESA) with the aim of mapping the Milky Way galaxy. It is the successor to the Hipparcos satellite (ESA, 1997), which was launched in 1989 and operated until 1993. The Hipparcos satellite measured the positions of about 100,000 stars and was the first space instrument dedicated to astrometry. Gaia was approved in 2006 and the Gaia satellite was launched on the 19th December 2013. It operates from the second Lagrange point where it is orbiting the Sun at the speed of the Earth. The Lagrange points are five points in a two-body system where a small (satellite, asteroid etc.) third body can circle the more massive body with the same period as the lower mass body. Satellites at one of these points are very stable and do not change position relative to the lower mass body. From there Gaia measures absolute parallaxes and transverse kinematics, effectively measuring the three-dimensional position and two-dimensional velocity of objects in the solar system. Additionally, Gaia will determine the radial velocities, completing the kinematic information, and photometric properties of a subset of target sources.

Gaia, as its predecessor Hipparcos, is part of a new field of astrometry called scanning space astrometry. It relies on slowly rotating (60 as/s) the satellite and using an array of CCD cameras to record the time of passing objects. Gaia collects one dimensional measurements along-scan (AL) of the source position w.r.t. the instruments axes. Across-scan (AC) position measurements are collected as well. However, for various reasons these are not as accurate as along-scan measurements. This is not of great concern, since these observations do not contribute much to the position accuracy. Collecting mainly one-dimensional information from a two-dimensional astrometric field seems to be odd at first, however, when looking at Figure 1.6 it becomes clear that the AC measurement is not distinguishable from a tilt of the instrument around the x and y-axes.
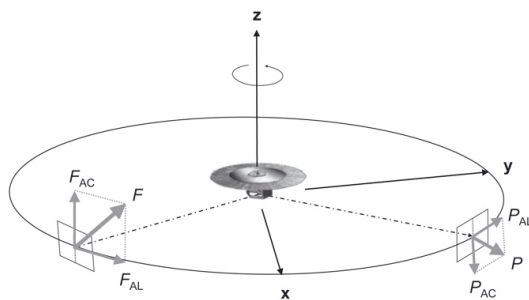
Figure 1.6: Positional errors in AC and AL directions for preceding (P) and following (F) fields. While the difference $P_{AL} - F_{AL}$ contains useful information the AC difference $P_{AC} - F_{AC}$ is mixed with attitude errors around the x and y-axes. This image was taken from Lindegren & Bastian (2011).

Gaia is equipped with two fields of view, which are projected onto the CCDs simultaneously. These two fields of view are separated by the basic angle Γ, for Hipparcos this angle was defined to be $\Gamma = 58^o$ and for Gaia it was set to $\Gamma = 106.5^o$. Since Gaia is rotating around its rotation axis (z) it observes consecutive great circles. It was found that the accuracy of the determination of the one-dimensional observable depends on the choice of Γ with

$\Gamma = 360^o \cdot (m/n)$ being a bad choice for small integers of m and n. This effect disappears when a global solution of the whole celestial sphere is conducted. However, waiting for a global solution deprives the analyst of a valuable great-circle solution, which can be calculated from just one day of data and provides a good indication of data quality. This is also the reason why the theoretically best value (more on that will be discussed later) of 90° (a simple fraction of 360°) was not used. Other values which were found to be suitable are 99.4^o and 106.5^o with the latter one being chosen for instrument design purposes.

One of the aims of Gaia is to build a global consistent reference frame. Lindegren & Bastian (2011) defined this by stating that in a global consistent reference frame the uncertainty of a measured angle α between any two points at any time should be roughly independent of the size of α. Astrometry with a small field of view does not fulfill these conditions since piecing together a reference frame from small pieces is prone to systematic zonal errors. Therefore, as mentioned before, two fields of view separated by a large angle (basic angle) are implemented. These fields are projected simultaneously on the same CCDs effectively relating small measured time differences on the CCD between sources from different field of views to large arcs on the sky. Additionally, using two fields of view allows Gaia to measure absolute parallaxes. Parallaxes are a way of estimating distances in astronomy by changing the position of the observer and measuring the positional change of the object that is observed. The larger the parallax (positional change of the object) the closer the object. In classical astrometry with small fields of view, only relative parallaxes can be measured. The reason for this is that by definition the parallactic displacement d of a star at distance r is dependent on the angle of the star from the sun Θ, see Equation 1.6.

$$d = \frac{R \sin \Theta}{r}, \tag{1.6}$$

with R being the distance of the observer from the Sun. For an observer 1 AU from the sun and the small angle approximation of parallax measurement ($\varpi = \frac{1}{r}$) the equation can be simplified to

$$d = \varpi \sin \Theta, \tag{1.7}$$

with ϖ being the parallax angle. Note that d is in arcseconds. In a small field of view, the factor $\sin \Theta$ is almost the same for all stars that can be seen. Therefore, one can only relate the parallax of a star to the background stars measuring a relative parallax. Gaia, makes relative measurements as well, however, since it can measure relative shifts of widely separated stars it can obtain absolute parallaxes. In Figure 1.7 the measurement principle of Gaia is depicted with its F and P fields and the solar aspect angle ξ. Applying the sine rule of spherical trigonometry to the triangle $Fz\odot$ reveals Equation 1.8.

$$\sin \Theta = \frac{sin \xi \sin \Gamma}{\sin \Psi} \tag{1.8}$$
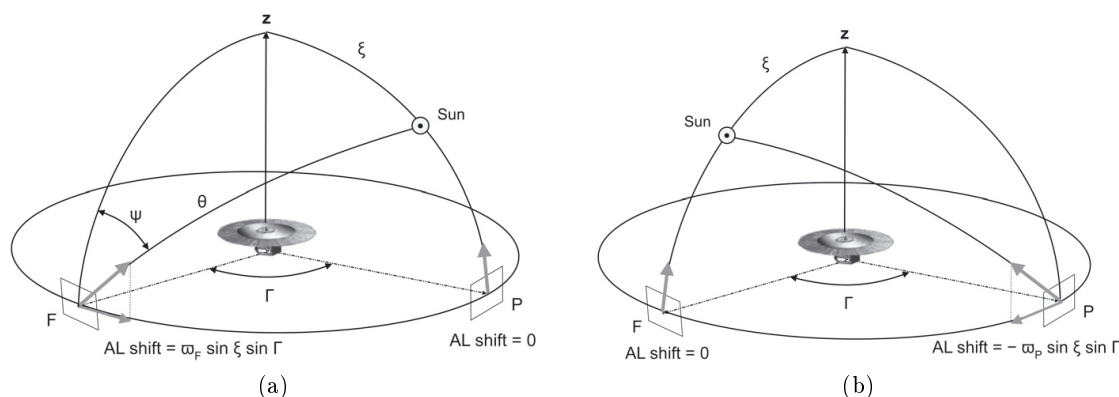
Figure 1.7: Absolute parallax measurement principle. The large angle measured AL between stars at the P and F fields depends on their parallaxes ϖ_F and ϖ_P times the sine of the position of the Sun. In the left part of the figure the apparent shift due to parallax only depends on ϖ_F and the reverse (apparent shift only depends on ϖ_P) is true for the right part of the figure. This allows for the determination of the absolute parallax rather than the relative parallax which would be $\varpi_P - \varpi_F$. This figure was taken directly from Lindegren & Bastian (2011).

Eliminating $\sin\Theta$ with Equation 1.7 and 1.8 reveals Equation 1.9 for the F field.

$$d\sin\Psi = ALshift = \varpi_F \sin\xi \sin\Gamma \tag{1.9}$$

At the same time at field P the AL shift is zero, therefore, the relative AL measurement from F and P depends only on ϖ_F and not on ϖ_P. The reverse is true for a different point in time, see right part of Figure 1.7. This is how absolute parallaxes can be determined. Equation 1.9 reveals that the sensitivity of the parallax is proportional to $\sin\xi \sin\Gamma$. Naturally, these should be designed to be maximized. Certain constraints have to be considered when choosing these values. First, the ideal value for Γ would be 90°, however, this is not what was chosen (reasons for this are discussed above). Second, ideally ξ should be 90° as well, however, this would mean that the Sun would enter the field of view at every rotation of the satellite, which is unacceptable for various reasons. The amount of acceptable stray light of the Sun and the size of the Sun shield are practical constraints for this factor with the best trade-off found to be a solar aspect angle of $\xi = 45^o$.

The measurements themselves are taken using an array of CCDs. In total, the focal plane used by Gaia contains 106 CCDs with about a billion pixels, which makes it the largest camera ever flown in space. In Figure 1.8 a sketch of the focal plane used on-board Gaia is depicted. Each pixel is $10\mu m \times 30\mu m$ in AL and AC direction respectively, which corresponds to $58.9mas \times 176.8mas$ on the sky. Three different types of CCD are used on-board Gaia, the AF-type, which are optimized to cover a broad band of frequencies, the BP-type, which are optimized for short wavelengths and the RP-type, which are optimized for long wavelengths. Two CCDs are used as Wave-Front Sensor (WFS) which measures the optical quality of each telescope. The basic angle is monitored with another set of two CCDs, the so-called Basic

Angle Monitor (BAM). Astrometric measurements are performed by the 62 CCDs, which make up the astrometric field (AF). In order to deal with the enormous data volumes only the pixels relevant to the passing object are read out, this procedure is called windowing. This can only be performed with knowledge of the location of passing objects. For Hipparcos this was realized by an a priori catalog, which was previously loaded. However, this approach cannot be used for Gaia since a catalog with such a high spatial resolution down to a magnitude of 20 simply does not exist. Therefore, Gaia has to select the objects to follow autonomously. This is realized with the so-called sky mappers (SM) which consist of two columns of seven CCDs each for one field of view. The sky mappers select the objects, which should be followed by the AF. Therefore, Gaia performs an unbiased survey of the sky, which is only limited by the objects flux. The wavelength observed by the AF is the white-light photometric G band, which ranges from 330 to 1050 nm. In the AF, the sources are observed in time-delay integration mode, which means that images of objects crossing the CCD are continuously integrated. After each CCD crossing, the image data and timing are read out and saved for further processing. Objects that passed through the AF are then observed (the spectral
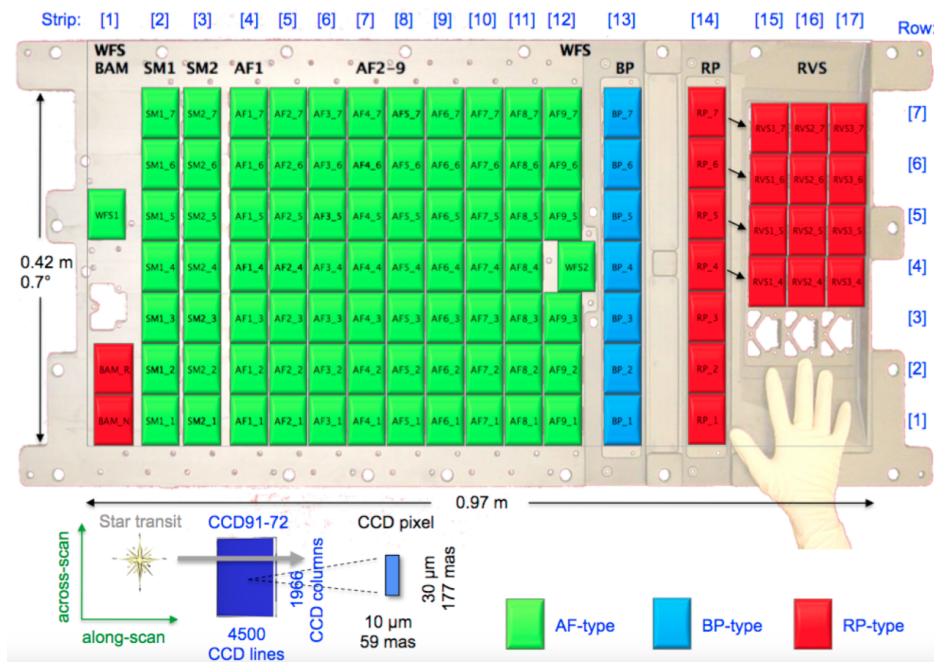
Figure 1.8: Sketch of the focal plane on-board Gaia. The different types of CCDs are depicted in different colors and their different functions are denoted with abbreviations and a numbering scheme. The scale is indicated by length information; in addition, a human hand is depicted. In the lower part of the figure, the pixel size is depicted. This figure was taken directly from Gaia Collaboration *et al.* (2016b).

energy distribution is observed) by the photometric instrument at the same angular resolution. This is done by two columns of CCDs, one sensitive to short wavelengths (BP-type; 330-680 nm) and one sensitive to long wavelengths (RP-type; 640-1050 nm). On the one hand, the photometric instruments provide astrophysical information of all objects, which can be used

for the classification of objects types (star, quasar etc.) and characterization (photometric redshift, effective temperature of stars etc.). On the other hand, this information can be used to correct for optical aberration of the telescope. A bright subset of sources observed by the AF are then observed by the spectroscopic instrument (Radial-Velocity Spectrometer - RVS) which delivers, among others, radial velocities of sources.

Gaia's telescope is not steerable; therefore, the whole satellite has to move to produce observations of the whole celestial sphere. The way this movement is designed is the so-called scanning law. The aim of the Gaia scanning law is the optimization of the sky coverage over the nominal five-year mission time. Gaia rotates with a fixed spin rate of 60 as/s, which assures that objects cross the focal plane with a constant speed, see Figure 1.9. As discussed before
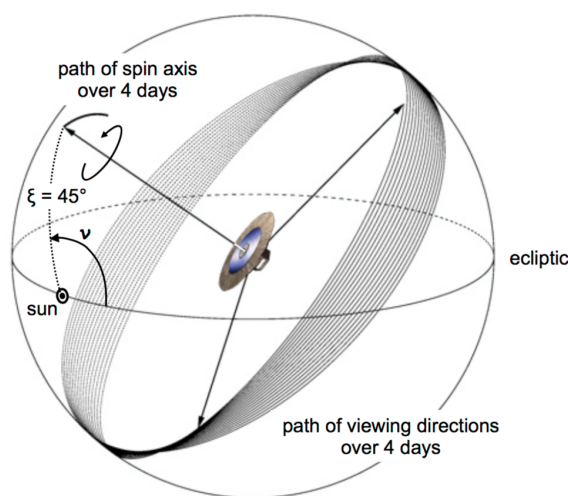
Figure 1.9: Depicted is the scanning law of Gaia over the duration of four days. During these four days the Gaia satellite rotates 16 times, observing sources along the consecutive great circles depicted in grey. For clarity reasons the path of the F viewing direction is not shown. This figure was taken directly from Gaia Collaboration *et al.* (2016b).

the solar aspect angle of the rotation axis is fixed to 45° which is a trade-off of parallactic sensitivity and thermal stability. Additionally, the spin axis describes a precession around the Earth Sun direction with 5.8 revolutions per year (63 days). When the path of the spin axis is plotted on the celestial sphere one can see that it follows a series of loops around the Sun's direction, see Figure 1.10.

An object at position a is observed each time the angle between it and the spin axis z is 90° which is denoted as the great circle A. Looking at Figure 1.10 it becomes evident that these scans intersect at a large angle which makes the determination of the two-dimensional coordinates from one-dimensional observations possible. The speed of the precession is chosen to be as small as possible since it introduces an across-scan smearing effect. However, at the same time it must be large enough to ensure a sufficient observing geometry (loops have to intersect). Figure 1.11 depicts what would happen, if the precession is chosen too small (loops do not intersect). Source a, which would be observed three times in Figure 1.10, is only observed once in Figure 1.11.
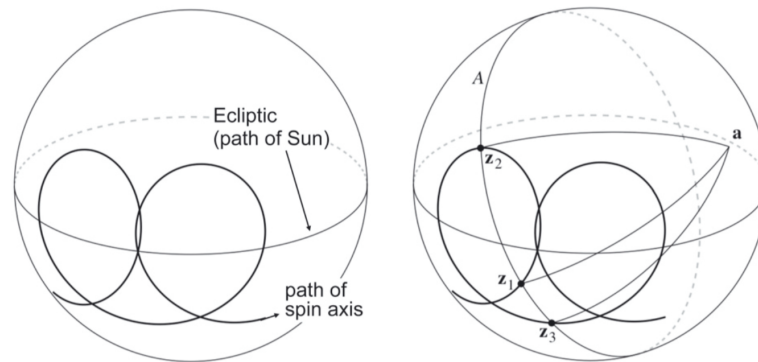
Figure 1.10: The path of the spin axis z describes loops around the Earth Sun direction. A source at position a is observed when the angle between a and the spin axis becomes 90°, which is denoted as the great circle A. This happens at positions z_1, z_2 and z_3. This figure was taken directly from Lindegren & Bastian (2011).
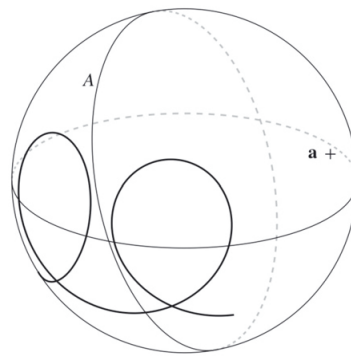
Figure 1.11: When the loops of the rotation axis do not intersect (precession is too slow) a great circle A can be drawn with only one observation. This resembles a poor observational geometry. The figure depicted here was taken directly from Lindegren & Bastian (2011).

It is planned that the Gaia data is published in several intermediate releases with the current one being the Gaia DR2. The Gaia data is freely available without limitations and can be downloaded from the Gaia archive [1].

1.7 The Gaia-CRF2

The content of this chapter is derived from three papers about Gaia and its second data release, they are Gaia Collaboration *et al.* (2018a), Lindegren *et al.* (2018) and Gaia Collaboration *et al.* (2018b).

The Gaia camera tracks all objects of a certain brightness, which pass through its field of view. Among these objects also extragalactic light sources are found, usually quasars. Gaia provides positions to quasars some of which are observed by VLBI. The position of these quasars is published alongside the other Gaia data.

---

[1] https://gea.esac.esa.int/archive/

On the 25th of April 2018 the second Gaia data release was made available to the public. The position and brightness of 1.7 billion sources was published. From these sources, about half a million are quasars. The Gaia DR2 solution was created in two steps with a primary and secondary solution. In the primary solution, the astrometric parameters of selected primary sources were calculated and in the secondary solution, the astrometric parameters of all sources were calculated using the attitude and calibration from the primary solution. Within the primary solution, the quasars were used to keep the astrometric parameters and attitude in the ICRS. This is done using the so-called frame rotator, see Lindegren *et al.* (2012) for more information. In order to do this the quasars were divided into two groups. First, about 3000 sources were identified to have a counterpart in the ICRF3 (a preliminary ICRF3 solution was provided by the ICRF3 working group). These were used for the orientation of the frame because they have the most accurate positions available to date. Second, the majority of quasars were found by cross matching with the ALLWISE AGN catalog (Secrest *et al.*, 2015). This homogeneous set of quasars as well as the ones cross-referenced from the ICRF3 were used to ensure that the frame is globally non-rotating (spin of the frame). The positions and uncertainties of half a million quasars are the first realization of the ICRS in optical wavelengths. The increased accuracy of the final DR2 was used once more to find matching quasars in the data set. In the end a total of 556869 quasars were found with 2820 having an ICRF3 counterpart. These quasars make up the non-rotating global reference frame, which is called the Gaia-CRF2.

Figure 1.12 depicts the spatial distribution of the 2820 quasars that have an ICRF3 counterpart. The density becomes sparser the closer the sources are to the galactic plane, which
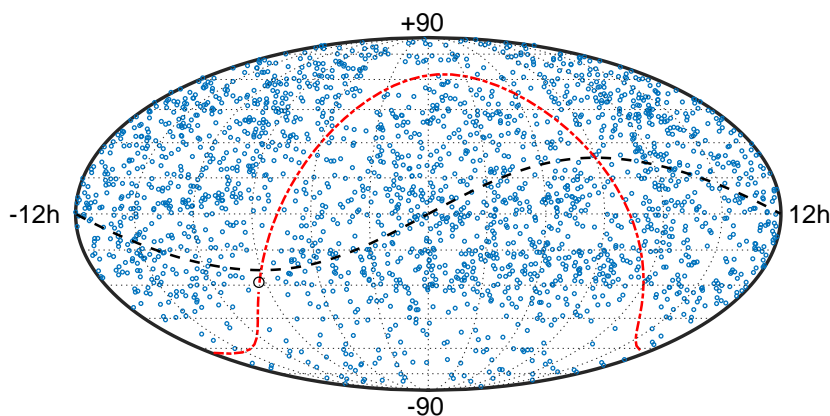
Figure 1.12: Distribution of 2820 Gaia sources with an ICRF3 counterpart. The galactic plane is depicted in red with the center of the Galaxy denoted as a black circle. The ecliptic is depicted as a black dashed line.

is due to the effects of Galactic extinction. Similar to the ICRF the southern sky has much less sources than the northern sky, which is an imprint of the sky distribution of the ICRF.

The distribution of formal uncertainties of the 2820 quasars that have an ICRF3 counterpart is depicted in Figure 1.13. It follows a bell curve with average formal uncertainties at

233 µas (scaled with $cos\delta$) in right ascension and 211 µas in declination.
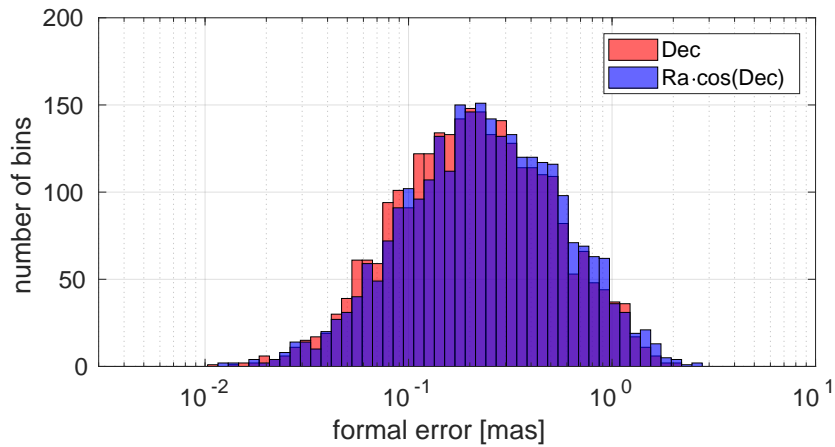
Figure 1.13: Distribution of formal uncertainties in Gaia.

Looking at the distribution of magnitudes, see Figure 1.14, one can see that the sources in this data set are rather faint with a median magnitude of 18.8.
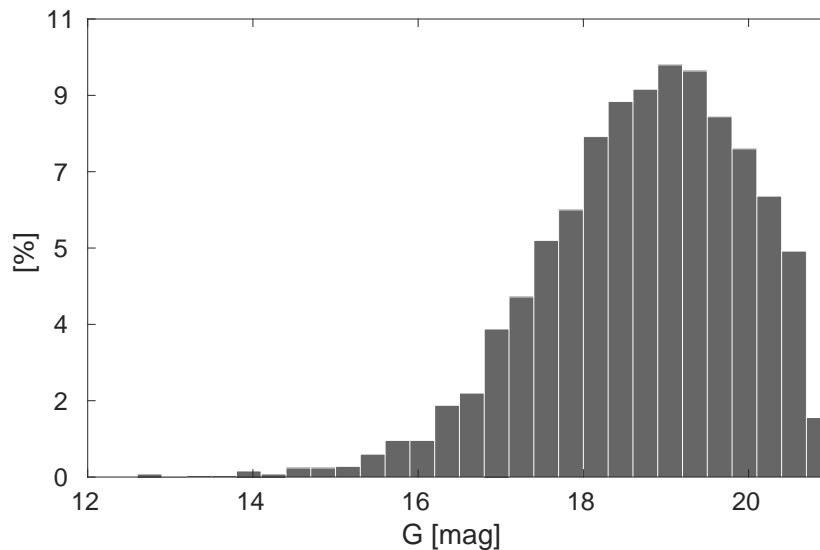
Figure 1.14: Distribution of magnitudes of the 2820 Gaia sources with an ICRF3 counterpart. The median magnitude is 18.8.

We can use the length of the semi-major axis of the error ellipse of a source to get one value for the positional accuracy. When this value is plotted against the magnitude of the sources a dependency of astrometric quality on magnitude of the source can be observed, see Figure 1.15. This is not new and was already reported by the references mentioned in the beginning. However, Figure 1.15 demonstrates that, as expected, Gaia measures bright objects more accurately than faint ones.
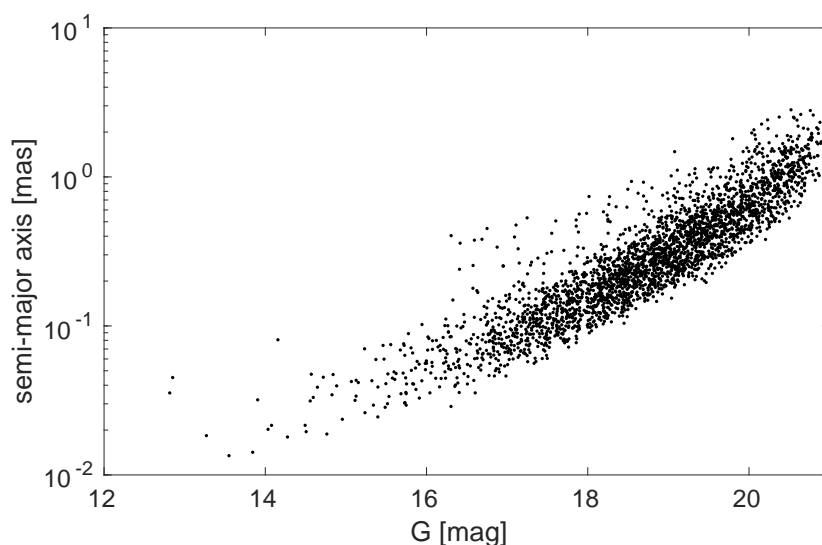
Figure 1.15: Scatter of magnitudes versus length of semi-major axis of error ellipse of the 2820 Gaia sources with an ICRF3 counterpart. A trend is clearly visible with brighter sources having smaller errors.

1.8 Offsets between Gaia and VLBI positions

Mignard *et al.* (2016) was the first to compare optical positions from Gaia to radio positions from VLBI. They got the VLBI positions from the ICRF2 and compared them to positions from the quasar auxiliary solution, which is part of Gaia DR1. They found 2191 matching sources and used the normalized separation (this is favorable to the angular distance since it incorporates the correlation between right ascension and declination) to calculate the difference between them. The overall agreement was found to be very good with about 6% of sources having statistically significant offsets. Some of these deviating cases were explained by false detections, large glare around images etc.

Petrov & Kovalev (2017) repeated the comparison based on normalized separation with a much larger and more recent VLBI solution. In total, they used 11,444 radio sources from several sources and found 6064 matches with Gaia DR1. They report a similar figure of 6% statistically significant offsets. Further, they report on the deviation of the distribution from a Rayleigh distribution. It was found that the majority of sources with statistically significant offsets are most likely not from oversight in VLBI quality control and must be, therefore, genuine radio optical offsets. Three explanations for these genuine radio optical offsets are provided. First, the emission core might be frequency dependent, see Lobanov (1998) and Kovalev *et al.* (2008). Second, unaccounted source structure can offset the radio position. Third, some galaxies are optically weak and host a bright radio star, see Condon *et al.* (2017).

Kovalev *et al.* (2017) determined jet directions of 2957 AGN from VLBI images. They showed that the offsets between Gaia and VLBI favor the direction of the jet. Further, they conducted Monte Carlo simulations and concluded that these offsets cannot be caused by extended frequency-dependent radio structure, which suggests the existence of elongated

optical jet structures.

Petrov & Kovalev (2017) claim that the position delivered by Gaia is more susceptible to the structure of optical jets than the VLBI position. They conclude that the presence of optical structures on the level of 1-2 mas due to relativistic jets set a limit to the usability of Gaia positions for radio astronomy, which means that radio frames will still be needed for highest accuracy applications such as EOP determination.

Frouard *et al.* (2018) and Liu *et al.* (2018) showed that the Gaia DR1 catalog agrees better (in terms of large-scale systematics) with recent ICRF solutions (U16A and gsf2016a respectively) than with ICRF2.

Gaia Collaboration *et al.* (2018b) repeated their comparisons when Gaia DR2 was released. With the new Gaia data and radio positions from a preliminary ICRF3 prototype solution the distribution of the normalized separation was found to deviate from a Rayleigh distribution. However, they report on a satisfactory agreement of these positions on the 20 to 30 μas level.

Plavin *et al.* (2018) used the Radio Fundamental Catalogue[1] which is based on VLBI data and cross-matched it with sources from Gaia DR2. About 9000 matches are found from which they calculate the jet direction of 4000 objects using images from the astrogeo database[2]. They can show that about 3/4 of the significant Gaia VLBI offsets are occurring either upstream or downstream the jet. Gaia includes information on redshift and color of the sources, which they use to distinguish between the effect of the host galaxy, the jet and the accretion disk. They find that strong optical jets are needed to explain the offset downstream while offsets upstream are at least partly due to impacts from the accretion disk on the Gaia coordinates and impacts from radio jets on the VLBI position.

Petrov *et al.* (2019) showed that positional errors of VLBI and Gaia should be rescaled in order to best fit the normalized separation distribution to the Rayleigh distribution. They demonstrated that the main reason for statistically significant offsets between VLBI and Gaia is the presence of optical structure, by showing that the majority of outliers have offsets along the jet direction. Further, they show that by rescaling the formal uncertainties of the VLBI and Gaia frame the distribution of the normalized differences gets closer to a Rayleigh distribution. They provide a scaling factor of 1.3 and 1.06 for the VLBI and Gaia uncertainties respectively. Additionally, they showed that the percentage of outliers depends on the factor χ^2/ndf, where ndf are the degrees of freedom. Both parameters are published within Gaia DR2. The number of outliers grows approximately with $\sqrt{\chi^2/ndf}$, therefore, this value can be used to scale the uncertainties of the individual sources.

---

[1] http://astrogeo.org/vlbi/solutions/rfc_2018b/
[2] http://astrogeo.org/vlbi_images/

Chapter 2

Data

2.1 VLBI data set

The data used to estimate the ICRF is made available by the International VLBI Service for Astrometry and Geodesy, see Nothnagel *et al.* (2015) for more detail. It consists of a set of group delay measurements in bandwidth synthesis mode corrected for various effects. Usually geodetic VLBI experiments utilize a globally distributed station network and last for 24h. These experiments are called sessions. The basic measurement is conducted in two frequency bands, X band with 8.4 GHz and S band with 2.3 GHz. From measurements in two bands, the effect of the ionosphere can be estimated to a first degree and consequently corrected. In geodetic VLBI, the instrumental delays are corrected using an injection of phase calibration tones at the receiver end. Meteorological data is logged at the station for a priori modeling of parts of the troposphere effect. Some stations have a cable calibration unit, which measures stretching and twisting of cables between receiver and recorder. For more detail see Ma & Feissel (1997) where the usage of VLBI data for CRF determination is described.

The geodetic VLBI data set incorporates more than twelve million VLBI group delay observations from more than hundred stations to more than 4000 sources. It starts in the year 1979 and observations are still ongoing. New telescopes are being developed and the rate of data acquisition is increasing, see black line in Figure 2.1.

2.2 Known problems

Figure 2.2 depicts the distribution of the VLBI stations included in the data set, in black are the stations which have a long observing history, stations depicted as grey are only observing occasionally and red denotes new (after 2009) stations. The quality of the VLBI product is strongly dependent on the volume of the observing network, see Malkin (2009). Therefore, a good station distribution is of high priority. Looking at Figure 2.2 it is obvious that the data set is dominated by stations on the Northern Hemisphere. Stations on the Southern Hemisphere are scarce and far apart, which makes them uniquely important for the
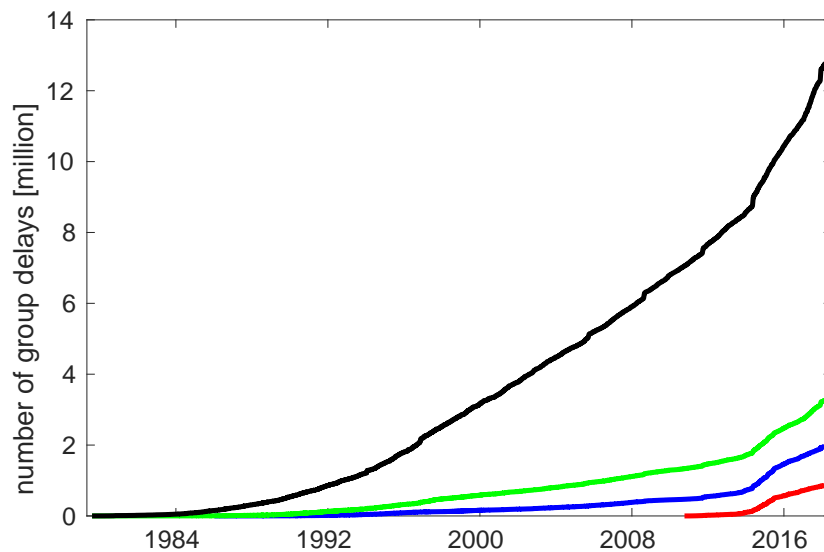
Figure 2.1: The black line depicts the increase of the number of geodetic VLBI group delay measurements from 1979 to 2018. The green line illustrates the number of group delays derived from southern sources (negative declination). The blue line depicts the number of group delays measured with southern stations (located on the Southern Hemisphere). The red line illustrates the number of group delays measured from the AUSTRAL core network (Hobart12, Kath12m and Yarra12m).
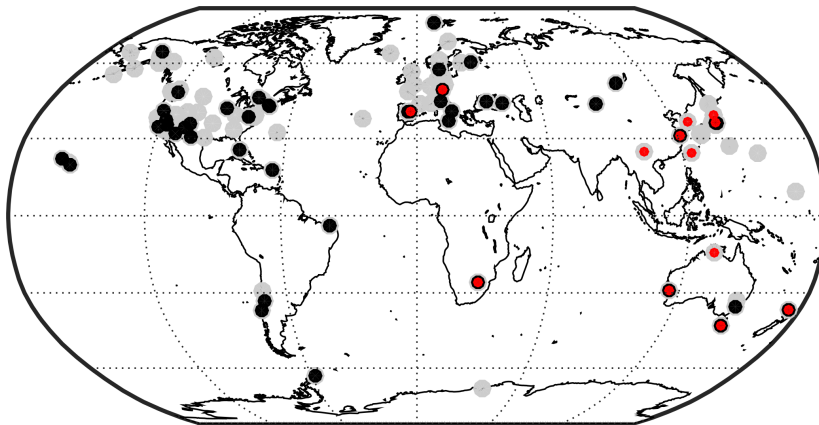
Figure 2.2: Station distribution of global geodetic VLBI network. Regular observing sites are depicted in black, grey sites are only occasionally observing and in red are sites, which were built recently (after 2009).

VLBI products, see Mayer *et al.* (2014). However, ambitious programs such as the AuScope network, see Plank *et al.* (2017) and Lovell *et al.* (2013), have helped to increase the VLBI antenna density in the south.

The uneven station distribution results in an uneven distribution of sources on the celestial sphere. This is illustrated in Figure 2.3 where the distribution of sources present in the used VLBI data set is depicted. Looking at Figure 2.3 it is evident that the distribution of sources above -40 degrees declination is rather dense, however, below this threshold sources are less and further apart. The main reason for this is connected to the VLBA network which can only observe sources to about -40 degrees declination, more detail on this can be found in Section
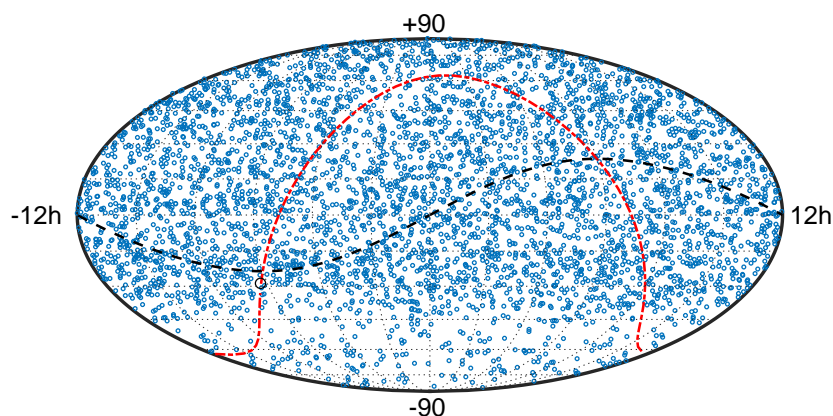
Figure 2.3: Distribution of sources in the VLBI data set on the celestial sphere. The galactic plane is depicted in red with the center of the galaxy denoted as a black circle. The ecliptic is depicted as a black dashed line.

1.5. Comparing the far north to the far south reveals that not only the number of sources is significantly smaller but also their accuracy is almost twice as bad with a median formal error in declination of sources in the far north (above +45 degrees) being 115 μas and in the far south (below -45 degrees) being 216 μas. Note that these errors are not yet scaled. This is a well-known problem, which the International VLBI Service for Geodesy and Astrometry (IVS), see Nothnagel *et al.* (2017) for more information, tried to solve with dedicated CRF sessions in the far south. However, the scarce station distribution in these latitudes limited the success of this program. Recently, the new stations in Australia are utilized to observe new sources in the far south, see McCallum *et al.* (2017) and the SOAP program[1]. The main limitation of these stations is the decreased sensitivity, which is due to the small dish sizes. However, new scheduling strategies, described in McCallum *et al.* (2017), were developed to mitigate this problem.

The magnitude of the problem of uneven observation distribution in the north-south direction can be easily displayed when the observations are divided into northern and southern observations. In Figure 2.1, where the total number of measured group delays is depicted in black, the green line represents the number of observations to southern sources (negative declination). It is clearly visible that almost three times as much data was collected from northern sources. Figure 2.1 also depicts the observations made by southern stations where the difference is even more pronounced with five times as many observations made by northern stations. However, as mentioned before, the Australian network became operational in 2011 and started observing regularly with a particularly dense observing schedule around 2014 to 2015. The Australian sites collected almost a million (860,000) observation in a very short time. Their observations are represented by the red line in Figure 2.1. The sudden increase in observations from southern stations and to southern sources are solemnly their achievement

---

[1] http://astrogeo.org/soap/soap_proposal.pdf

along with collaborating stations such as Wark12m and Hart15m.

Another problem connected to the station distribution is the fact that networks of all sizes are included in the data set. This is illustrated in Figure 2.4 where the sessions are divided into sections depending on the number of stations in the network. Most sessions include four
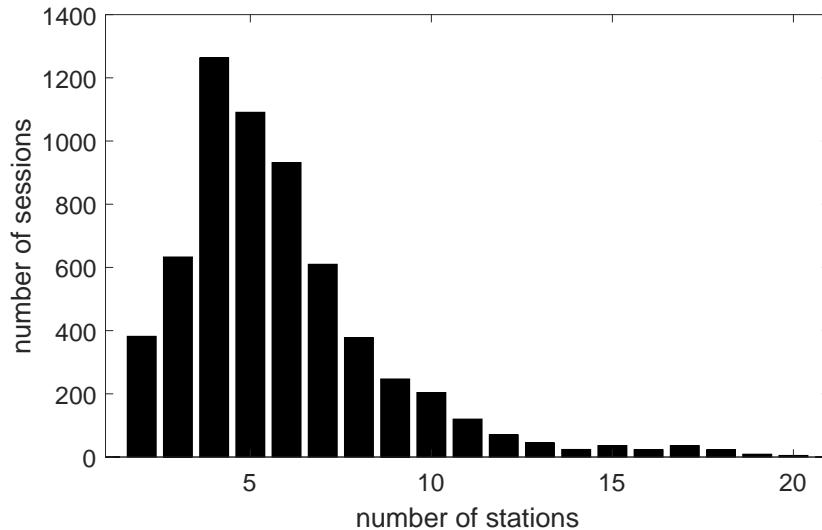
Figure 2.4: Distribution of stations per session in the VLBI data set. The distribution peaks at 4 stations.

to five stations, which is rather small for a global VLBI network. Especially, sessions in the early history of VLBI suffer from weak observation geometry.

A further problem this data set experiences is the uneven distribution of observations. This is illustrated by the distribution of measured group delays over sources, depicted in Figure 2.5. Most of the sources have about 200 to 300 observations. Then the number of observations drops with almost no sources at the 1000 observations mark. However, about 500 sources have more than 1000 observations. Some sources are observed in almost every session and, therefore, accumulated a huge about of data over the years. The most observed source is 0059+581 with more than 400,000 observations. By comparison, adding the total amount of data of the 2700 least observed sources accounts for approximately the same number. In other words, the most observed source has as much data as 62 % of all sources combined. A weak observing history is particularly problematic when sources are only observed in single sessions since there is no oversight and correlations between parameters due to weak observing geometries can propagate into the source coordinates, see Mayer *et al.* (2015).
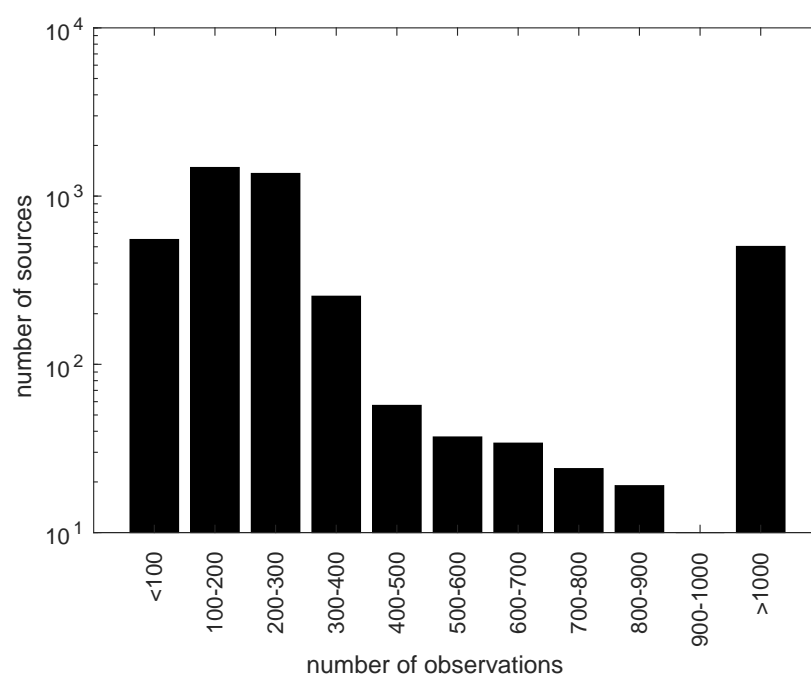
Figure 2.5: Distribution of the number of observations per source in the VLBI data set. Most sources have between 100 and 300 observations. About 500 sources have more than 1000 observations.

Chapter 3

Analysis

3.1   Geodetic VLBI analysis

In geodetic VLBI, the data is segmented in sessions, which are usually 24h long and consist of a network of at least two stations. Parameters such as source coordinates, troposphere parameters etc. can be estimated from these single sessions using a statistical estimation technique such as the least squares method, more detail can be found in Section 4.1. However, in order to estimate a reference frame from all the geodetic VLBI data available one has to combine these single sessions into one global adjustment.

3.1.1   Single sessions analysis

Time sensitive (e.g. changing weather) as well as time insensitive (e.g. station coordinates) parameters can be estimated in a single session analysis. This is done by the means of a statistical parameter estimation technique such as the least squares method. In order to do the linearization needed for this method (the LSM can only deal with linear observation equations) accurate a priori information is needed. This includes station and source positions, which are taken from reference frames as well as EOP time series. Further, certain geophysical effects such as solid Earth tides as well as Earth rotation effects such as high frequency components have to be modeled. A complete description of the modeling approach for VLBI can be found in the International Earth Rotation and Reference System Service (IERS) Conventions, see Petit & Luzum (2010).

When the modeling is completed one has to decide, which parameters to estimate. Further, it has to be decided how these parameters should be estimated. In theory, the best approach would be to estimate all parameters at every scan. However, this means that hundreds of parameters have to be calculated from a couple of observations, which is obviously not possible. Therefore, some kind of interpolation has to be introduced. In the analysis software used in this thesis this is realized using the concept of PWLO, see Section 3.2 for more information. The estimation interval for the parameter is set by the user. Then the parameter

is estimated at each specified epoch. Having decided on the method, the parameters, which will be estimated, have to be chosen. Usually our target parameters are station and source coordinates as well as EOP offsets.

In order to estimate these parameters certain network constraints have to be applied. The reason for this is that geodetic VLBI measures distances. Therefore, in theory, the whole network could be translated or rotated without changing these distances. This inherent property makes it necessary to constrain these translations and rotations, which is usually done by so-called no-net-rotation (NNR) and no-net-translation (NNT) constraints. These network constraints force the overall (sum of all stations that participate in the constraint) rotation and translation to zero. The same holds true for source coordinates, however, since the observed sources are infinitely far away (to a certain extent this is true) only the coordinate rotation has to be considered.

Additionally, auxiliary parameters have to be estimated. These have to be estimated in order to get reasonable target parameters but are not of high interest for the geodesist. In geodetic VLBI, these auxiliary parameters are usually the troposphere and clock. They cannot be predicted (modeled) with reasonable accuracy and, therefore, have to be estimated. The standard procedure for estimating the troposphere is the concept of Zenith Wet Delays (ZWD). With this approach, the slant delay is mapped to zenith direction using a mapping function. The easiest approach for mapping the slant delays to the zenith direction would be a mapping function of $\frac{1}{\sin\epsilon}$. However, this assumes a flat Earth and does not consider different weather conditions. A better approach is the VMF1 which uses numerical weather models to extract a mapping function, see Böhm *et al.* (2006) for more detail. With this approach, it is possible to map scans in different elevations to the zenith direction. However, the azimuthal component of the troposphere is not yet accounted for. In order to deal with the azimuthal dependency, north and south gradients are estimated. A priori knowledge of these tropospheric gradients can be applied using a model. Gradients published in such a model are usually calculated from a numerical weather model. The atomic clock at a VLBI station is highly stable, however, they do drift and experience nonlinear behavior. Hence, the drifting and nonlinear motion of the atomic clock has to be accounted for. In the analysis software used in this thesis, this is realized by estimating a drift and quadratic term over the whole session as well as PWLO.

Having set everything up correctly the LSM can be performed and the desired parameters derived, see Section 4.1. However, if the goal is to create a reference frame a number of sessions have to be analyzed together. This is done using a global solution, see next section. The normal equation system has to be saved in order to use it as input for the global solution. It has to be noted here that these normal equation systems should be saved constraint-free.

3.1.2   Global parameter estimation analysis

In the global parameter estimation, the desired global parameters are estimated. The normal equation systems from the single session analysis are combined to one global normal equation system from which the target parameters are estimated. The standard geodetic target parameters are the CRF and TRF but also other parameters can be estimated such as the relativistic γ parameter or antenna axis offsets and many more. Since EOP are very variable with time, they are not a prime example of a global parameter. Nevertheless, they can also be calculated in a global parameter adjustment.

In order to conduct a global solution, first, the undesirable parameters have to be removed from the normal equation system of the single session analysis, see Section 4.1.2 for more detail on parameter elimination. The eliminated parameters are the so-called arc parameters. Stations and sources can be eliminated as well. Usually, this is done when not enough observations exist to estimate a reliable position or when the assumption of linear station movement or source stability does not hold.

In the second step the normal equation systems has to be expanded to include all desired parameters. Practically speaking this means inserting zero lines and columns, where parameters are missing, into the normal equation systems. At the end of this procedure, one should have a number of normal equation systems, all the same size all, containing the same parameters. To get a global normal equation system one can simply stack (add together) these matrices, see Section 4.1.3 for more detail on stacking of normal equation systems.

After these steps, the desired parameters can be calculated. In order to do that, constraints similar to the single session analysis have to be added, e.g. NNR and NNT constraints for the TRF and NNR constraints for the CRF. Additionally, other constraints can be added, such as velocity constraints to ensure that antennas on the same site experience the same continental drift. After adding the constraints to the normal equation system, the desired parameters can be calculated.

The results of the estimation procedure are estimates and their formal errors. In a standard geodetic VLBI solution the calculated formal errors are usually too optimistic. This is due to the fact that during the least squares adjustment it is assumed that all errors follow a Gaussian distribution. With this assumption the uncertainties of the parameters decrease with $\sqrt{N}$. However, in reality not all errors follow a Gaussian distribution, which means that errors reported by the LSM are too optimistic. The solution to this problem is the rescaling of formal errors after the LSM. In order to find the scaling factor, the agreed approach is to create two independent solutions by dividing the data set into equal parts. The differences in these solutions can be used to calculate the scaling factor. In short, this is done by scaling the differences of estimates with their formal errors. The standard deviation of the scaled difference is the so-called scaling factor. Usual scaling factors used in geodetic VLBI are around 1.5. Additionally to the scaling factor, a noise floor is introduced to account for residual scaling errors. The noise floor can be calculated from the two solutions mentioned

before. The WRMS of the differences is calculated and scaled by $1/sqrt(2)$ (this assumes that no correlations are present and that both solutions have the same level of noise) to get an estimate of the noise floor. The noise floor could be calculated from subsets such as declination bins and then used for these declinations. Usual noise floors used in geodetic VLBI are around 30 to 40 µas. The overall inflation equation reads:

$$\sigma^2_{\alpha \cos \delta} = (scaling factor \cdot \sigma_{\alpha \cos \delta,0})^2 + (noise floor)^2 \qquad (3.1)$$

for right ascension and

$$\sigma^2_\delta = (scaling factor \cdot \sigma_{\delta,0})^2 + (noise floor)^2 \qquad (3.2)$$

for declination.

3.2 The analysis software VieVS

The software used for all computations in this thesis is called Vienna VLBI and Satellite Software, in short: VieVS. It is developed by the research group Höhere Geodäsie of the Department of Geodesy and Geoinformation at the Technische Universität Wien in Austria. VieVS is a state of the art software used for VLBI, Satellite Laser Ranging (SLR) and Global Navigation Satellite System (GNSS) analysis. Further, it incorporates tools for troposphere delay modeling, ring laser analysis and technique combination tools. Figure 3.1 depicts the interactions of the different parts of VieVS. In this thesis only the VLBI part is used, therefore, all following descriptions refer to this part.
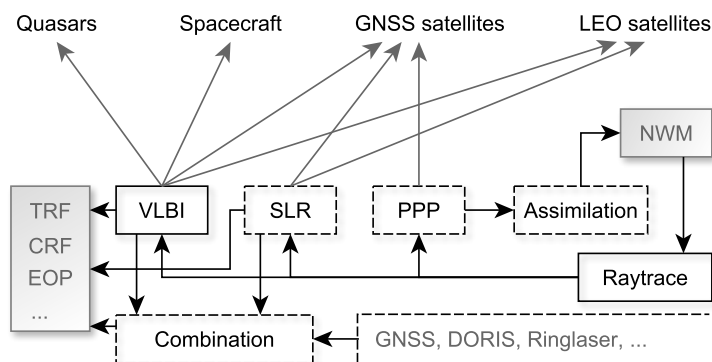
Figure 3.1: General structure and interactions of different parts of VieVS. Boxes with solid lines are models, which are already implemented while boxes with dashed lines represent models currently under development. Grey boxes refer to products while grey arrows symbolize observations.

What follows is a short introduction to the software. A more detailed description can be found in Böhm *et al.* (2018). VieVS has a modular structure, which means that it is a

consortium of separate parts, which can be used as standalone tools but also in combination with each other. This has the advantage that modules can be run separately or in conjunction with one another. For example, a rough first schedule can be produced using only the scheduling package and on a later stage a finer scheduling parameter selection can be completed by adding simulation and analysis models to the workflow. In total the VLBI part of VieVS is comprised of seven modules, they are:

- VIE_SETUP - this module incorporates the graphical user interface. All other modules are controlled by this module.

- VIE_SCHED - schedules can be produced using this model, more detail on this package can be found in Sun *et al.* (2014). However, in recent years a new scheduling tool was developed by Schartner & Böhm (2018) in C++. The name of this more advanced tool is VIE_SCHED++.

- VIE_SIM - with this module it is possible to simulate artificial observations, for more detail see Pany *et al.* (2011).

- VIE_INIT - data is loaded into the software using this module.

- VIE_MOD - the theoretical delays and the partial derivatives are calculated using this module.

- VIE_LSM - this module takes care of the least squares adjustment, see Section 4.1

- VIE_GLOB - in this module the global parameter estimation is realized, see Krásná (2013).

In VieVS, the parameters are estimated using the method of PWLO. This means that one linear segment is estimated in a given interval. A scan that takes place in between two offsets is related to these offsets by the means of a linear interpolation. This method allows for a continuous time series of linear segments and one has the option to set relative and absolute constraints. Relative constraints are pseudo observations, which tell the LSM that the next offset can only be a certain value away from the previous one. This is important for bridging observation gaps as well as applying a priori knowledge of the variability of the parameter. Absolute constraints are pseudo observations as well; they tell the LSM that no offset can be further than a certain value from the a priori value. This constraint can also help to bridge data gaps; also, it introduces a priori knowledge of the maximal range of a parameter.

3.3   The Vienna ICRF solution

The Vienna ICRF solution was created using the geodetic VLBI analysis software VieVS, see Section 3.2 for more detail on the software.

Geophysical modeling	IERS Convention, see Petit & Luzum (2010)
Antenna thermal expansion	Model by Nothnagel (2009)
Atmospheric pressure loading	Model by Wijaya *et al.* (2013)
A priori station coordinates	ITRF2014, see Altamimi *et al.* (2016)
A priori source positions	ICRF2, see Ma *et al.* (2009) and Fey *et al.* (2015)
EOP	EOP 14 C04 time series, see Bizouard *et al.* (2018)
Nutation and precession	IAU 2000A and IAU 2006 model, recommended in the electronic update of the IERS Conventions by Petit & Luzum (2010)
A priori tropospheric gradients	DAO model by MacMillan (1995) and MacMillan & Ma (1997)
Mapping function	VMF1, see Böhm *et al.* (2006)

Table 3.1: A priori values and models used in the Vienna single session analysis.

Station network datum constraints	All stations that are listed in the ITRF2014 are used for the datum constraints
Source datum constraints	All defining sources from the ICRF2 are used
ZWD	Estimated as PWLO every 30 min with relative (from one estimate to the next) constraints of 1.5 cm
North and south gradients	Estimated as PWLO every 6 h with relative constraints of 0.5 mm and absolute (w.r.t. the a priori value) constraints of 0.5 mm
Clock	Estimating a drift and quadratic term over the whole session as well as PWLO every 60 min with relative constraints of 1.3 cm
EOP	PWLO every 48 h with very tight constraints of 0.1 µas were used to estimate the EOP

Table 3.2: Solution setup of the Vienna single session analysis.

3.3.1   The Vienna single session analysis

In the standard single session analysis with VieVS the a priori values and models described in Table 3.1 are used. Special care has been taken to use models that are accurate and up to date. Further, the consistency of a priori TRF (ITRF2014) and EOP (EOP 14 C04) was taken into consideration. At the time this solution was created, the ICRF2 was the official celestial reference frame. Hence, it was used in the analysis. In situ tropospheric parameters, which were recorded at the stations, were used for the standard modeling of the hydrostatic zenith delay.

The solution setup is listed in Table 3.2. It has to be noted that the normal equation system, which is the input of the global solution and, therefore, the result of the single session analysis, must be constraint-fee, see Section 4.1.3. Nevertheless, the constraints defined for the troposphere, clock and EOP are used in VieVS to reduce (see Section 4.1.2 for more information on the reduction of parameters) these parameters from the normal equation system.

Hence, these parameters still affect the solution. However, the datum constraints for the TRF and CRF are not used in further analysis and are, therefore, not important.

The estimation setup of the EOP might appear strange for readers unfamiliar with VieVS. It is equivalent to estimating one offset per session for the EOP. The interval of 48 h was chosen to assure that only two offsets, one at midnight before and one at midnight after the session, are estimated. This was done to facilitate the transformation from this approach to an offset and rate estimation approach. The tight relative constraints of 0.1 μas were chosen to align the two offsets, which is more or less equivalent to a single offset.

3.3.2   The Vienna global parameter estimation

In the global parameter estimation, the time insensitive parameters are estimated from a series of 6199 24 h sessions. For the Vienna solution, the global parameters are station coordinates, station velocities and source coordinates. In total the positions and velocities of 97 stations and the positions of 4482 sources are estimated. Stations, which do not have enough data to calculate a reliable position and velocity are reduced (estimated per session); in this solution, 69 stations are reduced. The same is done for sources, which are known to experience significant positional movement; in this solution, the so-called 39 special handling sources (used in the ICRF2) are reduced. For the TRF constraints, 21 stable stations are used and for the CRF constraints, the 295 ICRF2 defining sources are used.

3.3.3   Computational environment

The IT infrastructure provided by the GEO department at the Technische Universität Wien includes so called project PCs. These are powerful computers shared by the department and can be used for computational intensive tasks. VieVS makes use of the parallel computing toolbox, which is provided by Matlab, to estimate single sessions in parallel. Using a sufficient number of cores significantly reduces the processing time, which enables us to process the whole data set in about 2 h. Unfortunately, the global solution module of VieVS does not yet support parallel computing which is why it needs up to 6 h to estimate a CRF and TRF. In total using VieVS within the GEO infrastructure enables us to estimate a CRF from scratch within 8 h.

3.3.4   Galactic aberration estimation

The Solar System Barycenter (SSB) rotates about the Galactic Center in a quasi-circular orbit. This induces an acceleration of the SSB, which causes pseudo proper motions of quasars. The resulting proper motion field can then be used to estimate the Galactic Aberration (GA). However, the variability of source structure causes similar random (in terms of direction; the jet can be pointed in any direction) proper motions in quasars which makes separation problematic.

Two different approaches to estimate the GA from VLBI data can be found in the literature. In the first method the quasar proper motion field is calculated and then the GA is estimated from that field using VSH (see Section 4.4.2), see Gwinn *et al.* (1997), Titov & Lambert (2013) and Titov & Lambert (2016). The second approach includes the estimation of GA directly in the global solution. Here it can be further distinguished. Titov *et al.* (2011) and Xu *et al.* (2012) include GA directly into the VLBI delay equation with small differences. Titov *et al.* (2011) ignore the component normal to the Galactic plane. A sort of hybrid solution where the VSH components are directly calculated in a global solution is introduced by MacMillan (2005). Recently, Titov & Krásná (2018) showed that the GA can also be calculated using the Earth scale factor.

In VieVS the approach described by Titov *et al.* (2011) and Titov & Krásná (2018) is implemented. Krásná & Titov (2017) showed that GA estimates from this implementation are comparable with other published values. A short overview of the equation needed to estimate GA will be provided here.

In Petit & Luzum (2010) the conventional vacuum group delay model is given as

$$t_{v_2} - t_{v_1} = \frac{\Delta T_{grav} - \frac{\boldsymbol{Kb}}{c}\left(1 - \frac{(1+\gamma)U}{c^2} - \frac{|\boldsymbol{V_\oplus}|^2}{2c^2} - \frac{\boldsymbol{V_\oplus \omega_2}}{c^2}\right) - \frac{\boldsymbol{V_\oplus b}}{c^2}\left(1 + \frac{\boldsymbol{KV_\oplus}}{2c}\right)}{1 + \frac{\boldsymbol{K}(\boldsymbol{V_\oplus}+\boldsymbol{\omega_2})}{c}}. \tag{3.3}$$

The notation is provided in Table 3.3. Proper motions can be added to the source vector and after some simplifications, the details of which can be found in Titov *et al.* (2011), Equation 3.4, which contains the galactic acceleration $\boldsymbol{a}$ and the time since the reference epoch Δt, is derived. This equation contains only terms up to order $O\left(\frac{a}{c^2}\right)$.

$$t_{v_2} - t_{v_1} = \frac{\Delta T_{grav} - \frac{\boldsymbol{Kb}}{c}\left(1 - \frac{(1+\gamma)U}{c^2} - \frac{|\boldsymbol{V_\oplus}|^2}{2c^2} - \frac{\boldsymbol{V_\oplus \omega_2}}{c^2}\right) - \frac{(\boldsymbol{V_\oplus}+\boldsymbol{a}\Delta t)\boldsymbol{b}}{c^2}\left(1 + \frac{\boldsymbol{KV_\oplus}}{2c}\right)}{1 + \frac{\boldsymbol{K}(\boldsymbol{V_\oplus}+\boldsymbol{a}\Delta t+\boldsymbol{\omega_2})}{c}} \tag{3.4}$$

The partial derivative, which is needed for the LSM, can then directly be calculated, it reads:

$$\frac{\partial \tau}{\partial \boldsymbol{a}} = \frac{\Delta t}{c^2}\left((\boldsymbol{Kb})\,\boldsymbol{K} - \boldsymbol{b}\right) - \frac{\Delta t}{c^3}\left(\boldsymbol{b}\left(\boldsymbol{K}\left(\boldsymbol{V_\oplus} + \boldsymbol{\omega_2}\right)\right) + \frac{\boldsymbol{b}\left(\boldsymbol{V_\oplus K}\right)}{2} - \left(\boldsymbol{bV_\oplus}\right)\boldsymbol{K}\right). \tag{3.5}$$

Equation 3.5 contains only terms up to order $O\left(\frac{1}{c^3}\right)$ and neglects the gravitational delay. Using Equation 3.4 and 3.5 GA can be directly estimated in a global solution.

If an estimate for GA was obtained it can be used to correct GA in the solution. In VieVS, this is done by correcting the vacuum delay. Equation 3.4 is used instead of Equation 3.3 to calculate the vacuum delay.

t_{v_i}	time of arrival of radio signal at i^{th} VLBI antenna. This is the vacuum time including gravitational delay and not including any effects of due to the atmosphere
ΔT_{grav}	the differential gravitational time delay (Shapiro effect)
$\boldsymbol{K}$	unit vector from barycenter to source
$\boldsymbol{b}$	baseline vector
c	speed of light
γ	parameterized post-Newtonian parameter; equals 1 for general relativity
U	gravitational potential of Sun at geocenter
$\boldsymbol{V}_\oplus$	barycentric velocity of geocenter
ω_i	geocentric velocity of ith antenna

Table 3.3: Notation of terms and short description used in group delay model by Petit & Luzum (2010).

3.4 Naming convention

In order to keep track of the multiple solutions, which will be investigated, it was decided to include a naming convention. It should be short but still carry meaning in a way that the reader can look at the name and immediately see the basic information, such as time span of observations, models used etc. The following convention was used:

- The first three letters will resemble the analysis center, in our case it will be "Vie".

- Then two numbers, which symbolize the time span used. The time span will always start in 1979, the beginning of geodetic VLBI data and it ends at the year abbreviated with two numbers, e.g. the ICRF2 includes data until March 2009, and, therefore, its suffix would be 09.

- Separated by a dash, a string, which denotes different a priori models, will be provided. This will always be with respect to the reference solution described in Section 3.3, e.g. if the solution uses the GRAD a priori gradient model but in the reference solution the DAO model is used, the suffix "-GRAD" would be added.

- The last extension to this convention is the analysis choice separated with a dash. E.g., if in the solution ZWD are estimated every 1 h but in the reference solution it is estimated every 30 min, then the suffix "-ZWD1h" would be added.

- If more than one a priori model is changed or more than one analysis choice differs the suffix is added to the naming convention separated by another dash.

For example, the Vienna group created an ICRF3 solution where a priori ray-traced delays were used and gradients were fixed. Following the naming convention, the solution would be given the name "Vie18-RayTrace-fixGrad".

The author is aware that not every reader will immediately understand these arbitrary abbreviations, which is why an additional small explanation for every solution used in this thesis is provided before:

- **Vie18**: reference solution, see Section 3.3.

- **Vie18-AOaltitudeCorr**: the correction for antenna axis offsets altitude correction is applied, see Section 5.2.2.

- **Vie18-AOest**: the antenna axis offsets are estimated for the southern stations, see Section 5.2.1.

- **Vie18-Clock30min**: the estimation intervals for the station clocks are changed to 30 min, see Section 5.2.5.

- **Vie18-ClockConst13cm**: the relative constraints between station clock estimates are changed to 13 cm, see Section 5.2.5.

- **Vie18-ElWeight6ps**: noise is added (6 ps) to observations with low elevations, see Section 5.2.8.

- **Vie18-ElWeight12ps**: noise is added (12 ps) to observations with low elevations, see Section 5.2.8.

- **Vie18-ErrorInflated**: the formal errors are inflated, see Section 5.2.13.

- **Vie18-estGA**: the galactic aberration vector is estimated, see Section 5.2.11.

- **Vie18-estGA-elWeight6ps**: the galactic aberration vector is estimated and noise is added (6 ps) to observations with low elevations, see Section 5.2.11.

- **Vie18-estGA-elWeight12ps**: the galactic aberration vector is estimated and noise is added (12 ps) to observations with low elevations, see Section 5.2.11.

- **Vie18-estGA-Grad1h**: the galactic aberration vector is estimated and the estimation interval for the gradients is changed to 1 h, see Section 5.2.11.

- **Vie18-estGA-Grad3h**: the galactic aberration vector is estimated and the estimation interval for the gradients is changed to 3 h, see Section 5.2.11.

- **Vie18-estGA-noAbsGradConst**: the galactic aberration vector is estimated and the absolute constraints on gradients are loosened to 1 m, see Section 5.2.11.

- **Vie18-estGA-RayTrace**: the galactic aberration vector is estimated and ray-traced delays are used a priori, see Section 5.2.11.

- **Vie18-GA2015**: galactic aberration is corrected to 2015 with 5.8 µas per year, see Section 5.2.12.

- **Vie18-GA2015-noSpecialHandling-ICRF3defining-ICRF3apriori-ErrorInflated**: galactic aberration is corrected to 2015 with 5.8 µas per year, all sources are estimated as global parameters, the ICRF3 defining sources in S/X band are used as defining sources, the ICRF3 S/X band solution is used as a priori catalog and the formal errors are inflated, see Section 5.6.

- **Vie18-GA2015-RayTrace-elWeight6ps**: galactic aberration is corrected to 2015 with 5.8 µas per year, ray-traced delays are used a priori, the absolute constraints on gradients are loosened to 1 m and noise is added (6 ps) to observations with low elevations, see Section 5.3.

- **Vie18-GA2015-RayTrace-elWeight12ps**: galactic aberration is corrected to 2015 with 5.8 µas per year, ray-traced delays are used a priori, the absolute constraints on gradients are loosened to 1 m and noise is added (12 ps) to observations with low elevations, see Section 5.3.

- **Vie18-GA2015-RayTrace-noAbsGradConst**: galactic aberration is corrected to 2015 with 5.8 µas per year, ray-traced delays are used a priori and the absolute constraints on gradients are loosened to 1 m, see Section 5.3.

- **Vie18-GA2015-RayTrace-noAbsGradConst-ErrorInflated**: galactic aberration is corrected to 2015 with 5.8 µas per year, ray-traced delays are used a priori, the absolute constraints on gradients are loosened to 1 m and the formal errors are inflated, see Section 5.3.

- **Vie18-GA2015-RayTrace-PCalHb**: galactic aberration is corrected to 2015 with 5.8 µas per year, ray-traced delays are used a priori, the absolute constraints on gradients are loosened to 1 m and a systematic effect due to phase calibration at the station Hobart12 is corrected, see Section 5.3.

- **Vie18-GRAD**: the a priori gradients from the GRAD model are used, see Section 5.2.3.1.

- **Vie18-Grad1h**: the estimation interval for the gradients is changed to 1 h, see Section 5.2.4.1.

- **Vie18-Grad3h**: the estimation interval for the gradients is changed to 3 h, see Section 5.2.4.1.

- **Vie18-Grad3h-noAbsGradConst**: the estimation interval for the gradients is changed to 3 h and the absolute constraints on gradients are loosened to 1 m, see Section 5.2.4.1.

- **Vie18-ICRF3defining-ICRF3apriori**: the ICRF3 defining sources in S/X band are used as defining sources and the ICRF3 S/X band solution is used as a priori catalog, see Section 5.2.7.2.

- **Vie18-NNRHalfFirst**: only half of the defining sources are used for the NNR constraints, see Section 5.2.7.2.

- **Vie18-NNRHalfSecond**: only defining sources that are not used in Vie18-NNRHalfFirst are used for the NNR constraints, see Section 5.2.7.2.

- **Vie18-NNR100muas**: the weight of the NNR constraints is changed to 100 µas, see Section 5.2.7.1.

- **Vie18-NNR1000muas**: the weight of the NNR constraints is changed to 1000 µas, see Section 5.2.7.1.

- **Vie18-NNR20muas**: the weight of the NNR constraints is changed to 20 µas, see Section 5.2.7.1.

- **Vie18-noAbsGradConst**: the absolute constraints on gradients are loosened to 1 m, see Section 5.2.4.2.

- **Vie18-noAPrioriGrad**: the a priori gradients are removed, see Section 5.2.3.1.

- **Vie18-noAPrioriGrad-noAbsGradConst**: the a priori gradients are removed and the absolute constraints on gradients are loosened to 1 m, see Section 5.2.3.1.

- **Vie18-noSpecialHandling**: all sources are estimated as global parameters, see Section 5.2.9.

- **Vie18-PCalHb**: a systematic effect due to phase calibration at the station Hobart12 is corrected, see Section 5.2.6.

- **Vie18-RayTrace**: ray-traced delays are used a priori, see Section 5.2.3.2.

- **Vie18-RayTrace-noAbsGradConst**: ray-traced delays are used a priori and the absolute constraints on gradients are loosened to 1 m, see Section 5.2.3.2.

- **Vie18-SI>4.0**: only sources with SI smaller than 4.0 are used to define the frame, see Section 5.2.7.2.

- **Vie18-SI>3.5**: only sources with SI smaller than 3.5 are used to define the frame, see Section 5.2.7.2.

- **Vie18-SI>3.25**: only sources with SI smaller than 3.25 are used to define the frame, see Section 5.2.7.2.

- **Vie18-SI>3.0**: only sources with SI smaller than 3.0 are used to define the frame, see Section 5.2.7.2.

- **Vie18-StatSesHarm**: station seasonal harmonic functions in north, east and up direction are estimated for the southern stations, see Section 5.2.10.

- **Vie18-ZWD20min**: the estimation interval for the ZWD is changed to 20 min, see Section 5.2.4.1.

- **Vie18-10SpecialHandling**: only the ten most variable sources are session-wise reduced, see Section 5.2.9.

Chapter 4

Methodology

4.1 Least Squares Method

This section is based on Niemeier (2008) and Thaller (2008). Further information on this topic can be found there and the publications therein.

The basic principle of the LSM will be discussed and a brief overview of concepts commonly used in geodesy will be provided. Since it is used throughout this thesis it is important that the reader becomes familiar with the basic terminology of this widely used statistical estimation technique.

4.1.1 The Gauß-Markov-Model

Let us assume that we have n independent observations all compiled in the vector $\boldsymbol{L}$ and we want to use all of them to estimate u parameters assembled in vector $\boldsymbol{X}$. Additionally, we define that $\boldsymbol{X}$ is in some kind of functional dependency on $\boldsymbol{L}$. If the true values $\tilde{\boldsymbol{L}}$ and $\tilde{\boldsymbol{X}}$ are known Equation 4.1 can be written.

$$\tilde{\boldsymbol{L}} = f\left(\tilde{\boldsymbol{X}}\right) \tag{4.1}$$

Unfortunately, each measurement has an error, therefore, the true value $\tilde{\boldsymbol{L}}$ can never be known. What is known, however, are the measured values $\boldsymbol{L}$. In order to keep consistency with the functional model, small residuals in addition to the vector $\boldsymbol{L}$ have to be allowed for. The whole equation system then reads:

$$\boldsymbol{L} + \boldsymbol{v} = f\left(\boldsymbol{X}\right). \tag{4.2}$$

The Gauß-Markov-Model is only valid, if the functional dependency is linear. In VLBI and many other application of LSM this is not the case, therefore, the functional dependency has to be linearized. The easiest way to linearize a function is by obtaining its first-order Taylor series expansion. However, in order to perform a Taylor expansion a priori values $\boldsymbol{X_0}$

are needed for the unknowns $\boldsymbol{X}$. Then only small corrections $\boldsymbol{x}$ are estimated. The Taylor expansion until degree 1 reads:

$$\boldsymbol{L} + \boldsymbol{v} = f\left(\boldsymbol{X_0}\right) + \left(\frac{\partial f}{\partial \boldsymbol{X}}\right)_{\boldsymbol{X}=\boldsymbol{X_0}} \cdot \boldsymbol{x}. \tag{4.3}$$

The values of the function with the a priori unknowns $f\left(\boldsymbol{X_0}\right)$ is often called computed. Subtracting it from the observations $\boldsymbol{L}$ results in the so-called observed minus computed vector and is often denoted as $\boldsymbol{l}$. The derivatives $\left(\frac{\partial f}{\partial \boldsymbol{X}}\right)_{\boldsymbol{X}=\boldsymbol{X_0}}$ are combined into the so-called Jacobian matrix $\boldsymbol{A}$. Finally, the functional model can be written as:

$$\boldsymbol{l} + \boldsymbol{v} = \boldsymbol{A}\boldsymbol{x}. \tag{4.4}$$

The residuals can then be written as

$$\boldsymbol{v} = \boldsymbol{A}\boldsymbol{x} - \boldsymbol{l}. \tag{4.5}$$

As the name least squares method suggests we want to minimize the sum of the squares of the residuals $\boldsymbol{v}$. This leads to the basic condition this method relies on:

$$\boldsymbol{v}^T \boldsymbol{v} \rightarrow min. \tag{4.6}$$

First, the sum of the squares of the residuals is calculated using Equation 4.7.

$$\boldsymbol{v}^T \boldsymbol{v} = \left(\boldsymbol{x}^T \boldsymbol{A}^T - \boldsymbol{l}^T\right) \left(\boldsymbol{A}\boldsymbol{x} - \boldsymbol{l}\right) = \boldsymbol{x}^T \boldsymbol{A}^T \boldsymbol{A}\boldsymbol{x} - 2\boldsymbol{x}^T \boldsymbol{A}^T \boldsymbol{l} + \boldsymbol{l}^T \boldsymbol{l} \tag{4.7}$$

In a mathematical sense, the minimum of a function can be found by setting its derivative to zero. Therefore, in a second step the derivative of the squares of the residuals is calculated and set to zero, see Equation 4.8.

$$\partial\left(\boldsymbol{v}^T \boldsymbol{v}\right) = \partial\boldsymbol{x}^T \boldsymbol{A}^T \boldsymbol{A}\boldsymbol{x} + \boldsymbol{x}^T \boldsymbol{A}^T \boldsymbol{A}\partial\boldsymbol{x} - 2\partial\boldsymbol{x}^T \boldsymbol{A}^T \boldsymbol{l} = 2\partial\boldsymbol{x}^T \left(\boldsymbol{A}^T \boldsymbol{A}\boldsymbol{x} - \boldsymbol{A}^T \boldsymbol{l}\right) \tag{4.8}$$

Equation 4.8 becomes zero when the expression in the brackets becomes zero. Therefore, the final equation reads:

$$\left(\boldsymbol{A}^T \boldsymbol{A}\boldsymbol{x} - \boldsymbol{A}^T \boldsymbol{l}\right) = 0. \tag{4.9}$$

With a little bit of rearranging the parameters can be calculated:

$$\boldsymbol{x} = \left(\boldsymbol{A}^T \boldsymbol{A}\right)^{-1} \boldsymbol{A}^T \boldsymbol{l}. \tag{4.10}$$

This equation is only valid for equally good observations. In the real world, this is rarely the case. A stochastic model, which introduces the possibility to weight observations differently, can be utilized. This is done using Equation 4.11.

$$\boldsymbol{\Sigma}_{ll} = \begin{pmatrix} \sigma_1^2 & \cdots & 0 \\ \vdots & \ddots & \vdots \\ 0 & \cdots & \sigma_n^2 \end{pmatrix} = \sigma_0^2 \begin{pmatrix} \frac{\sigma_1^2}{\sigma_0^2} & \cdots & 0 \\ \vdots & \ddots & \vdots \\ 0 & \cdots & \frac{\sigma_n^2}{\sigma_0^2} \end{pmatrix} = \sigma_0^2 \boldsymbol{Q}_{ll}, \tag{4.11}$$

where $\sigma_1^2 \cdots \sigma_n^2$ are the variances of the individual observations. The matrix $\boldsymbol{\Sigma}_{ll}$ is called covariance matrix. Removing σ_0^2 from $\boldsymbol{\Sigma}_{ll}$ results in the cofactor matrix $\boldsymbol{Q}_{ll}$. This approach represents the fact that often times only relative accuracies are known. The variance factor σ_0^2 is then usually estimated during the LSM. Correlations between observations can be introduced into the stochastic model off the main diagonal. From Equation 4.11 the weighting matrix $\boldsymbol{P}$ can be derived:

$$\boldsymbol{P} = \boldsymbol{Q}_{ll}^{-1}. \tag{4.12}$$

When the stochastic model is introduced into the parameter estimation the minimization criteria changes to:

$$\boldsymbol{v}^T \boldsymbol{P} \boldsymbol{v} \to min. \tag{4.13}$$

Further, the final Equation 4.10 changes to:

$$\boldsymbol{x} = \left(\boldsymbol{A}^T \boldsymbol{P} \boldsymbol{A} \right)^{-1} \boldsymbol{A}^T \boldsymbol{P} \boldsymbol{l}. \tag{4.14}$$

Equation 4.14 is often abbreviated with

$$\boldsymbol{x} = \boldsymbol{N}^{-1} \boldsymbol{b}, \tag{4.15}$$

where $\boldsymbol{N} = \boldsymbol{A}^T \boldsymbol{P} \boldsymbol{A}$ and $b = \boldsymbol{A}^T \boldsymbol{P} \boldsymbol{l}$. This is then called the normal equation system with $\boldsymbol{N}$ being called the normal equation matrix. Once the estimates are calculated, the residuals can be calculated using Equation 4.5. Further, the quantity $\boldsymbol{v}^T \boldsymbol{P} \boldsymbol{v}$ can be determined and, by dividing it with the degree of freedom, the variance factor can be estimated:

$$\hat{\sigma}_0^2 = \frac{\boldsymbol{v}^T \boldsymbol{P} \boldsymbol{v}}{n - u}. \tag{4.16}$$

This $\hat{\sigma}_0^2$ is often called χ^2 per degree of freedom and can be used as a quality indicator for the session fit. The cofactor matrix of the estimates can be calculated with Equation 4.17.

$$\boldsymbol{Q}_{xx} = \boldsymbol{N}^{-1} \tag{4.17}$$

The covariance matrix of the estimates can then be calculated using Equation 4.18.

$$\mathbf{\Sigma}_{xx} = \hat{\sigma}_0^2 \mathbf{Q}_{xx} \tag{4.18}$$

On the main diagonal of this matrix, the variances of the estimated parameters can be found. The covariances, which can be translated into correlations, are found off the main diagonal.

4.1.2 Parameter elimination

The normal equation systems is a u times u matrix with a row and column for each parameter. It is still possible to manipulate the normal equation system in clever ways before performing the parameter estimation. In this section the manipulation technique, which is used to remove unwanted parameters from the normal equation system without changing the desired parameters, is introduced. This is called the reduction of parameters. In geodesy, it is mainly used to remove parameters, which are unique to a specific technique (such as clock parameters in VLBI). This is needed when an inter-technique combination is performed or to remove rapidly changing parameters when combining longer time series.

First, the normal equation system has to be rearranged with all the desired parameters separated from the unwanted parameters. The normal equation system then reads:

$$\begin{pmatrix} \mathbf{N}_{11} & \mathbf{N}_{12} \\ \mathbf{N}_{21} & \mathbf{N}_{22} \end{pmatrix} \cdot \begin{pmatrix} \mathbf{x}_1 \\ \mathbf{x}_2 \end{pmatrix} = \begin{pmatrix} \mathbf{b}_1 \\ \mathbf{b}_2 \end{pmatrix}, \tag{4.19}$$

where 1 denotes the desired parameters and 2 denotes the unwanted parameters, which should be eliminated. These two parts are then separated, they read:

$$\mathbf{N}_{11} \cdot \mathbf{x}_1 + \mathbf{N}_{12} \cdot \mathbf{x}_2 = \mathbf{b}_1 \tag{4.20}$$

and

$$\mathbf{N}_{21} \cdot \mathbf{x}_1 + \mathbf{N}_{22} \cdot \mathbf{x}_2 = \mathbf{b}_2. \tag{4.21}$$

Eliminating $\mathbf{x}_2$, results in Equation 4.22.

$$\left(\mathbf{N}_{11} - \mathbf{N}_{12} \mathbf{N}_{22}^{-1} \mathbf{N}_{21} \right) \cdot \mathbf{x}_1 = \mathbf{b}_1 - \mathbf{N}_{12} \mathbf{N}_{22}^{-1} \mathbf{b}_2 \tag{4.22}$$

One can see that a term is subtracted from N_{11} and from b_1. The new matrices are called the reduced normal equation system with

$$\mathbf{N}_{reduced} = \mathbf{N}_{11} - \mathbf{N}_{12} \mathbf{N}_{22}^{-1} \mathbf{N}_{21}, \tag{4.23}$$

$$\boldsymbol{b}_{reduced} = \boldsymbol{b}_1 - \boldsymbol{N}_{12}\boldsymbol{N}_{22}^{-1}\boldsymbol{b}_2 \tag{4.24}$$

and

$$\left(\boldsymbol{l}^T\boldsymbol{P}\boldsymbol{l}\right)_{reduced} = \boldsymbol{l}^T\boldsymbol{P}\boldsymbol{l} - \boldsymbol{b}_2^T\boldsymbol{N}_{22}^{-1}\boldsymbol{b}_2. \tag{4.25}$$

4.1.3 Stacking of normal equation systems

The procedure of combining normal equation systems is called stacking. Normal equation systems, which have the same target parameters can be combined into one normal equation system without loosing information. In geodesy, this is used to combine observations from different techniques in order to estimate common parameters such as station positions. Another application of this combination is the estimation of common parameters in a long time series. In this thesis, the latter one is used. By stacking normal equation systems from the whole history of VLBI into one combined LSM, parameters such as source positions can be calculated with a very high accuracy.

First, the individual normal equation systems have to be transformed to only contain the desired parameters. Other parameters must be reduced or fixed, see Section 4.1.2. If the desired parameters are not part of the normal equation system, it has to be extended by adding zero lines and columns at the right positions. When everything is done correctly, i normal equation systems, all the same size, can be combined by the stacking procedure (here presented without mathematical derivations):

$$\left(\boldsymbol{N}_1 + \boldsymbol{N}_2 + \cdots + \boldsymbol{N}_i\right) \cdot \boldsymbol{x} = \boldsymbol{b}_1 + \boldsymbol{b}_2 + \cdots + \boldsymbol{b}_i \tag{4.26}$$

and

$$\boldsymbol{l}^T\boldsymbol{P}\boldsymbol{l} = \left(\boldsymbol{l}^T\boldsymbol{P}\boldsymbol{l}\right)_1 + \left(\boldsymbol{l}^T\boldsymbol{P}\boldsymbol{l}\right)_2 + \cdots + \left(\boldsymbol{l}^T\boldsymbol{P}\boldsymbol{l}\right)_i. \tag{4.27}$$

It has to be noted that the normal equation system has to be constraint free before the stacking can be executed. The reason being that constraints are introduced to the normal equation system as pseudo observations. Consequently, they would be stacked as well, which is not desirable. In geodetic VLBI analysis, the constraints are removed before stacking the normal equation system and then applied to the stacked normal equation system.

4.2 Outlier detection in astrometric catalogs

The method of calculating parameters with the least squares method is not robust, which means that outliers in the data cannot be dealt with. Present outliers would be incorporated into the solution and this would affect the parameters in a negative way. Robust parameter estimation techniques exist, see Chapter 6 in Niemeier (2008), but in general, they are not

practical. The workaround for this problem is to find outliers before performing the parameter estimation. Many techniques for finding outliers exist. Here the method proposed by Mignard *et al.* (2016), which can be used when two celestial catalogs are compared, is presented.

Let us assume we have a source in a catalog with coordinates (α_1, δ_1) and their formal errors $(\sigma_{\alpha \cos \delta,1}, \sigma_{\delta_1})$ and a source in a second catalog with coordinates (α_2, δ_2) and their formal errors $(\sigma_{\alpha \cos \delta,2}, \sigma_{\delta_2})$. The difference in right ascension and declination can be calculated with

$$\Delta\alpha_{\cos \delta} = (\alpha_2 - \alpha_1) \cos \delta_1 \tag{4.28}$$

and

$$\Delta\delta = (\delta_2 - \delta_1) . \tag{4.29}$$

The angular separation can be found using basic Euclidean geometry, it reads:

$$\rho = \sqrt{\Delta\alpha_{\cos \delta}^2 + \Delta\delta^2}. \tag{4.30}$$

Note that these equations are only valid for small differences. However, they can easily be used since state of the art astrometric catalogs generally agree on the level of a couple of microarcsecond. The combined error of the difference in right ascension and declination can be calculated using Equation 4.31 and 4.32.

$$\sigma_{\alpha \cos \delta} = \sqrt{\sigma_{\alpha \cos \delta,2}^2 + \sigma_{\alpha \cos \delta,1}^2} \tag{4.31}$$

$$\sigma_\delta = \sqrt{\sigma_{\delta_2}^2 + \sigma_{\delta_1}^2} \tag{4.32}$$

Using the combined errors the normalized differences can be derived, they read:

$$X_\alpha = \frac{\Delta\alpha_{\cos \delta}}{\sigma_{\alpha \cos \delta}} \tag{4.33}$$

and

$$X_\delta = \frac{\Delta\delta}{\sigma_\delta}. \tag{4.34}$$

The normalized differences can be used to calculate the test quantity, it reads:

$$\chi^2 = \begin{pmatrix} X_\alpha & X_\delta \end{pmatrix} \begin{pmatrix} 1 & C \\ C & 1 \end{pmatrix}^{-1} \begin{pmatrix} X_\alpha \\ X_\delta \end{pmatrix}, \tag{4.35}$$

where

$$C = \frac{\sigma_{\alpha\cos\delta,2}\sigma_{\delta_2}c_2 + \sigma_{\alpha\cos\delta,1}\sigma_{\delta_1}c_1}{\sigma_{\alpha\cos\delta}\sigma_\delta}, \tag{4.36}$$

with c_1 and c_2 being the correlation coefficients of the source in catalog one and two respectively.

It is important to use Equation 4.35 to test for outliers since it contains the correlation of the data. This is particularly important when Gaia and VLBI positions are concerned since they can contain high correlation.

χ^2 should follow a chi-squared distribution with two degrees of freedom and consequently χ, called normalized separation, should follow a Rayleigh distribution. Note that this is only true when the errors follow a Gaussian normal distribution. The theoretical probability of χ being larger than a certain value x can be calculated using Equation 4.37.

$$Ps\left(\chi > x\right) = \exp\frac{-x^2}{2} \tag{4.37}$$

This can be used as a threshold for outlier detection. When a sample size of 2800 (roughly the number of common sources in ICRF3 and Gaia-CRF2) is assumed, then less than 0.5 sources should have a larger normalized separation than 4.2. Hence, sources with higher χ are considered outliers. Following the convention presented by Mignard *et al.* (2016) all sources with $\chi > 4.2$ are considered to be outliers. Further, sources with a large ($> 10mas$) angular separation, see Equation 4.30, are removed by Mignard *et al.* (2016) as well. The latter threshold is rather arbitrary and it was found that not including it in the outlier determination does not affect the parameters significantly. Therefore, it was decided to stick to the statistically sound approach, which means that this arbitrary threshold was not applied.

4.3   Correlation and covariance

In this section, the mathematical background of chosen chapters concerned with correlation and covariance is presented. First, the estimation of the correlation coefficient is discussed. This is needed when the correlation between estimated parameters is of interest. Second, the covariance of the difference of two random vectors is examined, which is needed when two astrometric catalogs are compared. Third, covariance error propagation is discussed. Within this thesis, covariance error propagation is needed to correctly propagate the errors when estimated parameters are used for further calculations.

4.3.1   Correlation of estimated parameters

The result of a LSM is a vector with estimates and a covariance matrix. The variances of the estimates can be found on the main diagonal of the covariance matrix while the covariances, which describe the dependency of the parameters, can be found off the main diagonal.

The covariances can be normalized using the variances of the concerned parameters. The parameter we derive by doing this is the correlation coefficient, it reads:

$$c_{XY} = \frac{\rho_{XY}}{\sigma_X \sigma_Y},$$

(4.38)

where the two parameters are denoted as X and Y with their formal errors (square root of variance) σ_X and σ_Y. The correlation coefficient between the parameters is denoted as c_{XY} and the covariance as ρ_{XY}.

4.3.2 Covariance of the difference of two random vectors

In order to investigate the difference of celestial reference frames one has to find intersecting sources, subtract their coordinates from one another and examine the difference. Hence, the observable for the least squares method is the difference in right ascension and declination ($\Delta\alpha$ and $\Delta\delta$). The weighting matrix (inverse of the covariance matrix) can be easily constructed when no covariances are concerned. However, when high correlations are present between right ascension and declination, as is the case for Gaia and VLBI catalogs, the whole covariance information has to be considered. Mignard *et al.* (2016) described the statistically correct procedure to calculate the covariance matrix of the difference of two random vectors. Let us assume we have two random vectors $\boldsymbol{x_1} = (x_1, y_1)$ and $\boldsymbol{x_2} = (x_2, y_2)$. Then their covariance matrices are

$$\boldsymbol{\Sigma_1} = \begin{pmatrix} \sigma_{x_1}^2 & \rho_1 \\ \rho_1 & \sigma_{y_1}^2 \end{pmatrix}$$

(4.39)

and

$$\boldsymbol{\Sigma_2} = \begin{pmatrix} \sigma_{x_2}^2 & \rho_2 \\ \rho_2 & \sigma_{y_2}^2 \end{pmatrix}.$$

(4.40)

The combined covariance matrix reads:

$$\boldsymbol{\Sigma} = \begin{pmatrix} \sigma_{x_1}^2 + \sigma_{x_2}^2 & \rho_1 + \rho_2 \\ \rho_1 + \rho_2 & \sigma_{y_1}^2 + \sigma_{y_2}^2 \end{pmatrix},$$

(4.41)

where ρ denotes the covariance and σ^2 the variance. Equation 4.38 can be used to calculate the covariance, if correlation coefficients are provided instead.

4.3.3 Covariance error propagation

When multiple variables are placed into a functional relation and more than one variable is afflicted with errors (they have formal uncertainties), the method of error propagation has to be used in order to derive the uncertainty of the result. The standard technique used in

geodesy is the so-called propagation of uncertainty. It is based on the assumption that errors follow a Gaussian distribution. The basic equation reads:

$$\sigma_f^2 = \sum_{i=1}^{n} \left(\left(\frac{\partial f}{\partial x_i} \right)^2 \cdot \sigma_{x_i}^2 \right),$$

(4.42)

where σ_f is the uncertainty of the result, $\frac{\partial f}{\partial x_i}$ is the partial derivative of the function f of several variables x_i with the formal errors σ_{x_i}. However, this standard equation does not allow for covariances between the variables. For stochastic dependent variables (covariances exist) Equation 4.42 has to be adapted. First, the n partial derivatives can be combined into one vector. Second, when m functions are present, they can be combined into a matrix:

$$\boldsymbol{F} = \begin{pmatrix} \frac{\partial f_1}{\partial x_1} & \frac{\partial f_1}{\partial x_2} & \cdots & \frac{\partial f_1}{\partial x_n} \\ \frac{\partial f_2}{\partial x_1} & \frac{\partial f_2}{\partial x_2} & \cdots & \frac{\partial f_2}{\partial x_n} \\ \vdots & \vdots & \ddots & \ddots \\ \frac{\partial f_m}{\partial x_1} & \frac{\partial f_m}{\partial x_2} & \cdots & \frac{\partial f_m}{\partial x_n} \end{pmatrix}.$$

(4.43)

$\boldsymbol{F}$ is called the functional matrix, where $f_1 \cdots f_m$ are the m functions and $x_1 \cdots x_n$ are the n variables, which are afflicted with errors. The matrix $\boldsymbol{F}$ is then used in the universal description of the propagation of uncertainty, which reads:

$$\Sigma_{ff} = \boldsymbol{F} \Sigma_{xx} \boldsymbol{F}^T,$$

(4.44)

where Σ_{ff} is the covariance matrix of the results and Σ_{xx} is the covariance matrix of the variables.

4.4 Comparing astrometric catalogs

4.4.1 Coordinate transformation

In order to evaluate systematic effects between catalogs a transformation model can be applied. The standard model used to compare celestial reference frames reads:

$$\Delta \alpha = A_1 \cos \alpha \sin \delta + A_2 \sin \alpha \sin \delta - A_3 + D_\alpha \left(\delta - \delta_0 \right)$$

(4.45)

and

$$\Delta \delta = -A_1 \sin \alpha + A_2 \cos \alpha + D_\delta \left(\delta - \delta_0 \right) + B_\delta,$$

(4.46)

where $\Delta \alpha$ and $\Delta \delta$ are the differences in right ascension and declination respectively; δ_0 is an arbitrary origin of declination; A_1, A_2 and A_3 are rotation angles around the three axes; D_α and D_δ are slopes in right ascension and declination as a function of declination; B_α represents

a bias in declination.

This model is recommended by the McCarthy, D. D. (1996). It was used to compare different solutions when the ICRF2 (Ma *et al.*, 2009) was constructed but also in more recent work, see Lambert (2014). However, this transformation has a privileged direction, which is the z-axis. A more general transformation is given by the vector spherical harmonics of degree 1, as described by Mignard & Klioner (2012).

4.4.2 Vector spherical harmonics

A thorough description of the VSH is provided in Mignard & Morando (1990) and further elaborated by Mignard & Klioner (2012). The short description of the technique presented in this section is based on the latter one.

The difference between two celestial reference frames can be described mathematically as a vector field on a sphere. Basically, the coordinate differences of n common sources is calculated. When the first frame has coordinates $\alpha_i^{(1)}$ and $\delta_i^{(1)}$ and the second frame $\alpha_i^{(2)}$ and $\delta_i^{(2)}$ and the differences are reasonably small (catalogs are close to each other) the difference can be calculated in a local tangential plane. The vector field is then described as

$$\mathbf{V} = [\Delta\alpha\cos\delta = \left(\alpha^{(2)} - \alpha^{(1)}\right)\cos\delta^{(1)}, \Delta\delta = \delta^{(2)} - \delta^{(1)}] \tag{4.47}$$

for the n common sources. Using the technique of VSH this field can be analyzed by the means of smaller base functions and larger and smaller features can be investigated.

Spherical harmonic decomposition is a well-known technique in geodesy. It is often used for the description of the Earth's gravity field. One could argue that using this recognized technique on the scalar fields, e.g. $\mathbf{V} = [\Delta\alpha\cos\delta]$ and $\mathbf{V} = [\Delta\delta]$ should be preferred. However, using VSH for the decomposition is not at all the same as expanding the two fields separately. The reason for that being that the separate expansion would be dependent on the coordinate system used while the VSH is independent of any coordinate system and, therefore, reveals the true geometric features of the field.

In principle, there is no end to the degree of the decomposition with higher degrees reflecting smaller details of the vector field. However, when small sample sizes are investigated the number of estimated parameters should not be too large. Furthermore, only the first degree can be linked to very global features such as rotation around the axes and a dipole displacement. The dipole can be described as a flow from a source to a sink located at two poles of an axis. Mignard & Klioner (2012) introduced the term glide for the dipole, which will be adopted here. It is defined as

$$\Delta\alpha\cos\delta = -D_1\sin\alpha + D_2\cos\alpha \tag{4.48}$$

and

$$\Delta\delta = -D_1 \cos\alpha\sin\delta - D_2\sin\alpha\sin\delta + D_3\cos\delta, \tag{4.49}$$

with D_1, D_2 and D_3 being the components of the glide for each axis. For readability reasons it was decided to use the notation from Titov & Lambert (2013) for the VSH. The second part of the first degree describes the rotation of the two catalogs, it reads as follows:

$$\Delta\alpha\cos\delta = R_1\cos\alpha\sin\delta + R_2\sin\alpha\sin\delta - R_3\cos\delta \tag{4.50}$$

and

$$\Delta\delta = -R_1\sin\alpha + R_2\cos\alpha, \tag{4.51}$$

where R_1, R_2 and R_3 are the rotation angles about the three axes. The second order describes a quadrupole:

$$\begin{aligned}
\Delta\alpha\cos\delta = &\, a_{2,0}^{M}\sin 2\delta \\
&+ \sin\delta\left(a_{2,1}^{E,Re}\sin\alpha + a_{2,1}^{E,Im}\cos\alpha\right) \\
&- \cos 2\delta\left(a_{2,1}^{M,Re}\cos\alpha - a_{2,1}^{M,Im}\sin\alpha\right) \\
&- 2\cos\delta\left(a_{2,2}^{E,Re}\sin 2\alpha + a_{2,2}^{E,Im}\cos 2\alpha\right) \\
&- \sin 2\delta\left(a_{2,2}^{M,Re}\cos 2\alpha - a_{2,2}^{M,Im}\sin 2\alpha\right)
\end{aligned} \tag{4.52}$$

and

$$\begin{aligned}
\Delta\delta = &\, a_{2,0}^{E}\sin 2\delta \\
&- \cos 2\delta\left(a_{2,1}^{E,Re}\cos\alpha - a_{2,1}^{E,Im}\sin\alpha\right) \\
&- \sin\delta\left(a_{2,1}^{M,Re}\sin\alpha + a_{2,1}^{M,Im}\cos\alpha\right) \\
&- \sin 2\delta\left(a_{2,2}^{E,Re}\cos 2\alpha - a_{2,2}^{E,Im}\sin 2\alpha\right) \\
&+ 2\cos\delta\left(a_{2,2}^{M,Re}\sin 2\alpha + a_{2,2}^{M,Im}\cos 2\alpha\right),
\end{aligned} \tag{4.53}$$

where a are the desired coefficients for the magnetic (M) and electric (E) types. These parameters (in this case 3 glide + 3 rotation + 10 quadrupole = 16) can be estimated using the least squares method, see Section 4.1.

The glide can be further investigated by calculating its amplitude and direction. The amplitude A is the norm of the glide vector:

$$A = \sqrt{D_1^2 + D_2^2 + D_3^2}. \tag{4.54}$$

Using the universal propagation of uncertainty (Equation 4.44) the formal error of the amplitude σ_A can be derived using the functional matrix

$$\boldsymbol{F} = \begin{pmatrix} \frac{D_1}{A} & \frac{D_2}{A} & \frac{D_3}{A} \end{pmatrix}. \tag{4.55}$$

In order to get the direction the glide vector has to be normalized with

$$d^{norm} = \begin{pmatrix} \frac{D_1}{A} \\ \frac{D_2}{A} \\ \frac{D_3}{A} \end{pmatrix}. \tag{4.56}$$

In addition, the uncertainty of the normalized glide vector with the functional matrix described by Equation 4.57 can be calculated with

$$\boldsymbol{F} = \begin{pmatrix} \frac{y^2+z^2}{A^3} & \frac{-y \cdot x}{A^3} & \frac{-z \cdot x}{A^3} \\ \frac{-x \cdot y}{A^3} & \frac{x^2+z^2}{A^3} & \frac{-z \cdot y}{A^3} \\ \frac{-x \cdot z}{A^3} & \frac{-y \cdot z}{A^3} & \frac{x^2+y^2}{A^3} \end{pmatrix}, \tag{4.57}$$

where x, y and z stand for the first, second and third entry in the d^{norm} vector. Then the normalized glide vector can be used to calculate the direction in right ascension and declination, see Equations 4.58 and 4.59 respectively.

$$\alpha_{glide}^{norm} = \arctan \frac{D_2^{norm}}{D_1^{norm}} \tag{4.58}$$

$$\delta_{glide}^{norm} = \arcsin D_3^{norm} \tag{4.59}$$

The uncertainty of the direction can then be calculated using the functional matrix described by Equation 4.60 and 4.61 respectively.

$$\boldsymbol{F} = \begin{pmatrix} \frac{-D_2^{norm}}{(D_1^{norm})^2+(D_2^{norm})^2} & \frac{-D_1^{norm}}{(D_1^{norm})^2+(D_2^{norm})^2} \end{pmatrix} \tag{4.60}$$

$$\boldsymbol{F} = \begin{pmatrix} \frac{1}{\sqrt{1-(D_3^{norm})^2}} \end{pmatrix} \tag{4.61}$$

It is easier to understand the VSH when the parameters are plotted over the unit sphere. For the convenience of the reader this is done in Figure 4.1 where the rotational parameters R_1, R_2 and R_3 are depicted. Further the glide parameters D_1, D_2 and D_3 as well as the first two second order parameters $a_{2,0}^e$ and $a_{2,0}^m$ are depicted. For completeness the rest of the second order parameters are depicted in Figure 4.2.
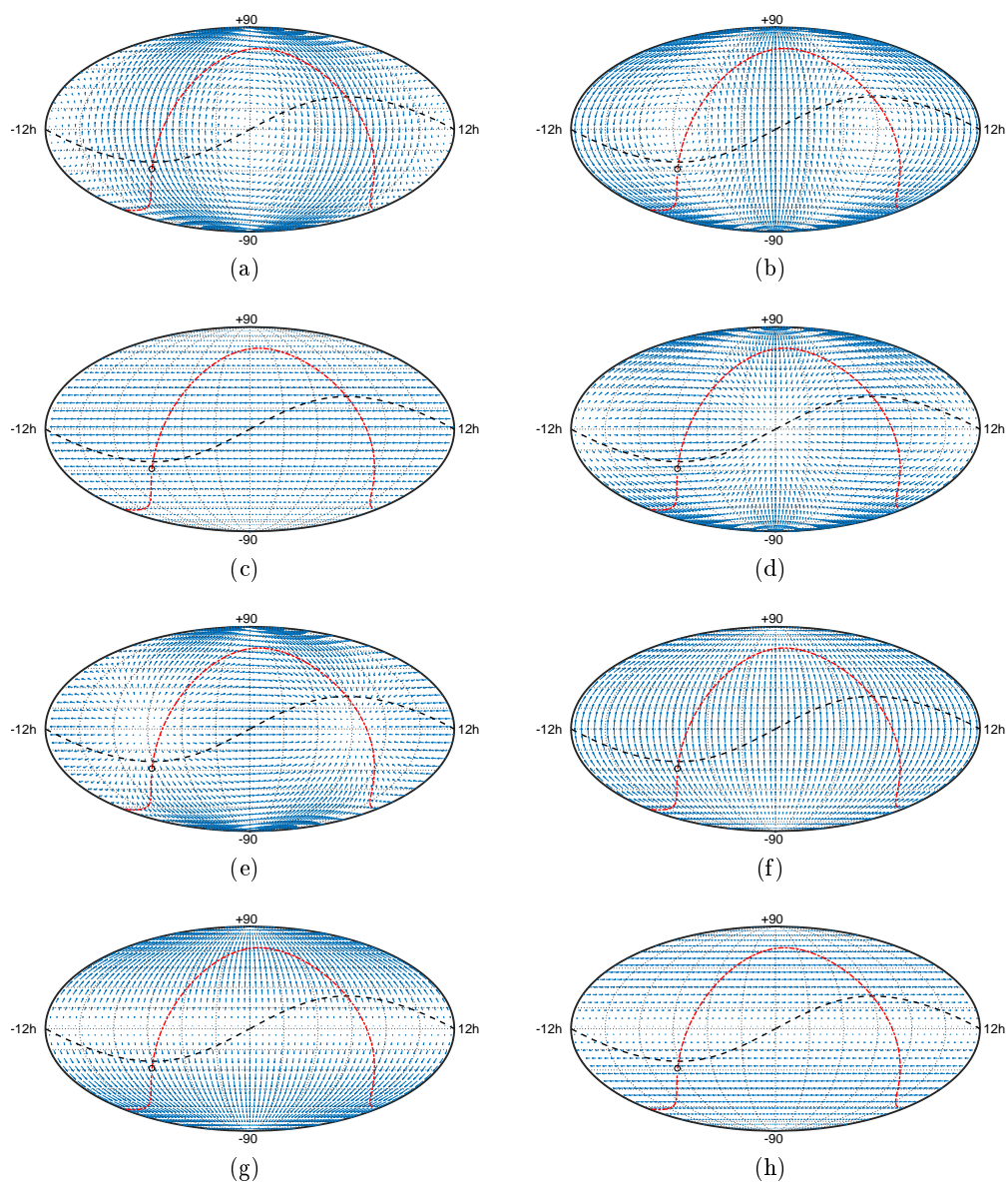
Figure 4.1: Depicted are the vector fields described by the (a) R_1, (b) R_2, (c) R_3, (d) D_1, (e) D_2, (f) D_3, (g) $a_{2,0}^e$ and (h) $a_{2,0}^m$ VSH parameters.
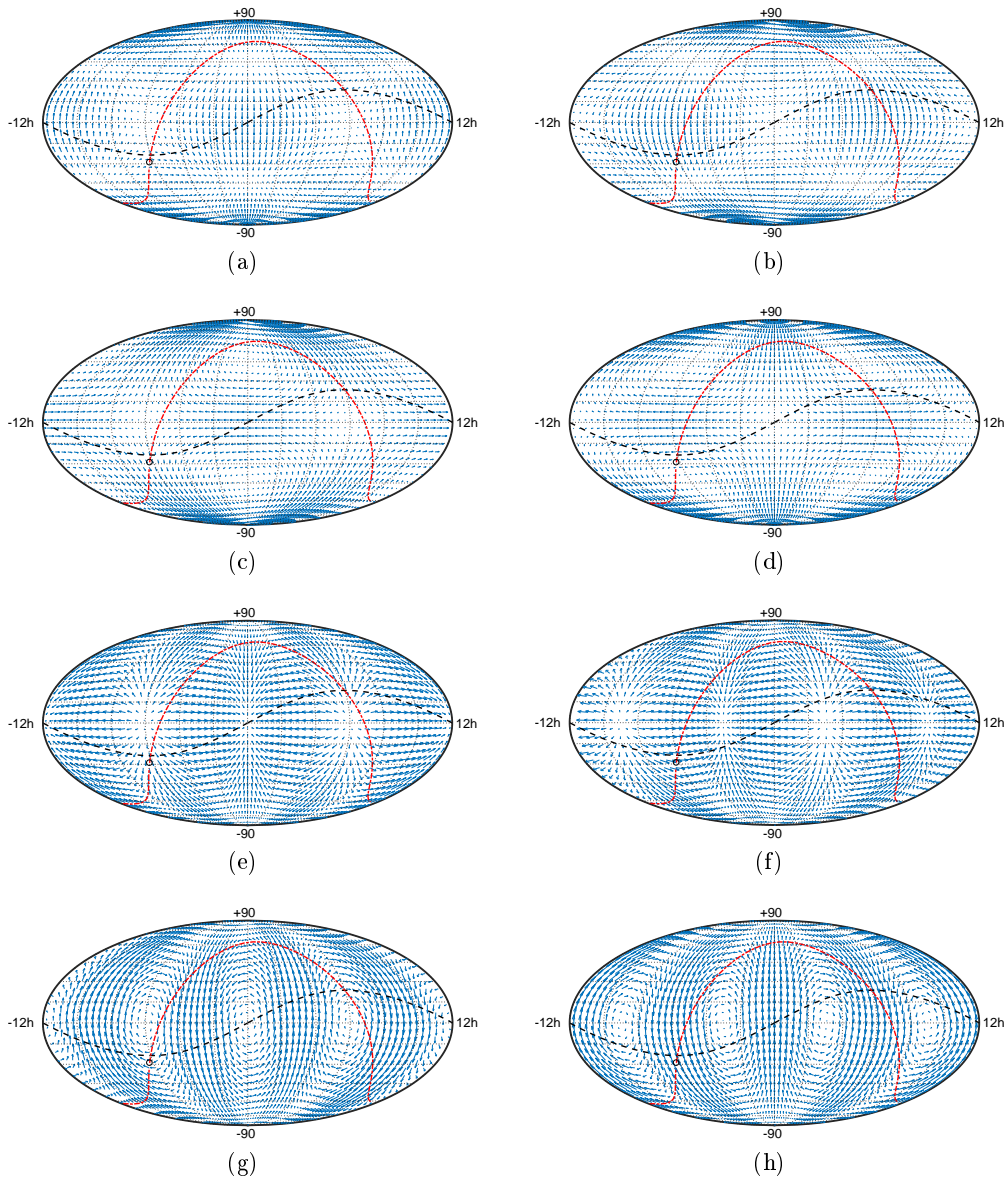
Figure 4.2: Depicted are the vector fields described by the (a) $a_{2,1}^{e,Re}$, (b) $a_{2,1}^{e,Im}$, (c) $a_{2,1}^{m,Re}$, (d) $a_{2,1}^{m,Im}$, (e) $a_{2,2}^{e,Re}$, (f) $a_{2,2}^{e,Im}$, (g) $a_{2,2}^{m,Re}$ and (h) $a_{2,2}^{m,Im}$ VSH parameters.

Chapter 5

Results and Discussion

5.1 The Vienna ICRF3 solution

In total about 12.8 million geodetic VLBI observations are utilized to create the Vienna ICRF3 solution from here on called Vie18. It incorporates 4482 sources with a solution fit χ^2/ndf of 0.88. Compared to the ICRF2 (3414 sources included) this is an increase of about 30 percent in sources.

The formal errors (not scaled yet) in declination, right ascension (scaled by $\cos\delta$) and the combined standard error ($\sqrt{\sigma_{\alpha\cos\delta}^2 + \sigma_\delta^2 + c \cdot \sigma_{\alpha\cos\delta}\sigma_\delta}$) of the Vie18 solution are depicted in Figure 5.1. They are plotted against the number of observations. If all errors would be Gaussian, the formal error would decrease with the square root of the observations; this is the blue line in the plot. It is evident that this behavior is true for most of the sources. However, sources which are observed more than ten thousand times deviate from the $\sqrt{N}$ rule. The general assumption of the least squares adjustment is that all observations are uncorrelated. There are multiple reasons why this does not hold in the real world. For once, observations from the same station go through the same observation set up and are, therefore, correlated. Further, the troposphere over one station adds spatial and temporal correlations to the observations. These correlations are rather small but can get problematic when many observations are concerned. Therefore, these effects are most evident when the most observed sources are considered. Their formal uncertainty does not improve when new observations are collected. Practically, this means that adding more observations to these sources only improves the position once the stochastic model is improved. The distribution of the formal uncertainties is depicted in Figure 5.2. One can see that the majority of sources have formal uncertainties of about 0.1 mas. Formal uncertainties are greater in declination than right ascension.

In Figure 5.3 the distribution of the 4482 sources in Vie18 is depicted. Further, the ICRF2 defining sources are added. These 295 sources define the rotation of the frame with the rest adding to the densification.
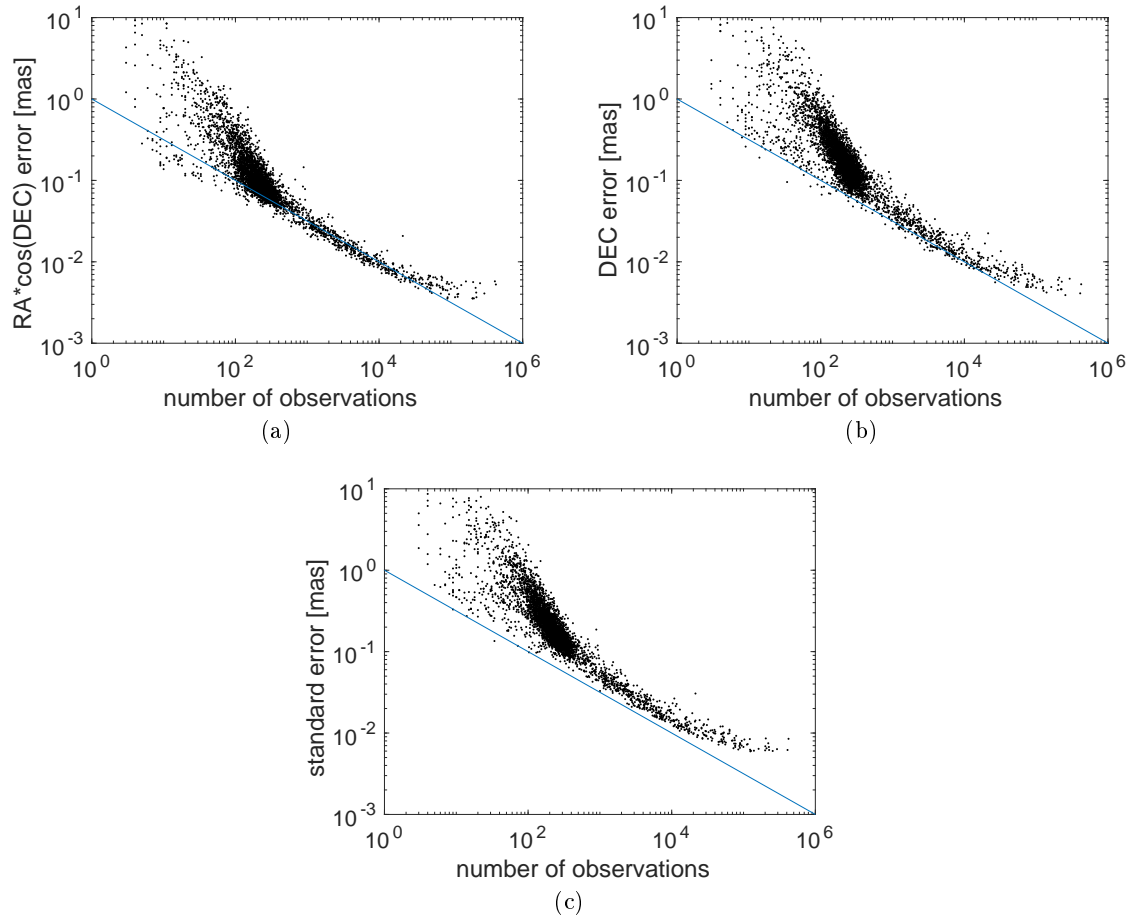
Figure 5.1: Formal errors in the Vie18 solution plotted against the number of observations. The blue line represents the decrease following the $\sqrt{N}$ rule. In the upper left plot the formal error in right ascension scaled by $\cos \delta$ is depicted, the upper right plot depicts the formal error in declination and the lower plot depicts the combined standard error.
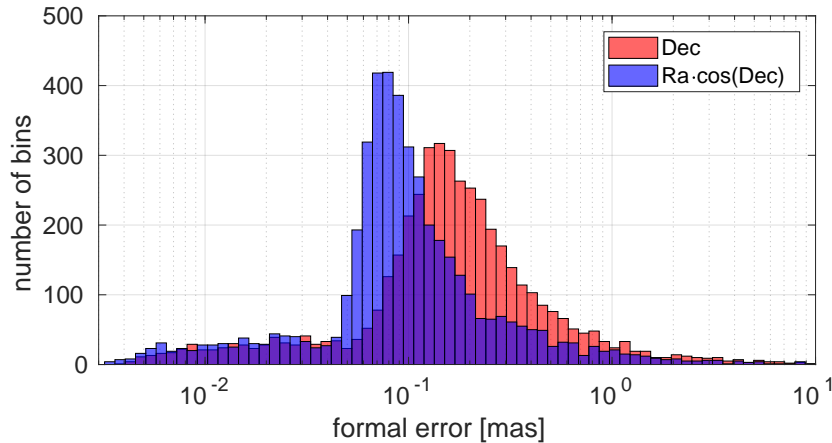
Figure 5.2: Distribution of formal uncertainties in Vie18. Note that the errors are not scaled in this solution. Hence, the difference to plots shown by Charlot *et al.* (2018).
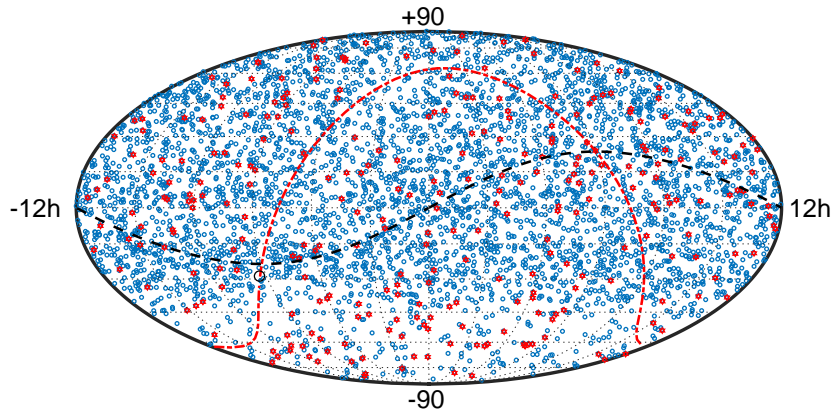
Figure 5.3: Distribution of sources in the Vie18 solution. Red stars denote the defining sources. The galactic plane is depicted in red with the center of the Galaxy denoted as a black circle. The ecliptic is depicted as a black dashed line.

5.1.1 Comparison to ICRF2

In Figure 5.4 the estimates w.r.t. ICRF2 are depicted. Most of the sources have small estimates below 1 mas. However, some larger values are present as well. These are either new sources, which had bad a priori values or VCS sources, which were only observed a couple of times for ICRF2 and were observed again for ICRF3.

When only looking at the defining sources, which are some of the best compact radio sources known, it is easier to see systematic differences between Vie18 and ICRF2. Differences in right ascension are for the most part randomly distributed. The declination differences between the Vie18 and ICRF2, however, show a systematic behavior when plotted against declination, see Figure 5.5. This rather distinct effect is called the declination bias.

The analysis of coordinate differences using the VSH technique can be used to describe systematic differences between astrometric catalogs. When calculating the VSH parameters between Vie18 and ICRF2 the values listed in Table 5.1 are found. The outlier elimination
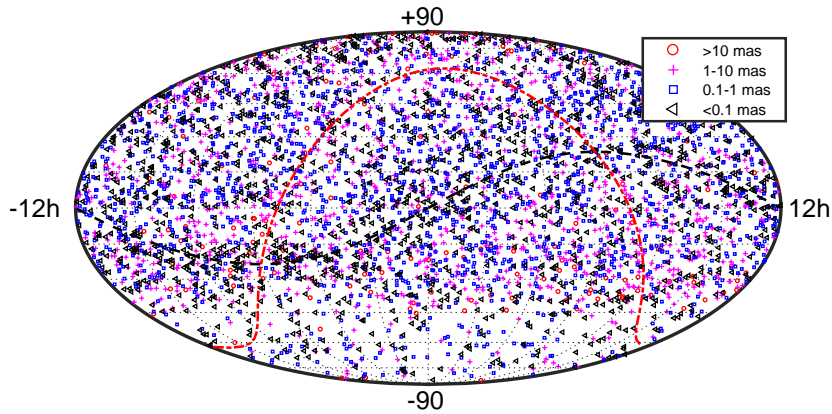
Figure 5.4: Estimates w.r.t. ICRF2 of the Vie18 solution. The galactic plane is depicted in red with the center of the Galaxy denoted as a black circle. The ecliptic is depicted as a black dashed line.
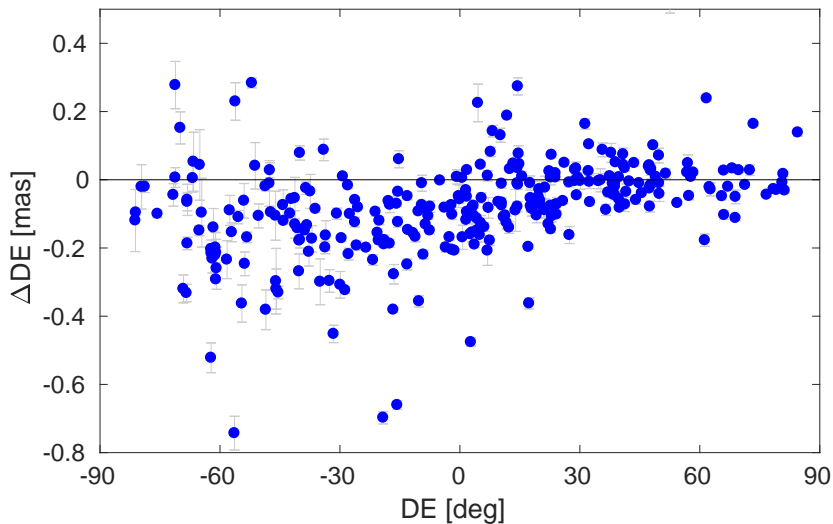
Figure 5.5: Declination estimates w.r.t. ICRF2 of the Vie18 solution plotted over declination. Only the defining sources are depicted here.

technique by Mignard *et al.* (2016) with a threshold of $\chi > 3$ was used to find outliers.

The rotation between these catalogs is very small which is not surprising since Vie18 and ICRF2 use the same set of defining sources. However, looking at the formal uncertainties one can see that the rotations are small but significant. One of the reasons for this is the fact that the Vie18 has formal errors which are not yet rescaled, hence, the significance of this results is overestimated. The other 13 VSH parameters describe deformations between the catalogs. Deformations of degree 1 are highly significant and reflect the declination bias between the two solutions, see Figure 5.5. The largest value for deformations between ICRF2 and Vie18 can be found in the D_3 parameter which reflects a deformation in declination. Further, a highly significant value is found for the $a_{2,0}^e$ parameters of degree 2, which is also connected to the source declination.

From the deformations of degree 1 it is possible to calculate the amplitude and direction

$[\mu as]$	Vie18
R_1	$+14 \pm 4$
R_2	$+10 \pm 4$
R_3	-7 ± 3
D_1	-19 ± 4
D_2	-57 ± 4
D_3	-86 ± 4
$a_{2,0}^{e}$	$+47 \pm 4$
$a_{2,0}^{m}$	$+7 \pm 3$
$a_{2,1}^{e,Re}$	-10 ± 4
$a_{2,1}^{e,Im}$	-1 ± 4
$a_{2,1}^{m,Re}$	$+4 \pm 4$
$a_{2,1}^{m,Im}$	-9 ± 4
$a_{2,2}^{e,Re}$	-1 ± 2
$a_{2,2}^{e,Im}$	$+3 \pm 2$
$a_{2,2}^{m,Re}$	-4 ± 2
$a_{2,2}^{m,Im}$	$+0 \pm 2$

Table 5.1: VSH parameters up to degree 2 between Vie18 and ICRF2.

Glide	Vie18
Glide Amplitude	$+105 \pm 4$
Glide RA	$+252 \pm 3$
Glide DEC	-55 ± 2

Table 5.2: Glide amplitude and position of VSH parameters up to degree 2 between Vie18 and ICRF2.

of the whole glide, see Table 5.2. When doing this the glide between Vie18 and ICRF2 is more than 100 µas, which is much larger than the noise floor reported by ICRF2 (40 µas).

In 2013 the AuScope network, see Plank *et al.* (2017) for more detail, started to observe. Especially, during 2014 and 2015 this network observed multiple sessions per week in addition to the IVS-R1 and IVS-R4 sessions where they participated as well. In total, the three Australian dishes account for about 860,000 observations of the 12.8 million total observations. To put this into perspective, the three Australian antennas make up about half of the total observations from the southern Hemisphere (about 2 million). All these observations happened after ICRF2 and the declination bias depicted in Figure 5.5 can be traced back to data from these antennas. In particular, the stations Hobart12 and Kath12m affect the declination of the sources. Removing them removes the declination bias. There are two possibilities for the difference. First, the ICRF2 is deformed and the new data corrects a systematic effect. A possible reason could be mismodeling of the tropospheric delays in ICRF2. Most of the observations to southern sources are from northern stations. These observations are all collected under low elevation angles, which in turn magnifies effects by the troposphere. It is conceivable that systematic effects from the troposphere could propagate into the declination

of the sources. In particular, the VLBA network that can observe sources down to about -40 degrees declination is responsible for many observations to southern sources. These observations are all collected under low elevation angles and since most of the sources are only observed by this network they are only observed under low elevations. The second possibility would be that the new data is somehow corrupted. In particular, a station dependent effect at the identically constructed Australian sites could have an influence similar to a bias in declination. The ICRF3 and ICRF2 utilize the same data from the same technique, hence, proving one of them wrong is a difficult task. In order to do this an independent source catalog is needed.

For the most part of VLBI history, a comparable celestial reference frame was simply not available at the accuracy needed. However, this has changed with the Gaia satellite mission, which was launched in 2013 and delivers source positions at accuracies comparable to VLBI. The Gaia reference frame can be used as an independent comparison for CRF solutions constructed using VLBI data and can help to understand systematic effects present in the current VLBI technique.

5.1.2 Comparison to Gaia

The Gaia-CRF2 is an optical realization of the ICRS and was published within the second data release in April 2018. It incorporates the positions of half a million quasars 2800 of which were found to have an ICRF3 counterpart. In its creation, the Gaia-CRF2 was rotated onto an ICRF3 prototype solution, which was provided by the ICRF3 working group. The formal errors of Gaia-CRF2 are on a similar magnitude as those of Vie18 with median formal uncertainties of 233 µas (scaled with $cos\delta$) in right ascension and 211 µas in declination for the Gaia-CRF2 and 136 µas (scaled with $cos\delta$) in right ascension and 240 µas in declination for Vie18 (with scaled formal uncertainties). Only the intersecting sources are used to calculate these values. Some of the common sources in Vie18 are only observed a couple of times by the VLBA and have, therefore, larger formal uncertainties while the distribution of formal uncertainties is more even for the Gaia-CRF2 catalog. In Table 5.3 VSH parameters up to degree 1 are listed. For each row a different outlier elimination techniques was used on the data set:

- In the first line the VSH parameters without any outlier testing are provided.

- In the second line the outlier test by Mignard *et al.* (2016) was used.

- In the third line the major axis of the error ellipse of the difference was calculated. If this value is larger than 2 mas the sources is flagged as an outlier.

- In the fourth line it is tested, if the normalized separation is larger than 5. This corresponds to a test where it is checked if the difference is larger than five times the combined sigma.

- In the fifth line the pure angular separation is looked at. If it is larger than 2 mas, the source is flagged as an outlier.

- In the sixth line it is checked, if the magnitude of the object is larger than 19, effectively, removing all faint objects.

- In the last three lines a threshold for the correlation between right ascension and declination of a source is introduced.

Gaia Collaboration *et al.* (2018b) and Petrov & Kovalev (2017) showed that the distribution of differences between ICRF3 and Gaia-CRF2 deviates from a standard Rayleigh distribution. This indicates that systematic effects are present between the catalogs. The two most conservative outlier elimination techniques, the Mignard *et al.* (2016) and the normalized separation technique, both assume that no systematic effects remain in the differences. As a consequence the outlier test described by Mignard *et al.* (2016) which is based on the Rayleigh distribution cannot be applied for this problem, since it would remove too many sources and in turn would mask systematic effects between these catalogs. The same holds true for the normalized separation technique. Further, VSH parameters from these tight outlier elimination techniques do differ from each other on a level of a couple of sigmas. Looking at the other outlier elimination techniques which introduce varying types of hard cutoffs no clear pattern emerges. This means that the VSH parameters are very susceptible to the outlier elimination technique.

Therefore, it was decided to use a more robust way to detect outliers, which does not remove systematic effects. Since Gaia-CRF2 and ICRF3 have only about 2800 intersecting sources (2782 for Gaia-CRF2 and Vie18) and the VSH are calculated rather quickly, it is possible to remove single sources and see the effect on the estimated parameters. This was realized by removing every source once from the data set, hence, ending up with a set of about 2800 VSH parameters. This series can then be checked for outliers with the assumption that a single source, which distorts the whole VSH parameters, is an outlier. What sets this technique apart from the ones listed in Table 5.3 is that only sources are removed which have a large impact on the VSH on their own. This means that, if a group of sources has a large offset directly in the same directions, they are not flagged as outliers but it is assumed that this is a systematic offset. With this method 194 sources (about 7%) are found to be outliers which in turn means that 2588 sources are left to calculate the VSH parameters. The number of found outliers is rather small for this technique compared to others, see Table 5.3 where the used sources of different outlier elimination techniques are listed. The repeatability of the VSH parameters after outlier elimination is depicted in Figures 5.6 and 5.7. One can see that further removing sources from the solution does not affect the transformation parameters by more than a couple of μas. Since the transformation parameters are susceptible to the selection of sources, this list of sources was used for all comparisons.

When comparing the Vie18 solution to Gaia using the VSH approach and the outlier

	sources	R_1	R_2	R_3	D_1	D_2	D_3
no test	2782	-37 ± 35	$+47\pm33$	$+6\pm31$	-26 ± 34	$+81\pm33$	$+50\pm34$
Mignard *et al.* (2016)	1976	-16 ± 7	$+30\pm7$	-9 ± 7	-4 ± 7	$+6\pm7$	$+16\pm7$
error ellipse > 2mas	2401	-41 ± 37	$+49\pm34$	$+9\pm33$	-28 ± 35	$+85\pm34$	$+49\pm35$
norm. sep. > 5	2391	-18 ± 8	$+21\pm8$	-14 ± 8	-6 ± 8	$+18\pm8$	$+2\pm8$
ang. sep. > 2mas	2444	-40 ± 10	$+65\pm10$	-33 ± 9	$+2\pm10$	$+26\pm10$	$+37\pm10$
magnitude > 19	1514	-47 ± 47	$+56\pm43$	$+9\pm42$	-39 ± 45	$+85\pm43$	$+52\pm45$
corr in DR2 > 0.8	2761	-37 ± 35	$+46\pm33$	$+6\pm32$	-26 ± 34	$+81\pm33$	$+49\pm34$
corr in DR2 > 0.6	2648	-35 ± 36	$+43\pm34$	$+10\pm33$	-22 ± 35	$+80\pm34$	$+38\pm35$
corr in DR2 > 0.4	2254	-36 ± 41	$+42\pm38$	$+3\pm38$	-23 ± 39	$+87\pm38$	$+61\pm41$

Table 5.3: VSH parameters between Vie18 and Gaia-CRF2 up to degree 1 with different outlier selection.
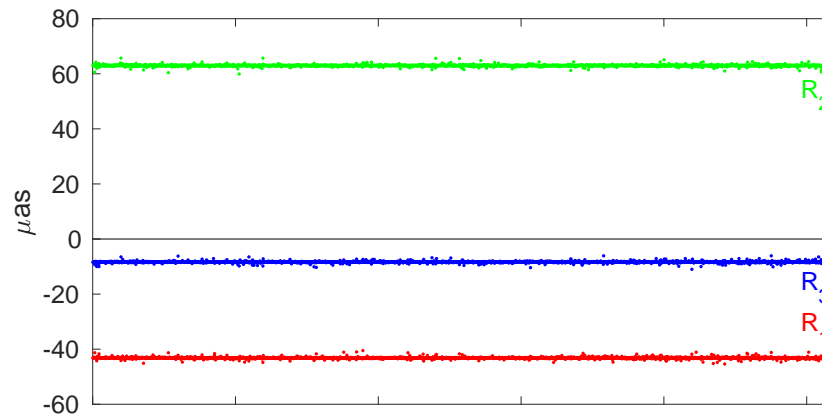
Figure 5.6: Repeatability of VSH rotation parameters after outlier elimination. Each dot represents a solution where one of the sources is excluded. The x-axis refers to the 2782 solutions.
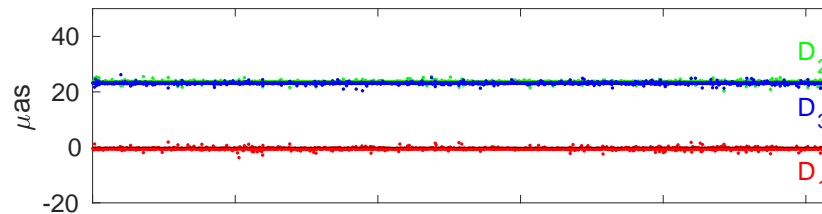

Figure 5.7: Repeatability of VSH glide parameters after outlier elimination. Each dot represents a solution where one of the sources is excluded. The x-axis refers to the 2782 solutions.

elimination technique described above the parameters listed in Table 5.4 are found. The Gaia celestial reference frame is oriented using a prototype solution provided by the ICRF3 working group, see Lindegren *et al.* (2018). This means that the rotational parameters between ICRF3 and Gaia-CRF2 should be negligible. However, large rotations are present in Table 5.4. The reason for this rather large discrepancy is manifold. First, the Vie18 solution compared here differs from the prototype solution provided to the Gaia team in terms of data. To be exact, the Vie18 solution includes data until March 2018 while the prototype solution includes data until November 2017. Second, the analysis differs as well. Different software (different models and estimation techniques) was used and different analysts evaluated the data. While the Vie18 solution is constructed using the VieVS software, the solution used to orient Gaia was created using the Calc/Solve solution. Third, the probably bigger reason for significant rotations is the selection of sources and the outlier elimination technique. While 2844 sources are used to orient the Gaia-CRF2 onto the ICRF3 (these were used in the second primary solution - in a later selection the previously reported 2820 source were found, see Lindegren *et al.* (2018) for more detail) the values presented here are only calculated from a subset of 2588 sources. As described above the outlier elimination technique removes the sources that have the most impact on the VSH parameters. Therefore, large rotations are to be expected. The more interesting differences between the catalogs are the deformations. Looking at the deformations of degree 1, which are the glide parameters, it is evident that significant deformations are present between the two catalogs. Further, the $a_{2,0}^e$ parameter of

67

$[\mu as]$	Vie18
R_1	-46 ± 16
R_2	$+60 \pm 15$
R_3	-11 ± 14
D_1	-1 ± 15
D_2	$+28 \pm 15$
D_3	$+20 \pm 15$
$a_{2,0}^{e}$	$+68 \pm 17$
$a_{2,0}^{m}$	$+8 \pm 15$
$a_{2,1}^{e,Re}$	$+17 \pm 18$
$a_{2,1}^{e,Im}$	-0 ± 19
$a_{2,1}^{m,Re}$	$+8 \pm 19$
$a_{2,1}^{m,Im}$	$+3 \pm 19$
$a_{2,2}^{e,Re}$	$+6 \pm 9$
$a_{2,2}^{e,Im}$	$+2 \pm 9$
$a_{2,2}^{m,Re}$	$+0 \pm 9$
$a_{2,2}^{m,Im}$	-8 ± 9

Table 5.4: VSH parameters up to degree 2 between Vie18 and Gaia-CRF2.

Glide	Vie18
Glide Amplitude	$+36 \pm 15$
Glide RA	$+93 \pm 32$
Glide DEC	$+39 \pm 24$

Table 5.5: Glide amplitude and position of VSH parameters up to degree 2 between Vie18 and Gaia-CRF2.

degree 2 is highly significant.

Gaia Collaboration *et al.* (2018b) did similar comparisons arriving at comparable magnitudes. However, it is important to mention here that they compare the Gaia-CRF2 exactly to the prototype solution, which means that the values reported there should be smaller than the values reported here.

From the deformation of degree 1 it is possible to calculate the direction and the amplitude of the dipole, this is listed in Figure 5.5. The direction of the dipole is for the most part rather close to the galactic anticenter (the Galactic Center is at $17h45min40sec$ in right ascension and $-29^o00'28''$ in declination). This indicates that the main deformational difference between Gaia-CRF2 and Vie18 is due to galactic aberration.

The correlations between the VSH parameters are listed in Table 5.6. It shows that for the most part correlations between the parameters are small with the largest positive correlation of 0.37 between R_2 and D_1 and largest negative correlation of -0.37 between R_1 and D_2. These small values indicate that the parameter separation is quite stable. For the coming comparisons the correlations between parameters are omitted.

	R_1	R_2	R_3	D_1	D_2	D_3
R_2	+0.08					
R_3	-0.18	-0.21				
D_1	+0.04	+0.37	-0.20			
D_2	-0.37	-0.04	+0.08	-0.07		
D_3	+0.17	-0.03	-0.00	+0.00	-0.00	
$a_{2,0}^{e}$	-0.09	+0.16	+0.01	-0.05	+0.04	-0.29
$a_{2,0}^{m}$	-0.04	-0.11	+0.26	-0.27	+0.25	-0.03
$a_{2,1}^{e,Re}$	+0.03	+0.19	-0.10	+0.28	-0.02	-0.03
$a_{2,1}^{e,Im}$	+0.06	+0.01	-0.10	-0.02	-0.28	-0.11
$a_{2,1}^{m,Re}$	-0.31	-0.03	+0.07	-0.07	+0.26	-0.13
$a_{2,1}^{m,Im}$	+0.04	+0.31	+0.03	+0.09	-0.05	-0.17
$a_{2,2}^{e,Re}$	-0.07	-0.12	-0.03	-0.03	+0.12	-0.01
$a_{2,2}^{e,Im}$	-0.07	+0.09	-0.11	+0.13	+0.02	+0.02
$a_{2,2}^{m,Re}$	-0.03	-0.09	+0.01	-0.15	-0.16	-0.07
$a_{2,2}^{m,Im}$	-0.12	-0.03	-0.02	-0.17	+0.16	-0.14

Table 5.6: Correlation of VSH parameters up to degree 2 between Vie17 and Gaia. To improve readability the correlations between the quadrupole parameters is omitted. The largest correlation between quadrupole parameters is -0.25 ($a_{2,2}^{e,Re}$ and $a_{2,1}^{e,Re}$).

The VSH parameters listed in Table 5.4 can be visualized by plotting them on a sphere. Figure 5.8, 5.9 and 5.10 depict the same information as Table 5.4. However, visualizing these values helps the human eye interpreting these values. For example, looking at Figure 5.9 it is now even clearer that the glide between Vie18 and Gaia-CRF2 is very close to the imprint of proper motions expected by GA. Further, looking at Figure 5.10 it is more clear what a quadrupole deformation with a highly significant $a_{2,0}^{e}$ parameter looks like.
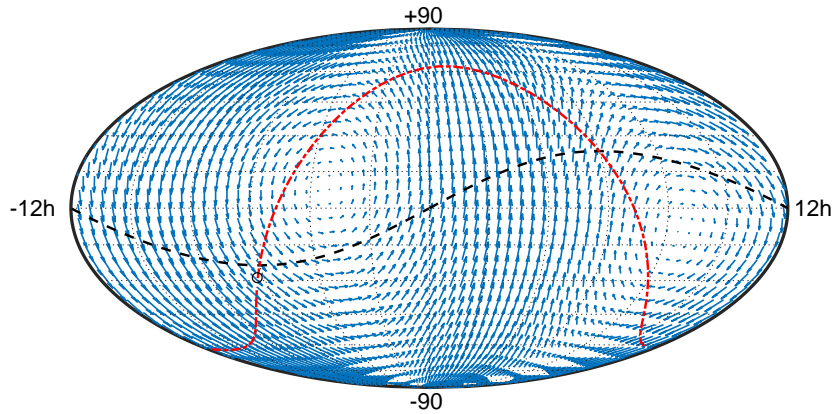

Figure 5.8: Rotation between Vie18 and Gaia-CRF2. The largest arrow is of size $76\mu as$. The galactic plane is depicted in red with the center of the Galaxy denoted as a black circle. The ecliptic is depicted as a black dashed line.

.

Figure 5.9: Glide between Vie18 and Gaia-CRF2. The largest arrow is of size $36\mu as$. The galactic plane is depicted in red with the center of the Galaxy denoted as a black circle. The ecliptic is depicted as a black dashed line.

Figure 5.10: VSH parameter of degree 2 between Vie18 and Gaia-CRF2. The largest arrow is of size $91\mu as$. The galactic plane is depicted in red with the center of the Galaxy denoted as a black circle. The ecliptic is depicted as a black dashed line.
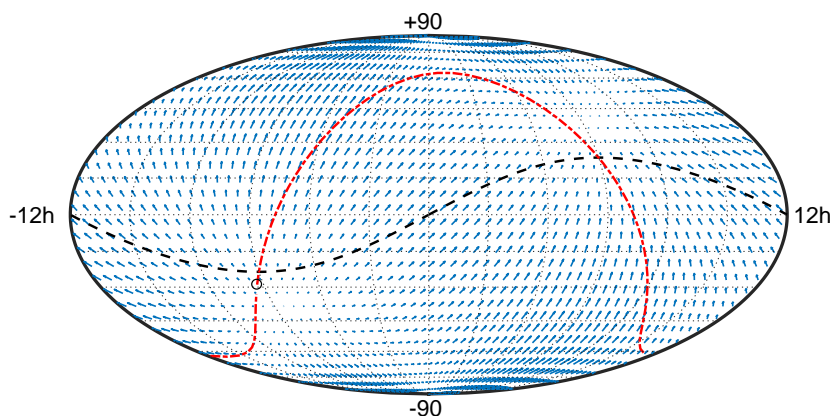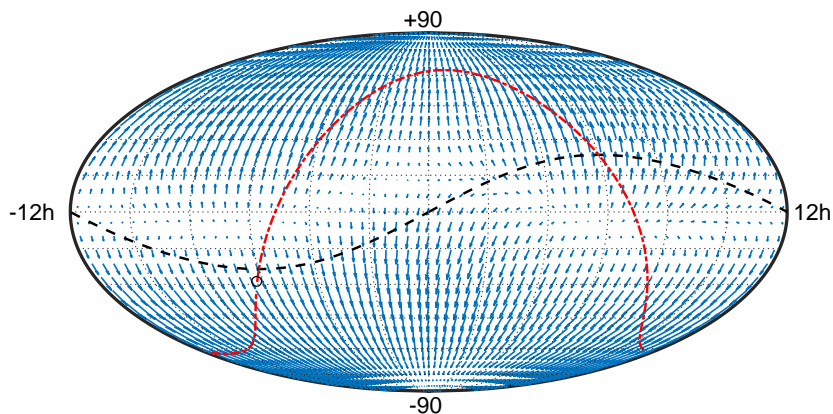
5.1.3   Estimated EOP

When calculating a CRF in a global solution the usual approach is to reduce the EOP, which means that they are calculated per session. In a second run, the so-called backward solution, the EOP can be calculated and used as quality criteria. The EOP estimates from the Vie18 solution w.r.t. the IERS 14 C04 time series are depicted in Figures 5.11, 5.12 and 5.13. A small feature is visible in the polar motion in 2015. Further, it is evident that some strange behavior is visible in dUT1. It is not clear, if this is a real behavior or inherent to the IERS 14 C04 time series.

Marking the AUSTRAL network (Plank *et al.*, 2017) sessions in the time series reveals that the small feature around 2015 mentioned above originates from these sessions, see red crosses in Figure 5.14. The AUSTRAL sessions are regional (Australia) with the addition of Hart15m (South Africa) and Wark12m (New Zealand) from time to time. Malkin (2009)

Figure 5.11: Time series of polar motion estimates w.r.t. IERS 14 C04 from a backward solution of the Vie18 solution.

Figure 5.12: Time series of dUT1 estimates w.r.t. IERS 14 C04 from a backward solution of the Vie18 solution.

Figure 5.13: Time series of nutation estimates w.r.t. IERS 14 C04 from a backward solution of the Vie18 solution.

showed that the EOP quality is directly connected to the networks size (in terms of volume). This means that a regional network such as the AUSTRAL network will not deliver reasonable

EOP. When comparing the EOP from the AUSTRAL sessions with the EOP from IVS-R1 and IVS-R4 sessions (blue circles in Figure 5.14), which generally have a large observing network, the difference in scatter is distinct. It is possible to explain this certain rise in EOP scatter with the beginning of tight observing schedule of the AUSTRAL network in 2014.
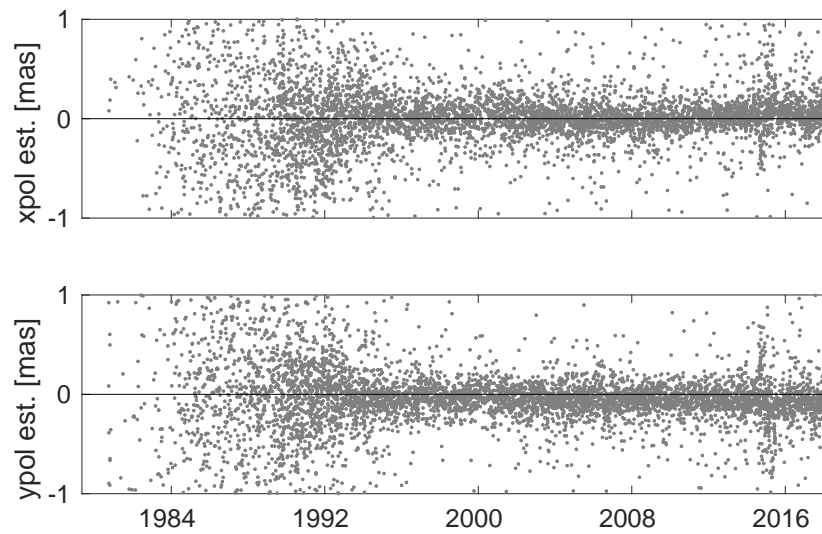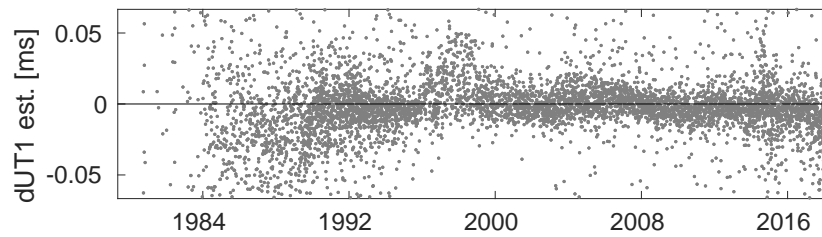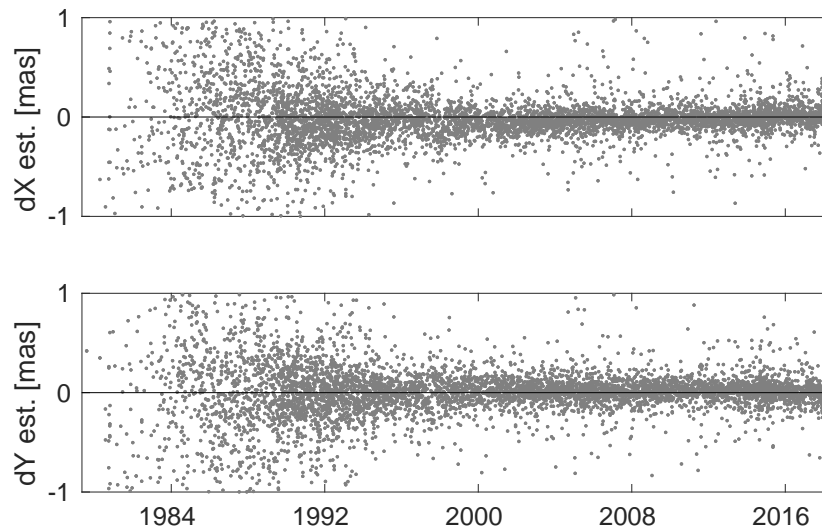

Figure 5.14: Time series of polar motion estimates w.r.t. IERS 14 C04 from a backward solution of the Vie18 solution. Estimates from IVS-R1 and IVS-R4 sessions are marked with blue circles and estimated from the AUSTRAL sessions are marked with red crosses.

AUSTRAL sessions do not stand out when the general EOP scatter due to small networks is considered, see Figure 5.15 where networks which have a smaller volume than $5 \cdot 10^{19} m^3$ are marked with red crosses. The largest volume for the AUSTRAL sessions is $4.5 \cdot 10^{19} m^3$, which is reached when Hart15m and Wark12m join the core network.
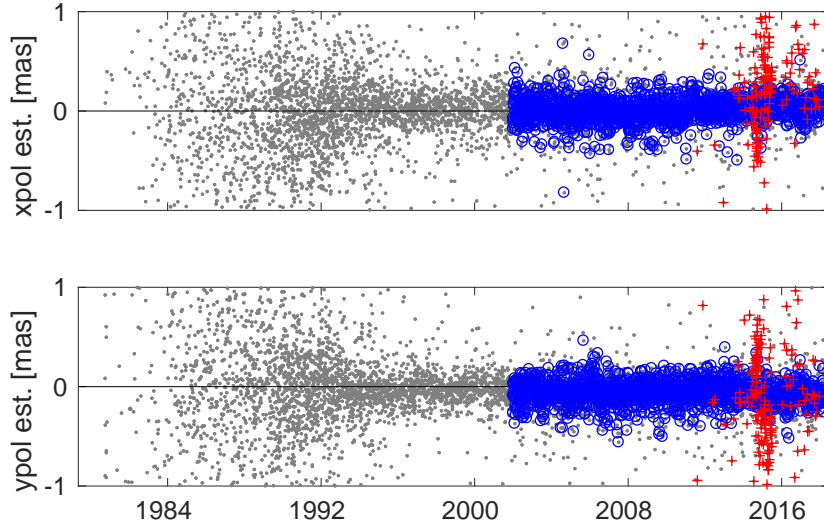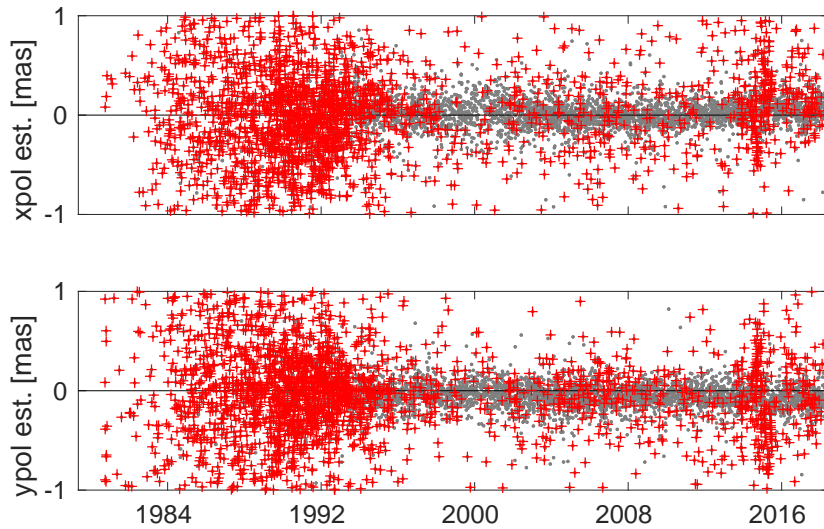

Figure 5.15: Time series of polar motion estimates w.r.t. IERS 14 C04 from a backward solution of the Vie18 solution. Estimates from small networks (network volume smaller than $5 \cdot 10^{19} m^3$) are depicted with red crosses.

	All sessions	IVS-R1 and IVS-R4 sessions	AUSTRAL sessions	Regional networks
xpol wrms [μas]	127	89	393	413
ypol wrms [μas]	119	90	358	371
dUT1 wrms [μs]	12	8	28	27
dX wrms [μas]	103	64	112	239
dY wrms [μas]	96	61	130	239

Table 5.7: WRMS values of EOP from different session types. All estimates larger than 10 mas were removed before the calculation.

WRMS values of the different session types are listed in Table 5.7. The EOP values are best determined with the IVS-R1 and IVS-R4 sessions as was expected. These values are comparable to those published by Bachmann *et al.* (2016).

5.1.4 Estimated special handling sources

Similar to the EOP a time series of the reduced source coordinates can be calculated in a backward solution. In the Vie18 solution, the 39 special handling sources are reduced. The reason for this is that these sources were reduced during the creation of ICRF2. Figure 5.16 depicts one of these sources which experiences a non-white noise behavior. Using 4C39.25 as an example, one can see the significant variability of the special handling sources. A median position for these sources can be calculated from the time series and a fitting formal error can be calculated by deriving the WRMS.
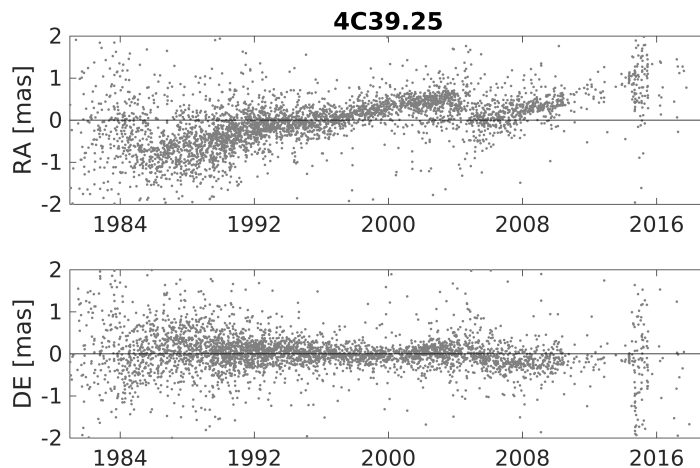

Figure 5.16: Time series of declination and right ascension coordinates of special handling source 4C39.25. Derived from a backward solution of Vie18.

5.2   Various CRF solutions

In this section, the Vie18 solution is modified in many different ways, which include various models and analysis strategies. The resulting solutions are compared against the Gaia-CRF2 catalog using the outlier list that was used for Vie18.

5.2.1   Antenna axis offset

An uncorrected axis offset could potentially result in an elevation dependent effect, which in turn would affect the declination of sources. This effect would be most prevalent in the Southern Hemisphere. The reason for this being the lack of stations in the south resulting in a weak network geometry. Therefore, a solution was created where the axis offset of the most prominent far southern stations was estimated alongside the other parameters. This solution is called Vie18-AOest. The VSH parameters of Vie18-AOest and Gaia-CRF2 are listed in Table 5.8. One can see that compared to Vie18 the transformation parameters are almost (only a small increase in D_3) not affected. This indicates that the handling of the antenna axis offset is sufficient and that uncorrected offsets of southern stations do not deform the CRF significantly.

5.2.2   Antenna axis offset altitude correction

A minor effect, which is not included into the standard VieVS delay model is the antenna axis offset altitude correction. This model corrects small variations in zenith troposphere delays due to antenna axis offsets. It is rather small (1 to 2 mm in zenith) and only has to be considered for stations with a vertically moving second axis (X-Y and Equatorial mounts). However, this effect is elevation dependent and can, therefore, change source declinations. In order to test the impact of this model its effect was corrected in the Vie18-AOaltitudeCorr solution. The VSH parameters of Vie18-AOaltitudeCorr and Gaia-CRF2 are listed in Table 5.8. Comparing to Vie18 one can see a small increase of the D_3 parameter the impact on the other parameters is negligible. Therefore, it can be concluded that the influence of this model is small with insignificant deformations on the CRF.

5.2.3   Troposphere delay modeling

Mayer *et al.* (2017) showed that tropospheric delay modeling choices could affect the celestial reference frame significantly. Especially, a priori ray-traced delays are shown to have an impact on source declination. In this section, the influence of tropospheric delay modeling on the celestial reference frame will be closely examined.

5.2.3.1   Choice of a priori gradients

A new model for a priori gradients developed by Landskron *et al.* (2015) was published in 2015. It is called the GRAD model and was developed at the Department of Geodesy

$[\mu as]$	Vie18	Vie18-AOest	Vie18-AOaltitudeCorr
R_1	-46 ± 16	-46 ± 16	-46 ± 16
R_2	$+60 \pm 15$	$+62 \pm 15$	$+60 \pm 15$
R_3	-11 ± 14	-12 ± 14	-11 ± 14
D_1	-1 ± 15	-2 ± 15	-1 ± 15
D_2	$+28 \pm 15$	$+29 \pm 15$	$+28 \pm 15$
D_3	$+20 \pm 15$	$+24 \pm 15$	$+24 \pm 15$
$a_{2,0}^{e}$	$+68 \pm 17$	$+68 \pm 17$	$+67 \pm 17$
$a_{2,0}^{m}$	$+8 \pm 15$	$+7 \pm 15$	$+8 \pm 15$
$a_{2,1}^{e,Re}$	$+17 \pm 18$	$+17 \pm 18$	$+17 \pm 18$
$a_{2,1}^{e,Im}$	-0 ± 19	-1 ± 19	-0 ± 19
$a_{2,1}^{m,Re}$	$+8 \pm 19$	$+9 \pm 19$	$+8 \pm 19$
$a_{2,1}^{m,Im}$	$+3 \pm 19$	$+2 \pm 19$	$+3 \pm 19$
$a_{2,2}^{e,Re}$	$+6 \pm 9$	$+6 \pm 9$	$+6 \pm 9$
$a_{2,2}^{e,Im}$	$+2 \pm 9$	$+2 \pm 9$	$+2 \pm 9$
$a_{2,2}^{m,Re}$	$+0 \pm 9$	$+1 \pm 9$	$+0 \pm 9$
$a_{2,2}^{m,Im}$	-8 ± 9	-8 ± 9	-8 ± 9

Table 5.8: VSH parameters up to degree 2 between Vie18-AOest/Vie18-AOaltitudeCorr and Gaia-CRF2.

and Geoinformation at the Technische Universität Wien, Vienna, Austria[1]. In this model a numerical weather models is used to predict a 6 h time series of a priori gradients. It is based on ray-traced delays, which are calculated by the program RADIATE, see Hofmeister & Böhm (2017). Using this more refined model for a priori gradients does not significantly change the VSH parameters compared to the reference solution where the DAO model is used, see Table 5.9.

Removing the a priori gradients completely from the solution does change the D_3 and $a_{2,0}^{e}$ parameter significantly, see solution Vie18-NoAPrioriGrad in Table 5.9. However, this is not due to the a priori gradients but rather due to the absolute constraints, which are too tight without a priori gradients. Solution Vie18-NoAPrioriGrad-noAbsGradConst in Table 5.9 lists the VSH parameters when no a priori gradients are used and the absolute constraints are loosened. It is evident that the large increase in D_3 and $a_{2,0}^{e}$ is no longer present. Comparing these VSH parameters to Table 5.12 where VSH parameters of solution Vie18-noAbsGradConst (a priori gradients from DAO model and loose absolute constraints) are presented one can see that they are almost identical. This indicates that the choice of a priori gradient model does not affect the CRF significantly, if the right constraints are chosen.

---

[1] http://vmf.geo.tuwien.ac.at

$[\mu as]$	Vie18	Vie18-GRAD	Vie18-NoAPrioriGrad	Vie18-NoAPrioriGrad-noAbsGradConst
R_1	-46 ± 16	-47 ± 16	-45 ± 16	-49 ± 16
R_2	$+60 \pm 15$	$+61 \pm 15$	$+62 \pm 15$	$+59 \pm 15$
R_3	-11 ± 14	-11 ± 14	-12 ± 14	-9 ± 14
D_1	-1 ± 15	-2 ± 16	-2 ± 15	-2 ± 16
D_2	$+28 \pm 15$	$+28 \pm 15$	$+28 \pm 15$	$+27 \pm 15$
D_3	$+20 \pm 15$	$+23 \pm 15$	$+58 \pm 15$	-2 ± 15
$a_{2,0}^{e}$	$+68 \pm 17$	$+69 \pm 17$	$+82 \pm 17$	$+69 \pm 17$
$a_{2,0}^{m}$	$+8 \pm 15$	$+8 \pm 15$	$+8 \pm 15$	$+8 \pm 15$
$a_{2,1}^{e,Re}$	$+17 \pm 18$	$+16 \pm 18$	$+16 \pm 18$	$+17 \pm 18$
$a_{2,1}^{e,Im}$	-0 ± 19	-1 ± 19	$+1 \pm 19$	-1 ± 19
$a_{2,1}^{m,Re}$	$+8 \pm 19$	$+8 \pm 19$	$+8 \pm 19$	$+7 \pm 19$
$a_{2,1}^{m,Im}$	$+3 \pm 19$	$+2 \pm 19$	$+2 \pm 19$	$+2 \pm 19$
$a_{2,2}^{e,Re}$	$+6 \pm 9$	$+7 \pm 9$	$+6 \pm 9$	$+6 \pm 9$
$a_{2,2}^{e,Im}$	$+2 \pm 9$	$+1 \pm 9$	$+2 \pm 9$	$+2 \pm 9$
$a_{2,2}^{m,Re}$	$+0 \pm 9$	$+0 \pm 9$	$+0 \pm 9$	$+1 \pm 9$
$a_{2,2}^{m,Im}$	-8 ± 9	-8 ± 9	-7 ± 9	-8 ± 9

Table 5.9: VSH parameters up to degree 2 between Vie18-GRAD and Gaia-CRF2.

5.2.3.2 A priori ray-traced delays

An interesting new troposphere delay modeling approach was developed recently. It is called ray-tracing and uses numerical weather data to predict the slant path delay through the troposphere for each observation. Two groups (Eriksson *et al.* (2014) and Hofmeister & Böhm (2017)) developed independent software, which uses different numerical weather models to derive these delays and tested those using VLBI data. They found that the technique is an interesting alternative to conventional tropospheric modeling and that the baseline length repeatability of most baselines is decreased. However, the influence of this new approach on source coordinates was not discussed. This was first done by Mayer *et al.* (2017) who showed that using ray-tracing to model a priori slant delay deforms the celestial reference frame. However, the assessment of this change is difficult without an independent source to test the reference frame. With the Gaia-CRF2 such an independent reference frame exist and can be used to test the influence of ray-traced a priori tropospheric delays on the CRF. Ray-traced delays were generated for the whole data set that was used for Vie18 using the program RADIATE, see Hofmeister (2016). These were then used in the VLBI analysis, see Table 5.10 for the VSH between the resulting CRF (Vie18-RayTrace) and Gaia-CRF2.

Using ray-traced delays a priori significantly reduces the $a_{2,0}^{e}$ parameter. This result is interesting since this parameter is one of the largest differences between Vie18 and Gaia-CRF2 and reducing it is a good indicator for the advantage of using ray-traced delays in the VLBI analysis. It has to be noted here that while the $a_{2,0}^{e}$ parameter is reduced the

$[\mu as]$	Vie18	Vie18-RayTrace	Vie18-RayTrace-noAbsGradConst
R_1	-46 ± 16	-50 ± 16	-53 ± 16
R_2	$+60 \pm 15$	$+61 \pm 15$	$+59 \pm 15$
R_3	-11 ± 14	-7 ± 14	-4 ± 14
D_1	-1 ± 15	$+2 \pm 15$	$+1 \pm 15$
D_2	$+28 \pm 15$	$+23 \pm 15$	$+23 \pm 15$
D_3	$+20 \pm 15$	$+41 \pm 15$	$+19 \pm 15$
$a_{2,0}^{e}$	$+68 \pm 17$	$+48 \pm 16$	$+46 \pm 16$
$a_{2,0}^{m}$	$+8 \pm 15$	$+5 \pm 15$	$+5 \pm 15$
$a_{2,1}^{e,Re}$	$+17 \pm 18$	$+11 \pm 17$	$+12 \pm 18$
$a_{2,1}^{e,Im}$	-0 ± 19	$+4 \pm 18$	$+3 \pm 18$
$a_{2,1}^{m,Re}$	$+8 \pm 19$	$+4 \pm 18$	$+4 \pm 18$
$a_{2,1}^{m,Im}$	$+3 \pm 19$	$+1 \pm 19$	$+2 \pm 19$
$a_{2,2}^{e,Re}$	$+6 \pm 9$	$+8 \pm 9$	$+8 \pm 9$
$a_{2,2}^{e,Im}$	$+2 \pm 9$	$+0 \pm 8$	$+1 \pm 8$
$a_{2,2}^{m,Re}$	$+0 \pm 9$	$+2 \pm 9$	$+3 \pm 9$
$a_{2,2}^{m,Im}$	-8 ± 9	-12 ± 9	-12 ± 9

Table 5.10: VSH parameters up to degree 2 between Vie18-RayTrace and Gaia-CRF2.

D_3 is increased by about the same amount. However, increasing the D_3 parameter does not necessarily mean that this technique moves the reference frame further from Gaia-CRF2 because, as will be shown later in more detail, the D_3 parameter is rather unstable and can be changed quite significantly by the choices of the analyst. As an example, the Vie18-RayTrace-noAbsGradConst solution is provided in Table 5.10. This is the same solution as before but this time the absolute constraints on tropospheric gradients are removed. It is evident that combining these two analysis choices removed the increase in D_3 while still maintaining the decrease of the $a_{2,0}^{e}$ parameter.

5.2.4 Troposphere estimation parameterization

Mayer *et al.* (2017) indicated that the parameterization of the troposphere estimation can influence the source declination. The wet part of the troposphere is time variable and is not predictable enough to be modeled, therefore, it has to be estimated. In VieVS, this is done using piece wise linear offsets, which are estimated in a certain time interval. Additionally, absolute and relative constraints can be added to stabilize the estimation. It is important to choose the estimation parameterization in accordance to realistic time scales (time intervals) and realistic variability (relative constraints) and range of the estimate (absolute constraints). Usually, best practice values are chosen for these values, as was done for the Vie18 solution. In the following part, the influence of this parameterization on the CRF by varying the intervals and constraints will be investigated.

$[\mu as]$	Vie18	Vie18-ZWD20min	Vie18-Grad1h	Vie18-Grad3h	Vie18-Grad3h-noAbsGradConst
R_1	-46 ± 16	-50 ± 16	-45 ± 16	-45 ± 16	-50 ± 16
R_2	$+60 \pm 15$	$+60 \pm 15$	$+64 \pm 15$	$+61 \pm 15$	$+60 \pm 15$
R_3	-11 ± 14	-9 ± 14	-12 ± 14	-11 ± 14	-9 ± 14
D_1	-1 ± 15	-1 ± 16	-0 ± 16	-1 ± 16	-3 ± 16
D_2	$+28 \pm 15$	$+26 \pm 16$	$+30 \pm 15$	$+29 \pm 15$	$+28 \pm 15$
D_3	$+20 \pm 15$	$+24 \pm 15$	$+37 \pm 15$	$+29 \pm 15$	-2 ± 15
$a_{2,0}^{e}$	$+68 \pm 17$	$+62 \pm 17$	$+70 \pm 17$	$+68 \pm 17$	$+67 \pm 17$
$a_{2,0}^{m}$	$+8 \pm 15$	$+6 \pm 16$	$+7 \pm 16$	$+9 \pm 15$	$+9 \pm 16$
$a_{2,1}^{e,Re}$	$+17 \pm 18$	$+18 \pm 18$	$+19 \pm 18$	$+18 \pm 18$	$+18 \pm 18$
$a_{2,1}^{e,Im}$	-0 ± 19	$+0 \pm 19$	-1 ± 19	-1 ± 19	-1 ± 19
$a_{2,1}^{m,Re}$	$+8 \pm 19$	$+3 \pm 19$	$+7 \pm 19$	$+8 \pm 19$	$+8 \pm 19$
$a_{2,1}^{m,Im}$	$+3 \pm 19$	$+3 \pm 19$	$+3 \pm 19$	$+3 \pm 19$	$+1 \pm 19$
$a_{2,2}^{e,Re}$	$+6 \pm 9$	$+6 \pm 9$	$+6 \pm 9$	$+6 \pm 9$	$+5 \pm 9$
$a_{2,2}^{e,Im}$	$+2 \pm 9$	$+2 \pm 9$	$+2 \pm 9$	$+2 \pm 9$	$+2 \pm 9$
$a_{2,2}^{m,Re}$	$+0 \pm 9$	-2 ± 9	$+0 \pm 9$	-0 ± 9	$+1 \pm 9$
$a_{2,2}^{m,Im}$	-8 ± 9	-7 ± 9	-8 ± 9	-9 ± 9	-8 ± 9

Table 5.11: VSH parameters up to degree 2 between Vie18-ZWD20min and Gaia-CRF2.

5.2.4.1 Estimation interval

The estimation interval is the period at which the troposphere is sampled. Gradients and ZWD are estimated, therefore, the sampling of these two parameters is investigated. In principal, the sampling of the troposphere should be as small as possible. However, the trade-off here is the number of observations versus number of unknowns. The standard values are chosen to represent typical time scales of weather phenomena. Nevertheless, it is important to check these values and see, if more can be gained by reducing the sampling time. In order to do that the sampling of the ZWD was reduced from 30 to 20 min, the solution is called Vie18-ZWD20min. The sampling of the gradients was reduced from 6 h to 3 h, this solution is called Vie18-Grad3h. In solution Vie18-Grad1h the sampling is even further reduced to 1 h. The VSH parameters of these solutions w.r.t. Gaia-CRF2 are listed in Table 5.11.

Reducing the sampling of the ZWD to 20 min does not significantly alter the results. However, when looking at the changed sampling for the gradient estimates it is evident that the glide parameters are increasing when the sampling interval is decreased. The other parameters are not significantly altered by changing the sampling interval of the gradients.

However, when removing the absolute constraints on gradients the gradient estimation interval does not affect the CRF significantly any longer, see solution Vie18-Grad3h-noAbsGradConst in Table 5.11 and compare to Table 5.12.

$[\mu as]$	Vie18	Vie18-noAbsGradConst
R_1	-46 ± 16	-49 ± 16
R_2	$+60 \pm 15$	$+59 \pm 15$
R_3	-11 ± 14	-10 ± 14
D_1	-1 ± 15	-2 ± 16
D_2	$+28 \pm 15$	$+27 \pm 15$
D_3	$+20 \pm 15$	-0 ± 15
$a_{2,0}^{e}$	$+68 \pm 17$	$+68 \pm 17$
$a_{2,0}^{m}$	$+8 \pm 15$	$+8 \pm 15$
$a_{2,1}^{e,Re}$	$+17 \pm 18$	$+17 \pm 18$
$a_{2,1}^{e,Im}$	-0 ± 19	-1 ± 19
$a_{2,1}^{m,Re}$	$+8 \pm 19$	$+7 \pm 19$
$a_{2,1}^{m,Im}$	$+3 \pm 19$	$+2 \pm 19$
$a_{2,2}^{e,Re}$	$+6 \pm 9$	$+6 \pm 9$
$a_{2,2}^{e,Im}$	$+2 \pm 9$	$+2 \pm 9$
$a_{2,2}^{m,Re}$	$+0 \pm 9$	$+1 \pm 9$
$a_{2,2}^{m,Im}$	-8 ± 9	-8 ± 9

Table 5.12: VSH parameters up to degree 2 between Vie18-noAbsGradConst and Gaia-CRF2.

5.2.4.2 Choice of constraints

Putting absolute constraints on gradients effects the declination of sources, see Mayer *et al.* (2017) for more detail. Usually, this is done to avoid unrealistic gradient values. Further, this approach helps to stabilize early VLBI sessions, which tend to have a weak network geometry, see Spicakova *et al.* (2011). However, as shown in Mayer *et al.* (2017) this has a systematic effect on the declination of sources and it is not clear, if this is desirable or not. In Table 5.12 the VSH between the solution without absolute constraints on gradients, which is called Vie18-noAbsGradConst, and Gaia-CRF2 is listed. Compared to Vie18 a significant reduction of the deformation parameter D_3 is evident. This corresponds to a deformation in declination, which is exactly what was published by Mayer *et al.* (2017). This indicates that removing absolute constraints on gradients moves the ICRF closer to the Gaia-CRF2. However, the D_3 parameter is very susceptible to the choices of the analysist. Therefore, this claim has to be thoroughly investigated which is done in a later section.

5.2.5 Clock estimation interval and constraints

In the Vie18 solution, the clocks are estimated every hour with relative constraints of 1.3 cm between estimated offsets. These two parameters were tested by lowering the estimation interval to 30 min (solution Vie18-Clock30min) and loosening the constraints by a factor of ten (Solution vie18-ClockConst13cm). The VSH parameters of these solutions with Gaia-CRF2 are listed in Table 5.13. It is clear the changing the estimation interval as well as loosening

$[\mu as]$	Vie18	Vie18-Clock30min	vie18-ClockConst13cm
R_1	-46 ± 16	-47 ± 16	-45 ± 16
R_2	$+60 \pm 15$	$+61 \pm 15$	$+61 \pm 15$
R_3	-11 ± 14	-11 ± 14	-13 ± 14
D_1	-1 ± 15	-2 ± 16	-5 ± 16
D_2	$+28 \pm 15$	$+28 \pm 15$	$+28 \pm 15$
D_3	$+20 \pm 15$	$+23 \pm 15$	$+21 \pm 15$
$a_{2,0}^{e}$	$+68 \pm 17$	$+69 \pm 17$	$+69 \pm 17$
$a_{2,0}^{m}$	$+8 \pm 15$	$+8 \pm 15$	$+9 \pm 16$
$a_{2,1}^{e,Re}$	$+17 \pm 18$	$+16 \pm 18$	$+14 \pm 18$
$a_{2,1}^{e,Im}$	-0 ± 19	-1 ± 19	-2 ± 19
$a_{2,1}^{m,Re}$	$+8 \pm 19$	$+8 \pm 19$	$+5 \pm 19$
$a_{2,1}^{m,Im}$	$+3 \pm 19$	$+2 \pm 19$	$+1 \pm 19$
$a_{2,2}^{e,Re}$	$+6 \pm 9$	$+7 \pm 9$	$+7 \pm 9$
$a_{2,2}^{e,Im}$	$+2 \pm 9$	$+1 \pm 9$	$+1 \pm 9$
$a_{2,2}^{m,Re}$	$+0 \pm 9$	$+0 \pm 9$	$+1 \pm 9$
$a_{2,2}^{m,Im}$	-8 ± 9	-8 ± 9	-8 ± 9

Table 5.13: VSH parameters up to degree 2 between Vie18-Clock30min and Gaia-CRF2.

the relative constraints does not have a significant effect on the deformation or rotation of the celestial reference frame. This illustrates that the choices for estimation interval and constraint are sufficient to describe the VLBI clocks.

5.2.6   Phase calibration at station Hobart12

Mayer *et al.* (2017) showed that the phase calibration at the Australian stations Hobart12 and Kath12m influences the declination of sources. Phase calibration is a technique where tones with a known frequency and phase are injected at the receiver. This can later be used to extract the effect the measuring equipment has on the signal.

The session AUG030 was analyzed once with phase calibration turned on and once with phase calibration turned off (manual phase calibration was used). When comparing the two results on the delay level a systematic effect mostly in azimuth becomes visible, see Figure 5.17 where this phenomenon is depicted for station Hobart12. This effect is mainly azimuth dependent with no clear systematic in elevation visible. One possible reason for this effect is cable stretching. Some VLBI stations have what is called a cable calibration unit. This measures the stretching of cables by sending a signal to the receiver and back to the cable calibration unit. The important thing here is that the signal travels up to the receiver and down again and, therefore, both directions are calibrated. However, the Australian stations do not have such a unit but rather use the phase calibration to account for this effect. The problem here is that the signal used for the phase calibration has to travel to the receiver end without oversight. Therefore, stretching that occurs on the way up to the receiver is not
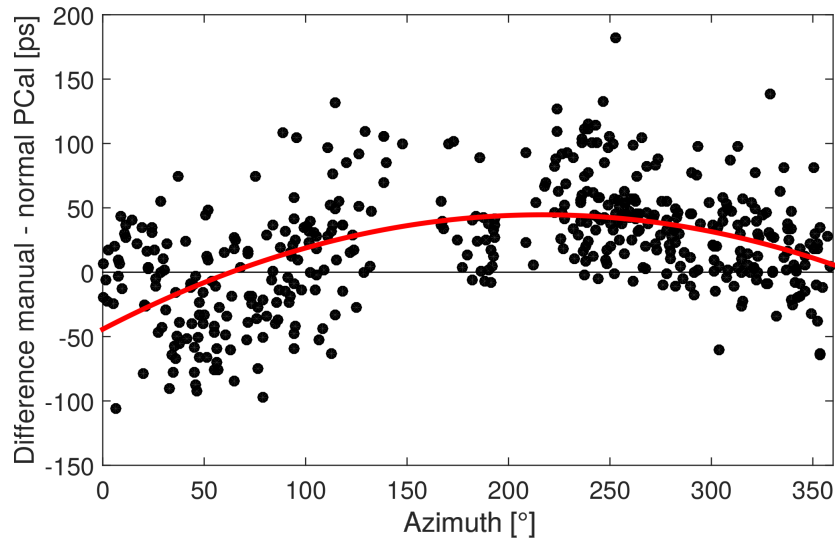
accounted for.

Figure 5.17: Difference in group delay for the station Hobart12 when session AUG030 is once analyzed using the phase calibration tones and once analyzed using manual phase calibration. The residual delays are plotted over azimuth and a quadratic polynomial is fitted to the scatter.

The fact that stretching is probably the reason for this behavior becomes clearer when the effect is split up into the different cable wraps. A VLBI station usually has some overlapping azimuth areas in order to give it more flexibility when slewing. Consequently, some part of the azimuth range of a station is ambiguous. This is called cable wrap. In order to remove this ambiguity it is usually split up in a clockwise, neutral and counter clockwise part. The information about the cable wrap of the station can be found in the schedule of the session. Using this information it is possible to solve the ambiguity still present in Figure 5.17 and see the real systematic effect. Figure 5.18 depicts just that with the counter clockwise depicted on the left, the neutral part in the middle and the clockwise part of the systematic effect depicted on the right. One can clearly see that the color changes when the edges of the cable wrap are reached. The edge of the cable wrap is also the area, which experiences the most stretching.

The obvious solution for this problem would be to develop a model and correct the observations. Unfortunately, the cable wrap information is not saved during the analysis and the cable wrap written into the schedule file does not always correspond to the real observed cable wrap. Therefore, it is not possible to create a model based on Figure 5.18. However, a model based on Figure 5.17 can be created and used in the analysis. The downside is that the ambiguity of the cable wrap cannot be accounted for which means that this model can only be used for test purposes.

In order to see, if this effect can influence the coordinates of sources a solution, where a fitted model (red line in Figure 5.17) was used to add a residual delay dependent on azimuth to all observations of the station Hobart12, was created. The model used here is very simple;
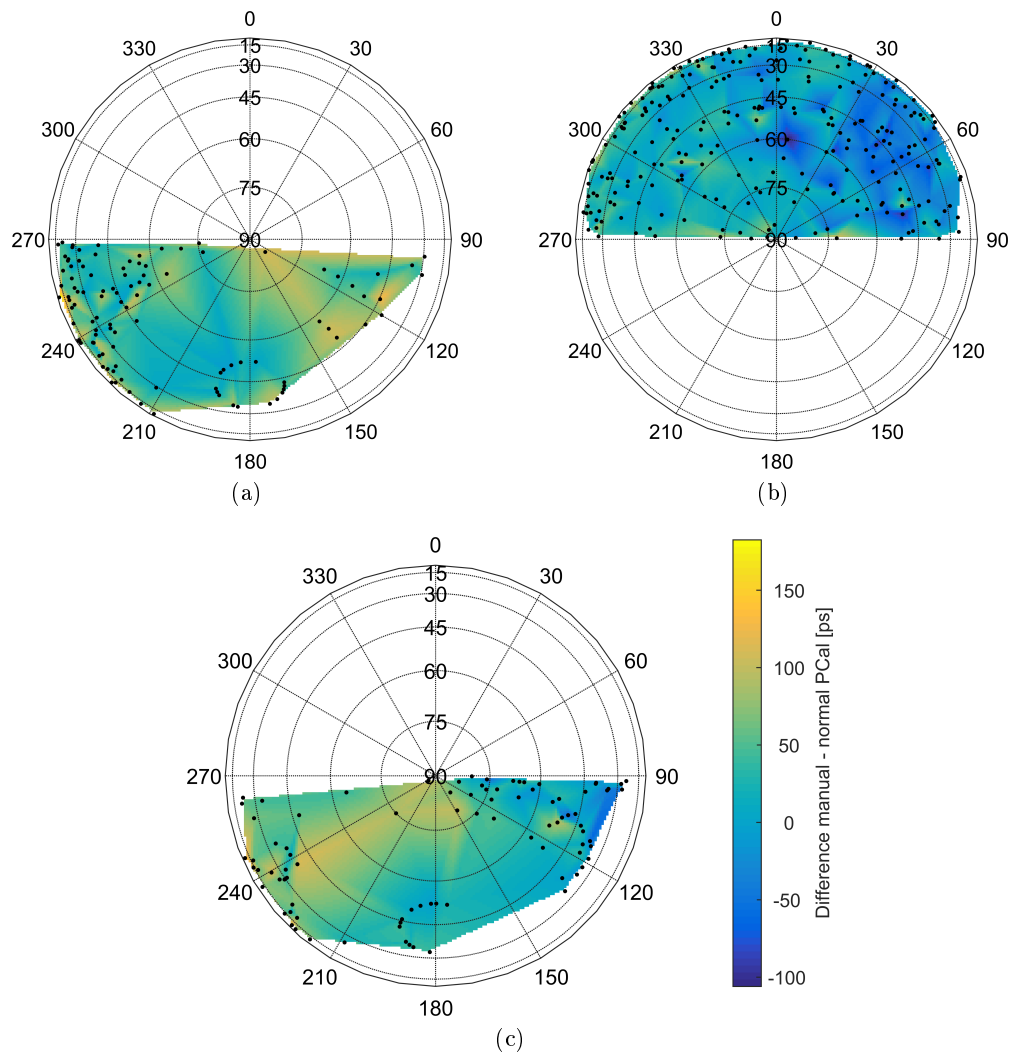
Figure 5.18: Same effect that is plotted in Figure 5.17 but this time plotted over azimuth and elevation. Further, the cable wrap information was used to split the systematic effect into the counter clockwise (upper left), neutral (upper right) and clockwise (lower middle) part.

basically, a polynomial function of order two was fitted to Figure 5.17. Figure 5.19 depicts the declination difference of this solution with the standard solution. One can clearly see that the phase calibration at Hobart12 significantly influences the declination of sources. This indicates that a station dependent effect such as this phase calibration problem can influence the declination of sources in a way similar to the declination bias. It is somehow counterintuitive that an azimuth dependent effect influences the declination of sources. However, considering the unique location of these telescopes this makes sense. Sources, which have small negative declinations, are only visible in the north of these stations. Moreover, north is also where the zero point of the azimuth axis of the Australian telescopes lies. Therefore, these sources are only observed with small azimuths. Sources with higher negative elevations are observed with more ranges of azimuth effectively letting an azimuth dependent station effect propagate into the declination of sources.
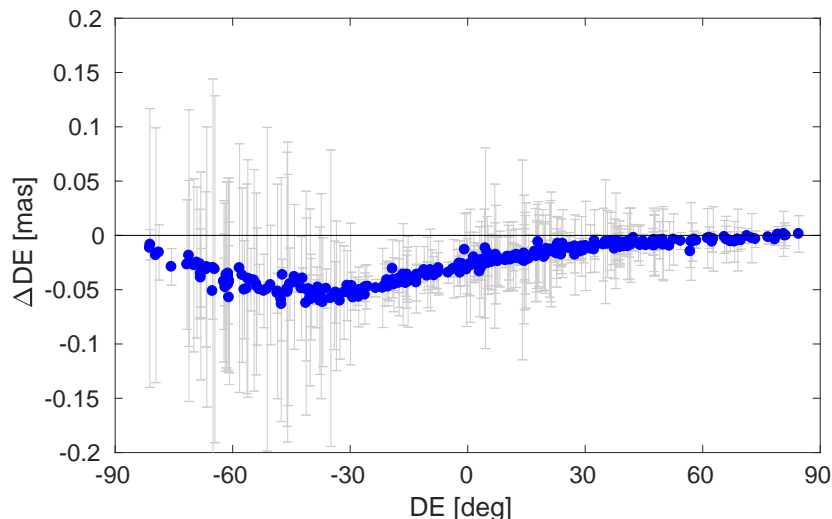

Figure 5.19: Difference of declination of defining sources of a solution were the simple phase cal model was used vs. the standard solution.

After proving that this effect can propagate into the CRF a solution was made where the polynomial model described above was used only for sessions where Hobart12 observed and the phase calibration tones were used. Again, this solution is only for testing purposes because of the reasons described above. Table 5.14 lists the VSH parameters between this solution (Vie18-PCalHb) and Gaia-CRF2. On the one hand, an increase in the D_3 parameter can be observed when using this simple model but, on the other hand, a decrease of the $a_{2,0}^e$ parameter is observed as well. The interaction of this effect with other analysis choices will be discussed in a later section.

5.2.7 No-Net-Rotation constraints

In this section the strength of no-net-rotation constraints are tested. Further, the selection of sources, which are used for these constraints, and the impact of that on the frame orientation

$[\mu as]$	Vie18	Vie18-PCalHb
R_1	-46 ± 16	-47 ± 16
R_2	$+60 \pm 15$	$+60 \pm 15$
R_3	-11 ± 14	-7 ± 14
D_1	-1 ± 15	-0 ± 15
D_2	$+28 \pm 15$	$+29 \pm 15$
D_3	$+20 \pm 15$	$+37 \pm 15$
$a_{2,0}^{e}$	$+68 \pm 17$	$+58 \pm 17$
$a_{2,0}^{m}$	$+8 \pm 15$	$+5 \pm 15$
$a_{2,1}^{e,Re}$	$+17 \pm 18$	$+16 \pm 18$
$a_{2,1}^{e,Im}$	-0 ± 19	-1 ± 19
$a_{2,1}^{m,Re}$	$+8 \pm 19$	$+9 \pm 19$
$a_{2,1}^{m,Im}$	$+3 \pm 19$	$+4 \pm 19$
$a_{2,2}^{e,Re}$	$+6 \pm 9$	$+6 \pm 9$
$a_{2,2}^{e,Im}$	$+2 \pm 9$	$+1 \pm 9$
$a_{2,2}^{m,Re}$	$+0 \pm 9$	$+0 \pm 9$
$a_{2,2}^{m,Im}$	-8 ± 9	-8 ± 9

Table 5.14: VSH parameters up to degree 2 between Vie18-PCalHb and Gaia-CRF2.

is investigated.

5.2.7.1 Strength of constraints

The no-net-rotation ensures that the frame is non-rotating w.r.t. a selected number of sources. This is done by choosing a subset of sources, which are called the defining sources and adding constraints that reduce the combined rotation of these sources to zero. In VieVS, these constraints are added as extra columns and lines to the normal equation system. This effectively adds constraints with infinite weight. Another possibility would be to create a constraint matrix, which is then added to the normal equation system. With this option, it is possible to weigh the constraints however desirable. The influence of these weights was tested by creating three solutions. The no-net-rotation was loosened more and more with weights of 20 µas, 100 µas and 1000 µas. These solutions are called Vie18-NNR20muas, Vie18-NNR100muas and Vie18-NNR1000muas respectively. The impact on the VSH between these solutions and Gaia-CRF2 can be neglected, with the largest difference being present for the Vie18-NNR1000muas. However, even the VSH parameters of this solution do not deviate by more than 1 µas from the reference solution. This indicates that no external strains are affecting the no-net-rotation, which means that even a very loose weight is satisfactory.

5.2.7.2 Choice of defining sources

In order to test the stability of the rotation the set of 295 defining sources was halved into 148 and 147 and the NNR was calculated using these subsets. A global distribution of these subsets was considered in order to avoid effects due to inhomogeneous distributions, see Figure 5.20 where the two subsets are plotted. In Table 5.15 the VSH parameters of these two solutions are listed. It is evident that the rotational parameters change significantly and are very susceptible to the set of defining sources used.
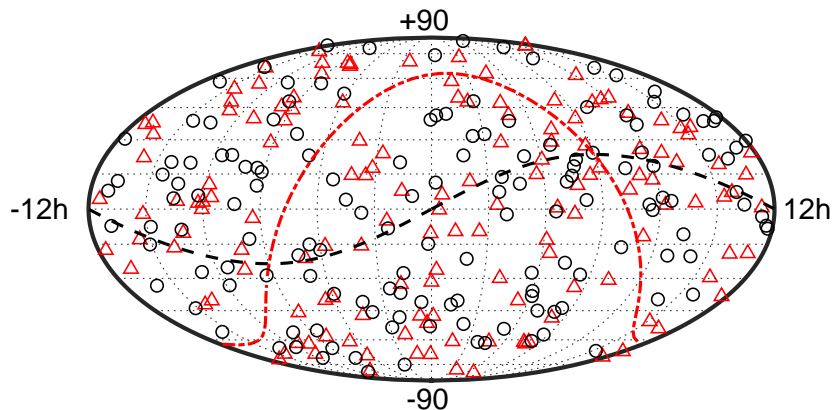
Figure 5.20: Depicted is the distribution of the defining sources. Each half (red triangles and black circles) of the defining sources was used once for the NNR. The galactic plane is depicted in red with the center of the Galaxy denoted as a black circle. The ecliptic is depicted as a black dashed line.
.

During the creation of ICRF3, the ICRF2 defining sources were investigated and 36 sources with a structure index larger than three were found[1]. In order to test the impact of the structure of these sources on the rotation of the frame these 36 sources were separated into four lists:

- Sources with SI larger than 4. One source falls into this category.

- Sources with SI larger than 3.5. 7 sources fall into this category.

- Sources with SI larger than 3.25. 12 sources fall into this category.

- Sources with SI larger than 3.0. 36 sources fall into this category.

For each category a solution was created removing the respective list from the defining sources. The resulting solutions are called Vie18-SI>4.0, Vie18-SI>3.5, Vie18-SI>3.25 and Vie18-SI>3.0 and their VSH parameters with respect to Gaia-CRF2 are listed in Table 5.16. No significant change in rotation was found for the first three solutions. However, the fourth solution, where most sources are excluded, shows a significantly different rotation in R_2. Nevertheless, since no direct dependency on the SI is found one has to conclude that large SI do not affect the rotation of the frame.

---

[1]Personal communication Patrick Charlot

$[\mu as]$	Vie18	Vie18-NNRHalfFirst	Vie18-NNRHalfSecond
R_1	-46 ± 16	-25 ± 16	-61 ± 16
R_2	$+60 \pm 15$	$+38 \pm 15$	$+87 \pm 15$
R_3	-11 ± 14	-27 ± 14	$+1 \pm 14$
D_1	-1 ± 15	-1 ± 16	-1 ± 15
D_2	$+28 \pm 15$	$+28 \pm 15$	$+28 \pm 15$
D_3	$+20 \pm 15$	$+20 \pm 15$	$+20 \pm 15$
$a_{2,0}^{e}$	$+68 \pm 17$	$+69 \pm 17$	$+69 \pm 17$
$a_{2,0}^{m}$	$+8 \pm 15$	$+8 \pm 15$	$+8 \pm 15$
$a_{2,1}^{e,Re}$	$+17 \pm 18$	$+16 \pm 18$	$+16 \pm 18$
$a_{2,1}^{e,Im}$	-0 ± 19	-0 ± 19	-0 ± 19
$a_{2,1}^{m,Re}$	$+8 \pm 19$	$+8 \pm 19$	$+8 \pm 19$
$a_{2,1}^{m,Im}$	$+3 \pm 19$	$+3 \pm 19$	$+3 \pm 19$
$a_{2,2}^{e,Re}$	$+6 \pm 9$	$+6 \pm 9$	$+6 \pm 9$
$a_{2,2}^{e,Im}$	$+2 \pm 9$	$+2 \pm 9$	$+2 \pm 9$
$a_{2,2}^{m,Re}$	$+0 \pm 9$	$+1 \pm 9$	$+0 \pm 9$
$a_{2,2}^{m,Im}$	-8 ± 9	-8 ± 9	-8 ± 9

Table 5.15: VSH parameters up to degree 2 between Vie18-NNRHalfFirst/Vie18-NNRHalfSecond and Gaia-CRF2.

During the creation of the ICRF3, a new set of defining sources was chosen. Special focus was given to the distribution of the sources. However, since the Southern Hemisphere lacks sources compared to the north some regions could not be filled or only be filled with sources, which are not of the highest positional stability. Nevertheless, special care (stable position time series; SI as low as possible) was taken to take the best source possible in the region. In total 303 sources are defining the ICRF3. When these sources are used in the Vienna solution the VSH parameters listed in Table 5.17 are found. Some of the new defining sources have bad a priori values because they were only observed recently. Therefore, in order to provide the best a priori values available the ICRF3sx solution was chosen as a priori catalog. One can see that even though only 165 sources are the same defining sources used in ICRF2 the rotation is very similar to Vie18 with the largest difference being about 10 µas in R_1. This demonstrates the high stability of the frame axis, when a sufficient number of defining sources with a sufficient distribution is selected. However, the large differences presented in Table 5.15 demonstrate how unstable the frame can get without a sufficient number of defining sources. When looking at Table 5.15, 5.16 and 5.17 it becomes evident that no matter what list of sources is used for the orientation of the frame the deformational parameters are unaffected. This indicates that the VSH decomposition correctly separates rotation from deformation.

$[\mu as]$	Vie18	Vie18-SI>4.0	Vie18-SI>3.5	Vie18-SI>3.25	Vie18-SI>3.0
R_1	-46 ± 16	-47 ± 16	-48 ± 16	-47 ± 16	-43 ± 16
R_2	$+60 \pm 15$	$+60 \pm 15$	$+59 \pm 15$	$+60 \pm 15$	$+83 \pm 15$
R_3	-11 ± 14	-8 ± 14	-8 ± 14	-7 ± 14	-12 ± 14
D_1	-1 ± 15	-1 ± 15	-1 ± 15	-1 ± 15	-1 ± 15
D_2	$+28 \pm 15$	$+28 \pm 15$	$+28 \pm 15$	$+28 \pm 15$	$+28 \pm 15$
D_3	$+20 \pm 15$	$+20 \pm 15$	$+20 \pm 15$	$+20 \pm 15$	$+20 \pm 15$
$a_{2,0}^{e}$	$+68 \pm 17$	$+69 \pm 17$	$+69 \pm 17$	$+69 \pm 17$	$+69 \pm 17$
$a_{2,0}^{m}$	$+8 \pm 15$	$+8 \pm 15$	$+8 \pm 15$	$+8 \pm 15$	$+8 \pm 15$
$a_{2,1}^{e,Re}$	$+17 \pm 18$	$+16 \pm 18$	$+16 \pm 18$	$+16 \pm 18$	$+16 \pm 18$
$a_{2,1}^{e,Im}$	-0 ± 19	-0 ± 19	-0 ± 19	-0 ± 19	-0 ± 19
$a_{2,1}^{m,Re}$	$+8 \pm 19$	$+8 \pm 19$	$+8 \pm 19$	$+8 \pm 19$	$+8 \pm 19$
$a_{2,1}^{m,Im}$	$+3 \pm 19$	$+3 \pm 19$	$+3 \pm 19$	$+3 \pm 19$	$+3 \pm 19$
$a_{2,2}^{e,Re}$	$+6 \pm 9$	$+6 \pm 9$	$+6 \pm 9$	$+6 \pm 9$	$+6 \pm 9$
$a_{2,2}^{e,Im}$	$+2 \pm 9$	$+2 \pm 9$	$+2 \pm 9$	$+2 \pm 9$	$+2 \pm 9$
$a_{2,2}^{m,Re}$	$+0 \pm 9$	$+1 \pm 9$	$+1 \pm 9$	$+1 \pm 9$	$+1 \pm 9$
$a_{2,2}^{m,Im}$	-8 ± 9	-8 ± 9	-8 ± 9	-8 ± 9	-8 ± 9

Table 5.16: VSH parameters up to degree 2 between solutions with different structure index cutoffs for defining sources and Gaia-CRF2.

5.2.8   Elevation weighting

Geodetic VLBI experiments usually try to observe in many different elevations, with the lowest at 5 degrees (usual threshold for geodetic VLBI). This is done to decorrelate the stations height, stations clock and the ZWD. However, when observing at such low elevations the signal from space has to travel through much more of the troposphere, which magnifies its impact. Down-weighting these observations is an effective measure to tell the least squares adjustment that these low elevation observations are noisier then the high elevation scan. Usually VieVS simply adds 1 cm of noise to the formal errors from the correlator output.[1]   However, it is possible to change this by adding noise to the observations dependent on their elevations. This is called elevation dependent weighting and is realized by:

$$addednoise = \sqrt{(\frac{6}{sin(e_1)})^2 + (\frac{6}{sin(e_2)})^2}, \tag{5.1}$$

where e_1 and e_2 are the elevations of the two antennas observing. The numerator in this equation represents the level of added noise in picoseconds. In VieVS, the default added noise is six picoseconds. Using elevation dependent weighting does influence the VSH significantly, see Table 5.18. In particular, the D_3 parameter which corresponds to a deformation in dec-

---

[1]Noise has to be added since the formal errors reported by the correlator are usually too optimistic. 1 cm is a value chosen based on experience.

$[\mu as]$	Vie18	Vie18-ICRF3defining-ICRF3apriori
R_1	-46 ± 16	-37 ± 16
R_2	$+60 \pm 15$	$+58 \pm 15$
R_3	-11 ± 14	-8 ± 14
D_1	-1 ± 15	-1 ± 16
D_2	$+28 \pm 15$	$+28 \pm 15$
D_3	$+20 \pm 15$	$+20 \pm 15$
$a_{2,0}^{e}$	$+68 \pm 17$	$+69 \pm 17$
$a_{2,0}^{m}$	$+8 \pm 15$	$+8 \pm 16$
$a_{2,1}^{e,Re}$	$+17 \pm 18$	$+14 \pm 18$
$a_{2,1}^{e,Im}$	-0 ± 19	$+2 \pm 19$
$a_{2,1}^{m,Re}$	$+8 \pm 19$	$+8 \pm 19$
$a_{2,1}^{m,Im}$	$+3 \pm 19$	$+2 \pm 19$
$a_{2,2}^{e,Re}$	$+6 \pm 9$	$+6 \pm 9$
$a_{2,2}^{e,Im}$	$+2 \pm 9$	$+1 \pm 9$
$a_{2,2}^{m,Re}$	$+0 \pm 9$	$+1 \pm 9$
$a_{2,2}^{m,Im}$	-8 ± 9	-8 ± 9

Table 5.17: VSH parameters up to degree 2 between solution Vie18-ICRF3defining-ICRF3Apriori and Gaia-CRF2.

lination is reduced. However, when looking at the χ^2/ndf factor of the solution where six picoseconds noise were added (Vie18-ElWeight6ps) a significant increase (the new factor is 1.7) can be observed. This indicates that the added noise of six picoseconds might be too optimistic and a larger value should be used. The noise was doubled to 12 picoseconds and a new solution was created, see solution Vie18-ElWeight12ps in Table 5.18. The χ^2/ndf factor of this solution is 1.0. One can see a larger reduction in the D_2 and $a_{2,0}^{e}$ parameter when more elevation dependent noise is used. However, adding more noise also increases the error bars of the VSH parameters.

5.2.9   Special handling sources

In the creation of the ICRF2, 39 sources were identified as special handling sources. The idea behind this selection was that the most unstable sources, which experience significant movement, should be calculated per session effectively allowing them to deviate from a point source. However, the downside of this approach is that the position of these sources, which are some of the most observed strong radio sources, is only available as a time series and not as a single position. The workaround for this problem is to calculate a single position and WRMS from these time series, which was done for ICRF2. In this section, the influence of these special handling sources on the CRF is investigated. This is done by including all special handling sources into the solution as global parameters (solution Vie18-NoSpecialHandling)

$[\mu as]$	Vie18	Vie18-ElWeight6ps	Vie18-ElWeight12ps
R_1	-46 ± 16	-55 ± 16	-55 ± 16
R_2	$+60 \pm 15$	$+60 \pm 15$	$+58 \pm 16$
R_3	-11 ± 14	-9 ± 14	-8 ± 14
D_1	-1 ± 15	-9 ± 15	-4 ± 16
D_2	$+28 \pm 15$	$+23 \pm 15$	$+16 \pm 16$
D_3	$+20 \pm 15$	$+4 \pm 15$	$+8 \pm 15$
$a_{2,0}^{e}$	$+68 \pm 17$	$+66 \pm 16$	$+61 \pm 17$
$a_{2,0}^{m}$	$+8 \pm 15$	$+10 \pm 15$	$+10 \pm 16$
$a_{2,1}^{e,Re}$	$+17 \pm 18$	$+11 \pm 17$	$+12 \pm 18$
$a_{2,1}^{e,Im}$	-0 ± 19	$+4 \pm 18$	$+1 \pm 19$
$a_{2,1}^{m,Re}$	$+8 \pm 19$	$+4 \pm 19$	$+3 \pm 19$
$a_{2,1}^{m,Im}$	$+3 \pm 19$	$+0 \pm 19$	-4 ± 19
$a_{2,2}^{e,Re}$	$+6 \pm 9$	$+6 \pm 9$	$+9 \pm 9$
$a_{2,2}^{e,Im}$	$+2 \pm 9$	-2 ± 8	-0 ± 9
$a_{2,2}^{m,Re}$	$+0 \pm 9$	-1 ± 9	-2 ± 9
$a_{2,2}^{m,Im}$	-8 ± 9	-14 ± 9	-11 ± 9

Table 5.18: VSH parameters up to degree 2 between Vie18-ElWeight6ps/Vie18-ElWeight12ps and Gaia-CRF2.

and investigating the impact on the VSH when compared to Gaia-CRF2. A second intermediate solution was created were only the ten most unstable sources[1] are removed from the global solution, it is called Vie18-10SepcialHandling. The VSH parameters of both solutions are listed in Table 5.19. Including the special handling sources into the solution as global parameters does not significantly deform the frame. However, small systematic deformations of about a couple of μas are present. This indicates that even though these sources experience a significant non point-like behavior estimating them alongside other source positions does not deform the reference frame significantly. Since estimating these sources in a global adjustment provides better estimates of their positions the solution without special sources, Vie18-NoSpecialHandling, should be preferred.

5.2.10 Station seasonal harmonics

Krásná *et al.* (2015) showed that seasonal station displacements could affect the position of sources with a sparse observing history. Further, they showed that no systematic effect propagates from these displacements into the CRF. Since this study was conducted, the southern Australian stations started to observe and, consequently, the declination bias appeared. In order to check, if a seasonal deformation of these stations somehow affected the sparsely observed southern sources, a solution was generated. In this solution annual and semiannual

---

[1]Personal communication David Gordon

$[\mu as]$	Vie18	Vie18-NoSpecialHandling	Vie18-10SpecialHandling
R_1	-46 ± 16	-46 ± 16	-45 ± 16
R_2	$+60 \pm 15$	$+64 \pm 15$	$+62 \pm 15$
R_3	-11 ± 14	-13 ± 14	-12 ± 14
D_1	-1 ± 15	-3 ± 15	-2 ± 15
D_2	$+28 \pm 15$	$+31 \pm 15$	$+30 \pm 15$
D_3	$+20 \pm 15$	$+20 \pm 15$	$+20 \pm 15$
$a_{2,0}^{e}$	$+68 \pm 17$	$+72 \pm 17$	$+70 \pm 17$
$a_{2,0}^{m}$	$+8 \pm 15$	$+10 \pm 15$	$+8 \pm 15$
$a_{2,1}^{e,Re}$	$+17 \pm 18$	$+15 \pm 18$	$+15 \pm 18$
$a_{2,1}^{e,Im}$	-0 ± 19	$+1 \pm 19$	$+1 \pm 19$
$a_{2,1}^{m,Re}$	$+8 \pm 19$	$+7 \pm 19$	$+7 \pm 19$
$a_{2,1}^{m,Im}$	$+3 \pm 19$	$+3 \pm 19$	$+3 \pm 19$
$a_{2,2}^{e,Re}$	$+6 \pm 9$	$+6 \pm 9$	$+6 \pm 9$
$a_{2,2}^{e,Im}$	$+2 \pm 9$	$+1 \pm 9$	$+1 \pm 9$
$a_{2,2}^{m,Re}$	$+0 \pm 9$	-0 ± 9	$+0 \pm 9$
$a_{2,2}^{m,Im}$	-8 ± 9	-8 ± 9	-8 ± 9

Table 5.19: VSH parameters up to degree 2 between Vie18-NoSpecialHandling and Gaia-CRF2.

periods for north, east and up components of the southern stations were estimated, it is called Vie18-StatSesHarm. Table 5.20 lists the VSH parameters of this solution w.r.t. Gaia-CRF2. When comparing these parameters to the reference solution Vie18 it is evident that the effect of station seasonal harmonic displacements does not affect the CRF significantly. This confirms the conclusion by Krásná *et al.* (2015) that station seasonal harmonic displacements do not systematically deform the CRF.

5.2.11 Estimation of galactic aberration

The GA can be estimated from VLBI data, see Section 3.3.4 for more details on the estimation process. When estimating GA one has to decide, if the whole vector should be estimated, containing the information about the amplitude and the direction (Galactic Center) of the GA, or only the amplitude should be estimated, effectively fixing the Galactic Center to the known coordinates. The advantage of estimating the whole vector is that the coordinates of the estimated Galactic Center can be used as quality criteria since the real coordinates of the Galactic Center are well known. Conversely, this knowledge can be used to fix the Galactic Center to the given coordinates, adding a priori information to the estimation process. Since the estimated position of the Galactic Center is deemed important information, it was decided to estimate the whole GA vector. In Table 5.21 the estimated amplitude and position of the GA vector is provided. When GA is corrected from the data set the D_2 and D_3 parameters of the VSH are significantly influenced, see Section 5.2.12. Other analysis strategies such as the interval of gradient estimations, the absolute constraints on gradients and the elevation

$[\mu as]$	Vie18	Vie18-StatSesHarm
R_1	-46 ± 16	-47 ± 16
R_2	$+60 \pm 15$	$+60 \pm 15$
R_3	-11 ± 14	-11 ± 14
D_1	-1 ± 15	-1 ± 15
D_2	$+28 \pm 15$	$+27 \pm 15$
D_3	$+20 \pm 15$	$+21 \pm 15$
$a_{2,0}^{e}$	$+68 \pm 17$	$+69 \pm 17$
$a_{2,0}^{m}$	$+8 \pm 15$	$+7 \pm 15$
$a_{2,1}^{e,Re}$	$+17 \pm 18$	$+16 \pm 18$
$a_{2,1}^{e,Im}$	-0 ± 19	$+0 \pm 19$
$a_{2,1}^{m,Re}$	$+8 \pm 19$	$+8 \pm 19$
$a_{2,1}^{m,Im}$	$+3 \pm 19$	$+3 \pm 19$
$a_{2,2}^{e,Re}$	$+6 \pm 9$	$+6 \pm 9$
$a_{2,2}^{e,Im}$	$+2 \pm 9$	$+2 \pm 9$
$a_{2,2}^{m,Re}$	$+0 \pm 9$	$+0 \pm 9$
$a_{2,2}^{m,Im}$	-8 ± 9	-7 ± 9

Table 5.20: VSH parameters up to degree 2 between Vie18-StatSesHarm and Gaia-CRF2.

	Amplitude $[\mu as/year]$	RA [deg]	DEC [deg]
Vie18-estGA	7.0 ± 0.2	264 ± 2	-26 ± 3
Vie18-estGA-noAbsGradConst	6.5 ± 0.2	264 ± 2	-15 ± 3
Vie18-estGA-elWeight6ps	6.6 ± 0.2	269 ± 2	-24 ± 3
Vie18-estGA-elWeight12ps	6.6 ± 0.2	266 ± 2	-24 ± 3
Vie18-estGA-Grad1h	7.1 ± 0.2	264 ± 2	-29 ± 3
Vie18-estGA-Grad3h	7.1 ± 0.2	264 ± 2	-27 ± 3
Vie18-estGA-RayTrace	7.4 ± 0.2	264 ± 2	-35 ± 3

Table 5.21: GA estimates from different solutions.

weighting scheme influence the D_3 parameter as well, see Sections 5.2.8, 5.2.4.2 and 5.2.4.1. Since some estimation techniques influence the same parameters as GA their influence on the estimation of GA was tested. In Table 5.21 the estimated GA with different analysis strategies are listed.

The GA can be corrected by simply estimating it alongside the other parameters. Therefore, a similar reduction in D_2 and D_3 as seen when GA is corrected a priori (see Section 5.2.12) should be seen when GA is estimated. In Table 5.22 the VSH parameters of the different solutions where GA was estimated are listed. Similar to correcting GA a priori the D_2 and D_3 parameters are reduced significantly.

If the GA is estimated from the Vie18 data set an amplitude of about 7 $\mu as/year$ is found. This is rather large when compared to estimates from other authors, see Table 5.23.

[μas]	Viel8	Viel8-estGA	Viel8-estGA-noAbsGradConst	Viel8-estGA-elWeigt6ps	Viel8-estGA-elWeigt12ps	Viel8-estGA-Grad1h	Viel8-estGA-Grad3h	Viel8-estGA-RayTrace
R_1	-46 ± 16	-39 ± 16	-42 ± 16	-48 ± 16	-45 ± 16	-38 ± 16	-38 ± 16	-43 ± 16
R_2	$+60\pm15$	$+57\pm15$	$+56\pm15$	$+57\pm15$	$+60\pm16$	$+60\pm15$	$+58\pm15$	$+57\pm15$
R_3	-11 ± 14	-8 ± 14	-7 ± 14	-6 ± 14	-9 ± 14	-9 ± 14	-8 ± 14	-4 ± 14
D_1	-1 ± 15	-6 ± 15	-7 ± 16	-10 ± 15	-9 ± 16	-4 ± 16	-5 ± 16	-4 ± 15
D_2	$+28\pm15$	-9 ± 15	-9 ± 15	-13 ± 15	-12 ± 16	-8 ± 15	-8 ± 15	-12 ± 15
D_3	$+20\pm15$	$+5\pm15$	-11 ± 15	-11 ± 15	$+2\pm15$	$+17\pm15$	$+10\pm15$	$+20\pm15$
$a_{2,0}^{e}$	$+68\pm17$	$+66\pm17$	$+67\pm17$	$+62\pm16$	$+62\pm17$	$+67\pm17$	$+65\pm17$	$+43\pm16$
$a_{2,0}^{m}$	$+8\pm15$	$+8\pm15$	$+8\pm15$	$+10\pm15$	$+12\pm16$	$+7\pm16$	$+9\pm15$	$+5\pm15$
$a_{2,1}^{e,Re}$	$+17\pm18$	$+16\pm18$	$+17\pm18$	$+11\pm17$	$+14\pm18$	$+18\pm18$	$+18\pm18$	$+11\pm17$
$a_{2,1}^{e,Im}$	-0 ± 19	-2 ± 19	-2 ± 19	$+2\pm18$	$+0\pm19$	-2 ± 19	-3 ± 19	$+3\pm18$
$a_{2,1}^{m,Re}$	$+8\pm19$	$+9\pm19$	$+9\pm19$	$+5\pm19$	$+6\pm19$	$+8\pm19$	$+9\pm19$	$+6\pm18$
$a_{2,1}^{m,Im}$	$+3\pm19$	$+3\pm19$	$+2\pm19$	$+0\pm19$	$+3\pm19$	$+3\pm19$	$+3\pm19$	$+1\pm19$
$a_{2,2}^{e,Re}$	$+6\pm9$	$+6\pm9$	$+6\pm9$	$+6\pm9$	$+7\pm9$	$+6\pm9$	$+6\pm9$	$+8\pm9$
$a_{2,2}^{e,Im}$	$+2\pm9$	$+1\pm9$	$+2\pm9$	-2 ± 8	-1 ± 9	$+2\pm9$	$+2\pm9$	$+0\pm8$
$a_{2,2}^{m,Re}$	$+0\pm9$	$+1\pm9$	$+1\pm9$	-0 ± 9	-1 ± 9	$+1\pm9$	$+0\pm9$	$+3\pm9$
$a_{2,2}^{m,Im}$	-8 ± 9	-8 ± 9	-7 ± 9	-13 ± 9	-12 ± 9	-8 ± 9	-8 ± 9	-12 ± 9

Table 5.22: VSH parameters up to degree 2 between different solutions where GA was estimated and Gaia-CRF2.

	Amplitude [$\mu as/year$]	RA [deg]	DEC [deg]
Titov *et al.* (2011)	6.4 ± 1.5	263 ± 11	-20 ± 12
Xu *et al.* (2012)	5.8 ± 0.4	243 ± 4	-11 ± 4
Titov & Lambert (2013)	6.4 ± 1.1	266 ± 7	-26 ± 7
MacMillan (2014)	5.6 ± 0.4	267 ± 3	-11 ± 3
Titov & Lambert (2016)	5.9 ± 1.0	273 ± 13	-56 ± 9
Krásná & Titov (2017)	5.4 ± 0.4	273 ± 4	-27 ± 4
Titov & Krásná (2018)	5.2 ± 0.2	281 ± 3	-35 ± 3

Table 5.23: GA estimates from different authors.

	Amplitude [$\mu as/year$]	RA [deg]	DEC [deg]
$1979.7 - 2016.5 \sim 5800$ sessions	6.1 ± 0.2	260 ± 2	-18 ± 4
$1993.0 - 2016.5 \sim 2000$ sessions	5.4 ± 0.4	273 ± 4	-27 ± 4

Table 5.24: GA estimates from different data sets. This table is copied from Krásná & Titov (2017).

However, Krásná & Titov (2017) showed that using a large data set including sessions with weak networks yields a higher value for GA, see Table 5.24. In the solution with fewer sessions (about 2000), they only used sessions with large networks. Applying this knowledge, the large amplitude (about 7 $\mu as/year$), which is derived from the data set that includes almost all VLBI sessions (including small networks) can be explained. Further, Krásná & Titov (2017) did not use absolute constraints on tropospheric gradients which reduces the GA estimate a little further, see Table 5.21. When looking at Table 5.21 it is evident that the estimate of GA is to a certain extent dependent on the parameterization of the solution.

5.2.12 Correction of galactic aberration

MacMillan (2014) and Krásná & Titov (2017) investigated the impact of GA correction on the celestial reference frames. This section will deal with the same aim but will use an independent catalog, the Gaia-CRF2, and a more refined method, the VSH, to describe the influence of GA correction on the frame.

In order to stay consistent with the data and software the logical thing to do would be to use the value reported in Section 5.2.11 to correct for GA in this solution. However, this would make comparisons to solutions from other analysts complicated because everybody would correct something different. Therefore, the IVS established a working group with the general purpose of investigating the issues concerning the incorporation of the GA in IVS analysis[1]. This working group settled on 5.6 $\mu as/year$ (personal communication MacMillan) for the amplitude. Further, the center of the Galaxy is set to the known position of $17h45min40sec$ in right ascension and $-29^o00'28''$ in declination. However, the value 5.6 $\mu as/year$, which

---

[1] https://ivscc.gsfc.nasa.gov/about/wg/wg8/index.html

$[\mu as]$	Vie18	Vie18-GA2015
R_1	-46 ± 16	-41 ± 16
R_2	$+60 \pm 15$	$+57 \pm 15$
R_3	-11 ± 14	-9 ± 14
D_1	-1 ± 15	-3 ± 15
D_2	$+28 \pm 15$	-2 ± 15
D_3	$+20 \pm 15$	$+6 \pm 15$
$a_{2,0}^{e}$	$+68 \pm 17$	$+66 \pm 17$
$a_{2,0}^{m}$	$+8 \pm 15$	$+8 \pm 15$
$a_{2,1}^{e,Re}$	$+17 \pm 18$	$+16 \pm 18$
$a_{2,1}^{e,Im}$	-0 ± 19	-1 ± 19
$a_{2,1}^{m,Re}$	$+8 \pm 19$	$+9 \pm 19$
$a_{2,1}^{m,Im}$	$+3 \pm 19$	$+3 \pm 19$
$a_{2,2}^{e,Re}$	$+6 \pm 9$	$+6 \pm 9$
$a_{2,2}^{e,Im}$	$+2 \pm 9$	$+1 \pm 9$
$a_{2,2}^{m,Re}$	$+0 \pm 9$	$+1 \pm 9$
$a_{2,2}^{m,Im}$	-8 ± 9	-8 ± 9

Table 5.25: VSH parameters up to degree 2 between Vie18-GA2015 and Gaia-CRF2.

was reported by the working group, was estimated using data up to 2016. The ICRF3 data set is considerably longer (March 2018). Therefore, the calculation was repeated using this consistent data set and the new value was found to be 5.8 $\mu as/year$ (personal communication David Gordon). This value was used to correct GA.

Xu *et al.* (2013) proposed a GA corrected reference frame, the epoch ICRF, where they would provide source positions at J2000.0 with the addition of apparent proper motions. However, the ICRF3 working group decided to provide their frame corrected to the year 2015.

GA is a systematic effect, which accumulates over the years. Geodetic VLBI is a rather old technique, which means that a very long time series (1979 - now) of data is available. Hence, the effects of GA become noticeable and have to be corrected. Gaia collected all its data in only a couple of years, therefore, it is safe to assume that GA did not have a great impact on Gaia data. With this knowledge, Gaia can be used as a reference and correcting GA should bring the VLBI solution closer to it. A solution was created where the reference time was set to J2015.0 (close to Gaia-CRF2, which is J2015.5); it is called Vie18-GA2015. In Table 5.25 the estimated VSH parameters up to degree 2 are listed. It is evident that correcting GA significantly affects the glide parameters while the other parameters are more or less untouched. This is exactly what is expected, since GA affects the source coordinates in a dipole glide from Galactic Center to anticenter.

The amplitude and direction of the glide can be found in Table 5.26. Comparing this table to Table 5.5 reveals that most of the glide in the Vie18 solution can be explained by GA. Furthermore, the remaining glide direction has a very high formal error in right ascension and

Glide	Vie18-GA2015
Glide Amplitude [$\mu as/year$]	$+7 \pm 15$
Glide RA [deg]	$+215 \pm 217$
Glide DEC [deg]	$+54 \pm 119$

Table 5.26: Glide amplitude and direction of VSH parameters up to degree 2 between Vie18-GA2015 and Gaia-CRF2.

declination, which indicates that the remaining glide does not have a clearly defined direction.

5.2.13 Inflating of formal errors

Formal uncertainties from geodetic VLBI solutions are usually too optimistic. This is because it is assumed that all errors are Gaussian, which does not hold in reality. The solution for this problem is to scale the formal errors. Additionally, a noise floor is added to account for residual scaling errors. For the ICRF3 the scaling factor was agreed to be 1.5 in right ascension and declination. The noise floor was found to be declination dependent. However, it was decided to use one conservative estimate (30 µas) for all sources.

In the solution Vie18-ErrorInflated, the formal uncertainties were inflated as described in Section 3.1.2. Some parameters, such as the D_3 and the $a_{2,0}^e$ parameter, are affected by the inflation of the errors, see Table 5.27. Of course, the inflation of formal errors does not deform the solution but rather decreases the significance of these parameters. It has to be noted here that even though the inflation of formal errors is treated similar to other analyst choices it is not a choice but rather a necessary part of the estimation of a celestial reference frame and has to be conducted to derive realistic errors. Therefore, the inflation of formal errors should always be performed.

Petrov *et al.* (2019) suggests to also scale the uncertainties published in the Gaia DR2, see Chapter 1.8. The second column in Table 5.27 lists the VSH parameters of the scaled Gaia-CRF2 with respect to the Vie18 solution. When scaling the uncertainties from Gaia-CRF2 the D_3 parameter increases, the $a_{2,0}^e$ parameter increases slightly and the formal uncertainties of the VSH are decreased. Scaling the uncertainties of both frames decreases the D_3 and $a_{2,0}^e$ parameter again.

5.3 Combining models and analysis strategies to get closer to Gaia-CRF2

Using the knowledge gained in previous sections one can now choose the parameterization of the ICRF solution in a way that reduces systematic effects between the VLBI celestial reference frame and Gaia-CRF2. However, it has to be noted that uncorrected systematic effects could be hidden in Gaia-CRF2. Nevertheless, in this section the VLBI solution, which fits best to Gaia-CRF2 is elicited. The rotation between Gaia-CRF2 and Vie18 is not a

$[\mu as]$	Vie18	Vie18-ErrorInflated	Vie18 and Gaia-CRF2-ErrorInflated	Vie18-ErrorInflated and Gaia-CRF2-ErrorInflated
R_1	-46 ± 16	-45 ± 16	-41 ± 15	-39 ± 15
R_2	$+60 \pm 15$	$+60 \pm 15$	$+57 \pm 15$	$+57 \pm 14$
R_3	-11 ± 14	-4 ± 14	-18 ± 13	-11 ± 13
D_1	-1 ± 15	-1 ± 15	-0 ± 15	$+0 \pm 14$
D_2	$+28 \pm 15$	$+29 \pm 15$	$+29 \pm 15$	$+30 \pm 14$
D_3	$+20 \pm 15$	$+17 \pm 15$	$+27 \pm 14$	$+21 \pm 14$
$a_{2,0}^{e}$	$+68 \pm 17$	$+61 \pm 17$	$+66 \pm 16$	$+58 \pm 16$
$a_{2,0}^{m}$	$+8 \pm 15$	$+6 \pm 15$	$+9 \pm 15$	$+8 \pm 14$
$a_{2,1}^{e,Re}$	$+17 \pm 18$	$+14 \pm 18$	$+16 \pm 17$	$+16 \pm 17$
$a_{2,1}^{e,Im}$	-0 ± 19	$+1 \pm 19$	$+0 \pm 18$	-1 ± 18
$a_{2,1}^{m,Re}$	$+8 \pm 19$	$+17 \pm 19$	-1 ± 18	$+9 \pm 18$
$a_{2,1}^{m,Im}$	$+3 \pm 19$	$+3 \pm 19$	$+1 \pm 18$	$+3 \pm 18$
$a_{2,2}^{e,Re}$	$+6 \pm 9$	$+6 \pm 9$	$+7 \pm 9$	$+6 \pm 8$
$a_{2,2}^{e,Im}$	$+2 \pm 9$	$+2 \pm 9$	$+3 \pm 8$	$+3 \pm 8$
$a_{2,2}^{m,Re}$	$+0 \pm 9$	$+2 \pm 9$	-2 ± 9	$+0 \pm 9$
$a_{2,2}^{m,Im}$	-8 ± 9	-8 ± 9	-8 ± 9	-8 ± 9

Table 5.27: VSH parameters up to degree 2 between Vie18-ErrorInflated and Gaia-CRF2. In the second column, the Gaia uncertainties were scaled and VSH were calculated with respect to Vie18. In the third column, the uncertainties in both frames were inflated.

property inherent to Gaia-CRF2 since it was merely rotated onto an ICRF3 prototype solution. Hence, the rotation is not considered in the following investigations. First, it was found that using ray-traced delays a priori reduces the $a_{2,0}^{e}$ parameter by about 20 µas, see solution Vie18-RayTrace Section 5.2.3.2. However, at the same time the D_3 parameter was increased by about the same amount. When reading previous sections it becomes evident that the D_3 parameter is rather unstable and affected by many different models and analysis strategies, e.g. absolute constraints on gradients, estimation interval of gradients, ray-traced delays just to name a few. The larger D_3 parameter can be reduced by loosening the absolute constraints on gradients, see solution Vie18-RayTrace-noAbsGradConst Section 5.2.3.2. In order to reduce the D_2 parameter and the remaining D_3 parameter the galactic aberration can be corrected. The VSH of this solution can be found in Table 5.28. Another small effect is the inflation of formal errors. The VSH of the addition of these effects can be found in Table 5.28. Most of the parameters stay the same after the inflation of the errors with the largest deviation for the $a_{2,0}^{e}$ and D_3 parameter. In general, inflating the errors reduces the VSH w.r.t. Gaia-CRF2.

Adding the phase calibration model to this solution does change some of the VSH parameters, see Table 5.29. The largest deviation is 10 µas for the D_1 parameter. However, correcting the systematic due to phase calibration removes this solution further from Gaia-CRF2. Using

$[\mu as]$	Vie18	Vie18-GA2015-RayTrace-noAbsGradConst	Vie18-GA2015-RayTrace-noAbsGradConst-ErrorInflated
R_1	-46 ± 16	-47 ± 16	-46 ± 16
R_2	$+60 \pm 15$	$+57 \pm 15$	$+57 \pm 15$
R_3	-11 ± 14	-2 ± 14	$+5 \pm 13$
D_1	-1 ± 15	-1 ± 15	-1 ± 15
D_2	$+28 \pm 15$	-7 ± 15	-6 ± 15
D_3	$+20 \pm 15$	$+6 \pm 15$	$+2 \pm 15$
$a_{2,0}^{e}$	$+68 \pm 17$	$+43 \pm 16$	$+38 \pm 17$
$a_{2,0}^{m}$	$+8 \pm 15$	$+5 \pm 15$	$+3 \pm 15$
$a_{2,1}^{e,Re}$	$+17 \pm 18$	$+12 \pm 18$	$+11 \pm 18$
$a_{2,1}^{e,Im}$	-0 ± 19	$+2 \pm 18$	$+3 \pm 19$
$a_{2,1}^{m,Re}$	$+8 \pm 19$	$+5 \pm 18$	$+13 \pm 18$
$a_{2,1}^{m,Im}$	$+3 \pm 19$	$+1 \pm 19$	$+2 \pm 19$
$a_{2,2}^{e,Re}$	$+6 \pm 9$	$+8 \pm 9$	$+7 \pm 9$
$a_{2,2}^{e,Im}$	$+2 \pm 9$	$+1 \pm 8$	$+0 \pm 9$
$a_{2,2}^{m,Re}$	$+0 \pm 9$	$+3 \pm 9$	$+4 \pm 9$
$a_{2,2}^{m,Im}$	-8 ± 9	-12 ± 9	-11 ± 9

Table 5.28: VSH parameters up to degree 2 between Vie18-GA2015-RayTrace-noAbsGradConst and Gaia-CRF2.

an elevation dependent weighting scheme in the solution has a noticeable impact on the VSH parameters, see Table 5.29. The weighting was realized with 6 and 12 ps of noise respectively. In general, the elevation dependent weighting increases the VSH parameters between these solutions and Gaia-CRF2. As discussed in Section 5.2.8, adding more noise (12 ps) results in a χ^2/ndf parameter close to unity, which is preferable. Looking at Table 5.29 the solution with more noise added also fits better to Gaia-CRF2.

In order to get a better overview of the different solutions the VSH can be visualized into one plot, see Figure 5.21. Correcting galactic aberration combined with ray-tracing removes most of the deformation, which are present between Gaia-CRF2 and ICRF. Especially, the $a_{2,0}^{e}$ and D_2 parameters are affected by these models/corrections. Further, removing the absolute constraints of gradients results in an insignificant D_3 parameter. The mandatory scaling of formal errors reduces the significance of some of the parameters.

Plotting the VSH of the solution which fits best to Gaia-CRF2, the Vie18-GA2015-RayTrace-noAbsGradConst-ErrorInflated solution, one can see the remaining systematic, see Figure 5.22, 5.23 and 5.24. When comparing these figures to Figure 5.8, 5.9 and 5.10 the change in VSH is immediately visible. While the rotation is more or less the same (largest arrow being $76\mu as$ for Vie18 and $73\mu as$ for Vie18-GA2015-RayTrace-noAbsGradConst-ErrorInflated) the glide and quadrupole parameters are significantly different. The Gaia-CRF2 frame was rotated onto the ICRF3 using common sources. Among these were sources with

$[\mu as]$	Vie18	Vie18-GA2015-RayTrace-noAbsGradConst-PCalHb	Vie18-GA2015-RayTrace-noAbsGradConst-elWeight6ps	Vie18-GA2015-RayTrace-noAbsGradConst-elWeight12ps
R_1	-46 ± 16	-55 ± 16	-55 ± 16	-53 ± 16
R_2	$+60 \pm 15$	$+52 \pm 15$	$+52 \pm 15$	$+57 \pm 16$
R_3	-11 ± 14	-2 ± 14	-2 ± 13	-6 ± 14
D_1	-1 ± 15	-11 ± 15	-11 ± 15	-5 ± 16
D_2	$+28 \pm 15$	-10 ± 15	-10 ± 15	-9 ± 16
D_3	$+20 \pm 15$	-10 ± 14	-10 ± 15	-5 ± 15
$a_{2,0}^{e}$	$+68 \pm 17$	$+48 \pm 16$	$+48 \pm 16$	$+48 \pm 17$
$a_{2,0}^{m}$	$+8 \pm 15$	$+7 \pm 15$	$+7 \pm 15$	$+9 \pm 16$
$a_{2,1}^{e,Re}$	$+17 \pm 18$	$+9 \pm 17$	$+9 \pm 17$	$+12 \pm 18$
$a_{2,1}^{e,Im}$	-0 ± 19	$+4 \pm 18$	$+4 \pm 18$	$+2 \pm 19$
$a_{2,1}^{m,Re}$	$+8 \pm 19$	$+4 \pm 18$	$+4 \pm 18$	$+4 \pm 19$
$a_{2,1}^{m,Im}$	$+3 \pm 19$	-1 ± 18	-1 ± 18	$+2 \pm 19$
$a_{2,2}^{e,Re}$	$+6 \pm 9$	$+7 \pm 9$	$+7 \pm 9$	$+8 \pm 9$
$a_{2,2}^{e,Im}$	$+2 \pm 9$	-1 ± 8	-1 ± 8	-1 ± 9
$a_{2,2}^{m,Re}$	$+0 \pm 9$	$+1 \pm 9$	$+1 \pm 9$	$+1 \pm 9$
$a_{2,2}^{m,Im}$	-8 ± 9	-17 ± 9	-17 ± 9	-15 ± 9

Table 5.29: VSH parameters up to degree 2 between Vie18-GA2015-RayTrace-noAbsGradConst-PCalHb and Gaia-CRF2.
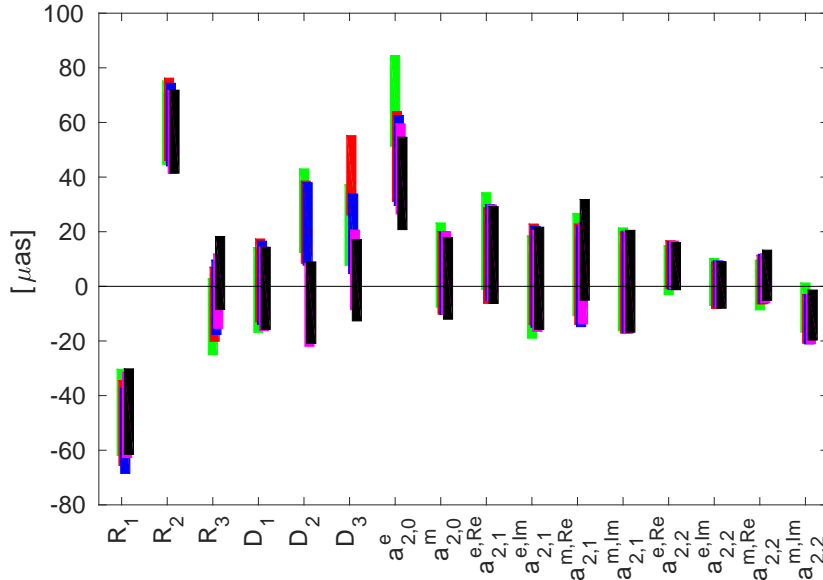
Figure 5.21: Comparison of VSH of different VLBI solutions with Gaia-CRF2. The color code is as follows: green is the Vie18 solution, red is the Vie18-RayTrace solution, blue is the Vie18-RayTrace-noAbsGradConst solution, magenta is the Vie18-GA2015-RayTrace-noAbsGradConst solution and black is the Vie18-GA2015-RayTrace-noAbsGradConst-ErrorInflated solution. The bars indicate the uncertainties of the VSH.

angular separations of many milliarcseconds. Most of these sources were removed during the outlier elimination. Hence, large rotational parameters are the result of the different source selection. The glide becomes insignificant with the largest arrow being of the size of $6\mu as$ versus $36\mu as$ for the Vie18 solution. This means that all the large-scale deformation (degree 1) can be explained by the analysis choices made while constructing the VLBI reference frame. It is important to note here that systematic effects might as well be hidden in the Gaia-CRF2 and choosing models to get closer to it might propagate problems from the Gaia-CRF2 into the ICRF. For the second order parameters the reduction is not as big but still significant with a reduction from $91\mu as$ to $71\mu as$ for the largest arrow in the plot. However, the second order parameters still show significant behavior, which cannot be explained by models and analysis strategies explained in this chapter.
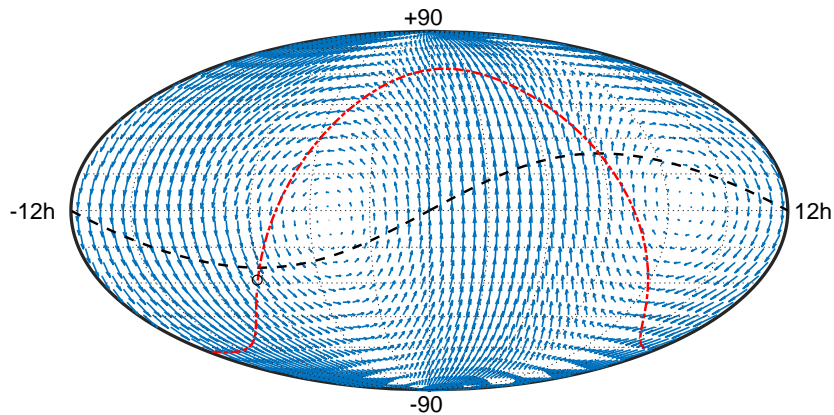
Figure 5.22: Rotation between Vie18-GA2015-RayTrace-noAbsGradConst-ErrorInflated and Gaia-CRF2. The largest arrow is of size $73\mu as$. The galactic plane is depicted in red with the center of the Galaxy denoted as a black circle. The ecliptic is depicted as a black dashed line.
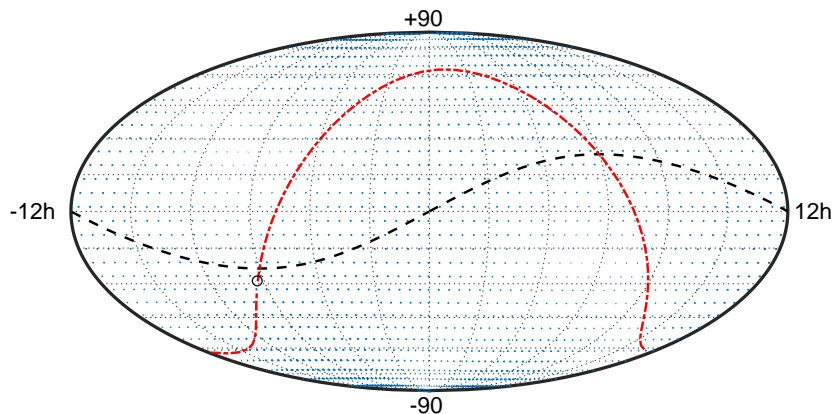
Figure 5.23: Glide between Vie18-GA2015-RayTrace-noAbsGradConst-ErrorInflated and Gaia-CRF2. The largest arrow is of size $6\mu as$. The galactic plane is depicted in red with the center of the Galaxy denoted as a black circle. The ecliptic is depicted as a black dashed line.

A similar comparison can be done using the outlier test proposed by Mignard *et al.* (2016). This was completed and the resulting VSH parameters are summarized in Figure 5.25. The
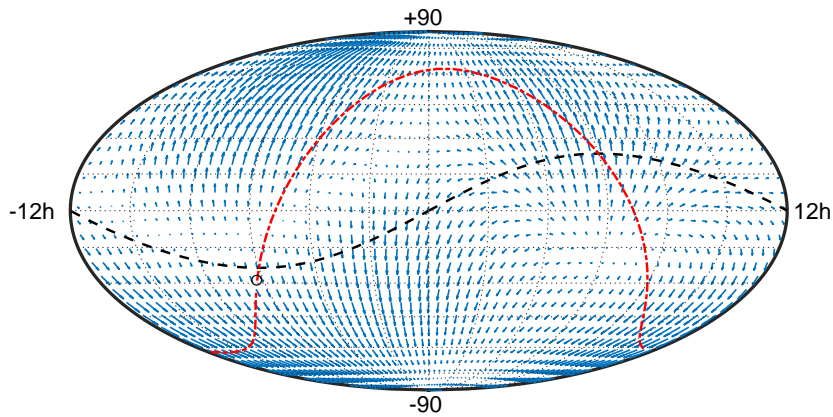
Figure 5.24: VSH parameter up to degree 2 between Vie18-GA2015-RayTrace-noAbsGradConst-ErrorInflated and Gaia-CRF2. The largest arrow is of size $71\mu as$. The galactic plane is depicted in red with the center of the Galaxy denoted as a black circle. The ecliptic is depicted as a black dashed line.

first interesting fact (not seen in the figure) is the number of outliers. While 494 outliers are found for the Vie18 solution, significantly less (445) are found for the Vie18-RayTrace solution. This number then stays the same when loose a priori gradients are used (446) and when GA is corrected (446). Only when the errors are scaled does this number further decrease (366), which is not surprising since the formal uncertainties are increased. This indicates that at least some of the outliers can be explained by insufficient troposphere modeling. Unfortunately, the conclusion which can be drawn from Figure 5.21 cannot be confirmed completely when looking at Figure 5.25. The main differences are:

- The overall magnitude of the differences decreased. This is not surprising since more outliers are removed.

- When ray-traced tropospheric delays are used as a priori the $a^e_{2,0}$ parameter is decreased and the D_3 parameter is increased, which is similar to previous observations, however, at the same time the $a^{e,Im}_{2,1}$ is increased and the $a^{m,Re}_{2,1}$ decreased, which is new.

- The D_2 parameter is affected similarly (by about -30 µas) when GA is corrected, however, since the D_2 parameter is already small to begin with the correction of GA shifts it away from the zero line.

- While the scaling of formal uncertainties does not shift the parameters much in Figure 5.21, it does so in Figure 5.25.

Some of these differences are due to the different set of sources used for the calculation of the VSH. A fairer comparison would be to use one list of outliers for all computations. One possibility would be to fix the list of outliers to the 494 outliers found for the Vie18 solution. The VSH parameters calculated with this fixed list of outliers can be found in Figure 5.26. Generally, the same differences as in Figure 5.25 are found. The only noteworthy difference
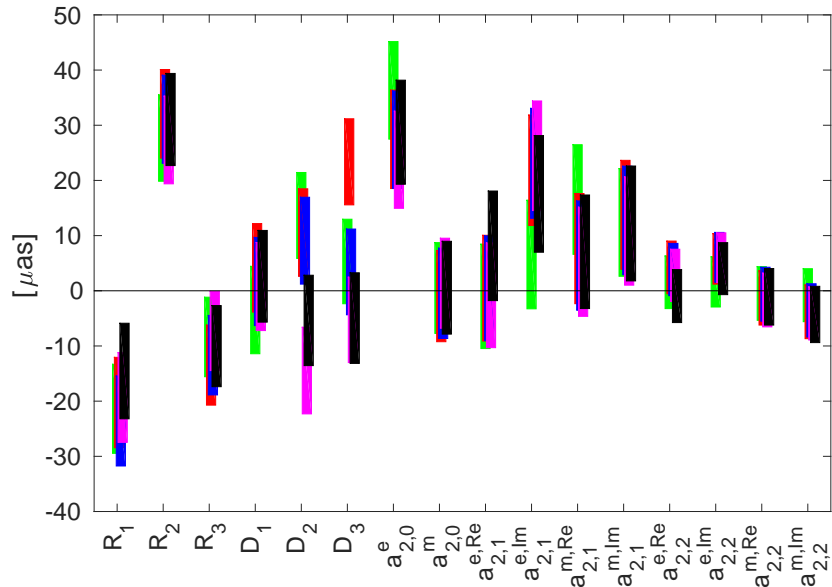
Figure 5.25: Comparison of VSH of different VLBI solutions with Gaia-CRF2. Outliers are removed according to Section 4.2. The color code is as follows: green is the Vie18 solution, red is the Vie18-RayTrace solution, blue is the Vie18-RayTrace-noAbsGradConst solution, magenta is the Vie18-GA2015-RayTrace-noAbsGradConst solution and black is the Vie18-GA2015-RayTrace-noAbsGradConst-ErrorInflated solution. The bars indicate the uncertainties of the VSH.
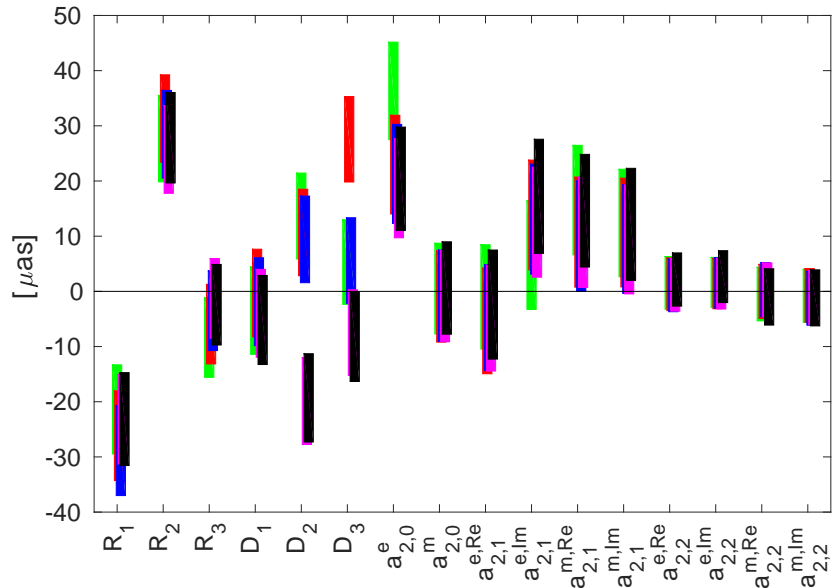
Figure 5.26: Same as Figure 5.25 with different outlier elimination technique. Outliers were found according to Section 4.2 between the Vie18 and Gaia-CRF2 solution. This list of outliers was used for all solutions.

to Figure 5.25 is that the scaling of formal errors does not shift the VSH parameters much any longer.

These differences demonstrate the susceptibility of the VSH estimation on the set of sources used. In general, the conclusion that the deformations of degree 1 can be explained by models

and analysis strategies within the VLBI technique still holds. Further, the $a_{2,0}^e$ parameter stays highly significant no matter which models, analysis strategies or outlier detection methods are used. However, finding the models, which definitely bring the VLBI and Gaia reference frame closer, is much harder, since the VSH are highly affected by the source list used for the comparison.

5.4 Baseline length repeatability

The baseline length repeatability is a good measure to test, if new models or analysis strategies improve results. Baselines between stations are calculated from a number of sessions and then their stability (standard deviation, WRMS etc.) is calculated. If this is done for all baselines and plotted w.r.t. the baseline length the so-called baseline length repeatability plot is derived. It can be assumed that a model, or analysis strategy, which decreases this scatter, also improves the overall solution. The longer a baseline the more variable it is. For the most part this general rule is based on geometry since the longer a baseline the more the height component, which is not as well defined, is reflected by the baseline.

The quality of the baseline length is dependent on the quality of the network. In general, the volume of a network is a good indicator for the reliability of the geodetic results. Therefore, in order to use only the best data available, the 2000 largest (in terms of network volume) sessions were selected from the data set. Baseline lengths were then calculated from this data set. In order to see any effect of the CRF in the baseline length repeatability the source positions have to be fixed. This was realizes by fixing all sources in the available catalog to their a priori values and estimating all other sources as offsets. The results for ICRF2 and Vie18 is depicted in Figure 5.27. Using Vie18 improves the baseline length repeatability very slightly. When Vie18 is used 56.3% of baselines having a smaller repeatability. Using ICRF2 as a priori reference frame results in a smaller repeatability for 29.3% of baselines. The repeatability of 14.4% of baselines remains unchanged. Since the difference between ICRF2 and Vie18 is larger than the difference between the Vie18 solutions, it is safe to assume that the different solutions for Vie18 will not influence the baseline length repeatability significantly.

Figure 5.28 depicts the baseline length repeatability of 2000 sessions where source coordinates are fixed to Gaia-CRF2 and Vie18. Only the 2588 sources which passed the outlier test, see Section 5.1.2, were fixed to Gaia-CRF2 and Vie18 respectively. The Vie18 solution clearly produces a smaller baseline scatter than the Gaia-CRF2. When Vie18 is used 89.6% of baselines are having a smaller repeatability. Using Gaia-CRF2 as a priori reference frame results in a smaller repeatability for 8.3% of baselines. The repeatability of 2.1% of baselines remains unchanged. It is not surprising that the solutions derived from VLBI data fits the VLBI data better. However, the rough impact of using Gaia-CRF2 data for VLBI processing can be assessed with Figure 5.28 with an impact of a couple of millimeters to centimeters on longer baselines.
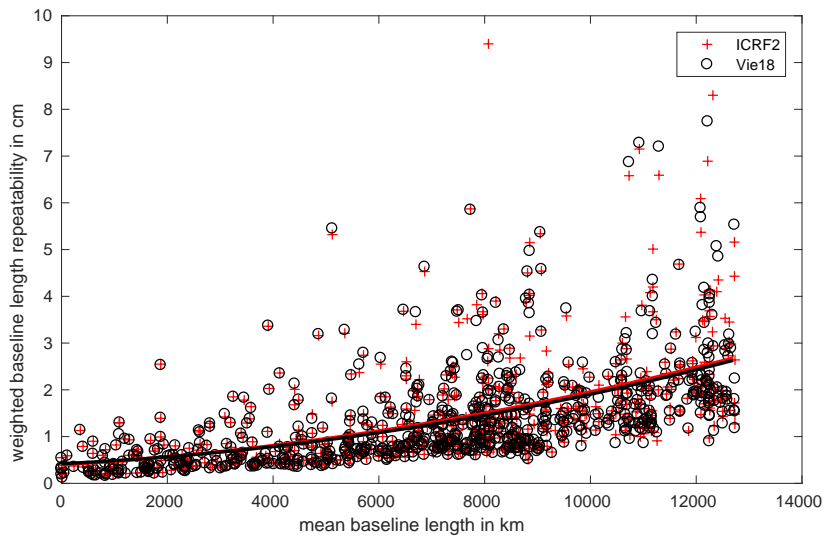
Figure 5.27: Baseline length repeatability when sources are fixed to ICRF2 and Vie18. A subset of the 2000 largest (in terms of volume) sessions was used.
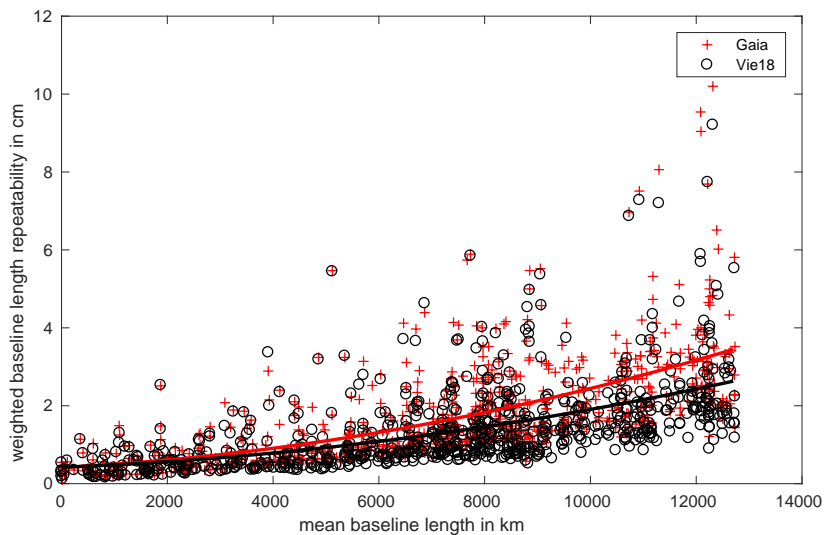
Figure 5.28: Baseline length repeatability when sources are fixed to Gaia-CRF2 and Vie18. Only the 2588 sources, which were not flagged in the outlier test, were fixed. A subset of the 2000 largest (in terms of volume) sessions was used.

5.5   Comparison of official ICRF3 with Gaia-CRF2

The official ICRF3 S/X band solution (from here on called ICRF3sx) was created by the Goddard VLBI group using the Calc/Solve software, see Charlot *et al.* (2018). Generally, the geophysical modeling is the same as for Vie18 with minor differences, e.g. different model for atmospheric pressure loading, different a priori CRF (ICRF2 for Vie18 and gsfc2016a.src for ICRF3sx) etc. For the ICRF3sx the GA was corrected to the year 2015 with 5.8 µas per year. The estimation parameterization is for the most part also similar. Noteworthy differences are:

- the estimation of the EOP, which are estimated differently (offset and rate for polar

$[\mu as]$	ICRF3
R_1	-52 ± 16
R_2	$+59 \pm 16$
R_3	$+6 \pm 14$
D_1	-7 ± 16
D_2	$+5 \pm 15$
D_3	$+9 \pm 15$
$a_{2,0}^{e}$	$+46 \pm 17$
$a_{2,0}^{m}$	$+2 \pm 16$
$a_{2,1}^{e,Re}$	$+10 \pm 18$
$a_{2,1}^{e,Im}$	-2 ± 19
$a_{2,1}^{m,Re}$	$+16 \pm 19$
$a_{2,1}^{m,Im}$	$+2 \pm 19$
$a_{2,2}^{e,Re}$	$+7 \pm 9$
$a_{2,2}^{e,Im}$	$+2 \pm 9$
$a_{2,2}^{m,Re}$	$+1 \pm 9$
$a_{2,2}^{m,Im}$	-12 ± 9

Table 5.30: VSH parameters up to degree 2 between ICRF3sx and Gaia-CRF2.

motion and dUT1 and only offsets for nutation) for ICRF3sx,

- the estimation of the TRF (in ICRF3sx no stations are estimated as arc parameters; some station's nonlinear position variations are modeled using splines; 38 stations are used to set the datum; velocities are fixed, if stations have short data spans),

- other sources were chosen for the NNR datum constraints,

- all sources were estimated as global parameters.

The data weighting procedure differs from the one used for Vie18. In the ICRF3sx the data was weighted with $\frac{1}{\sqrt{f^2+a^2}}$, where f is the uncertainty reported by the fringe fitting process (dependent on the signal to noise ratio) and a is a station dependent parameter which was computed per session such that χ/ndf becomes unity. Formal errors were scaled with a scaling factor of 1.5 and a noise floor of 30 µas.

When the ICRF3sx is compared against Gaia-CRF2 the VSH parameters listed in Table 5.30 are found. For consistency, the list of outlier that was used for the Vienna solutions was applied here as well. A rather good agreement with Gaia-CRF2 is found with the only highly significant parameter (apart from rotations) being the $a_{2,0}^{e}$ parameter.

5.6 Comparison of Vienna solutions with ICRF3

The differences between the Vienna and the ICRF3sx solution can be assessed using VSH. All sources in the Vienna solutions are found in the ICRF3sx solution. Therefore, the number

$[\mu as]$	Vie18	Vie18-GA2015-noSpecialHandling-ICRF3defining-ICRF3apriori-ErrorInflated	Vie18-GA2015-RayTrace-noAbsGradConst-ErrorInflated
R_1	$+7 \pm 1$	$+20 \pm 1$	$+9 \pm 1$
R_2	$+0 \pm 1$	$+1 \pm 1$	-2 ± 1
R_3	-11 ± 1	-7 ± 1	-5 ± 1
D_1	$+5 \pm 1$	$+2 \pm 1$	$+7 \pm 1$
D_2	$+24 \pm 1$	-4 ± 1	-11 ± 1
D_3	$+5 \pm 1$	-10 ± 1	-7 ± 1
$a_{2,0}^{e}$	$+14 \pm 1$	$+13 \pm 1$	-7 ± 1
$a_{2,0}^{m}$	$+1 \pm 1$	$+3 \pm 1$	-1 ± 1
$a_{2,1}^{e,Re}$	$+1 \pm 1$	-1 ± 1	$+0 \pm 1$
$a_{2,1}^{e,Im}$	$+5 \pm 1$	$+5 \pm 1$	$+4 \pm 2$
$a_{2,1}^{m,Re}$	-0 ± 1	$+1 \pm 1$	-2 ± 1
$a_{2,1}^{m,Im}$	$+0 \pm 1$	$+0 \pm 1$	-0 ± 1
$a_{2,2}^{e,Re}$	-1 ± 1	-1 ± 1	-1 ± 1
$a_{2,2}^{e,Im}$	-2 ± 1	-2 ± 1	-1 ± 1
$a_{2,2}^{m,Re}$	$+0 \pm 1$	$+1 \pm 1$	-0 ± 1
$a_{2,2}^{m,Im}$	$+1 \pm 1$	$+1 \pm 1$	-1 ± 1

Table 5.31: VSH parameters up to degree 2 between Vienna solutions and the ICRF3sx.

of intersecting sources is 4482 (4521 when the special handling sources are estimated as global parameters). Median formal errors are found to be on a comparable level with 136 µas and 127 µas in right ascension and 239 µas and 219 µas in declination for Vie18 and ICRF3sx respectively. Outliers were removed according to Section 4.2 with a cutoff threshold of $\chi > 4.3$ which corresponds to the number of intersecting sources. The outlier test revealed one source to be an outlier.

Additionally, two other solutions are investigated, namely Vie18-GA2015-noSpecialHandling-ICRF3defining-ICRF3apriori-ErrorInflated which should be close to the ICRF3sx solution and Vie18-GA2015-RayTrace-noAbsGradConst-ErrorInflated which is the closest solution to the Gaia-CRF2. The deformations between these solutions and the ICRF3sx solutions are small with the maximal deformation being 13 µas. However, when using the new set of defining sources which were used in the ICRF3sx solution, as was done in the Vie18-GA2015-noSpecialHandling-ICRF3defining-ICRF3apriori-ErrorInflated solution a large R_1 parameter of 20 µas is found. The reason for this rather large rotation is that ICRF3sx was rotated onto the ICRS using some of the defining sources of ICRF2. This step is omitted in the Vie18-GA2015-noSpecialHandling-ICRF3defining-ICRF3apriori-ErrorInflated solution, hence, the significant rotations.

Deformations between the Vie18-GA2015-RayTrace-noAbsGradConst-ErrorInflated and

$[\mu as]$	ICRF3k	ICRF3ka
R_1	$+9 \pm 8$	-21 ± 9
R_2	-8 ± 8	-5 ± 9
R_3	-8 ± 4	$+6 \pm 6$
D_1	$+16 \pm 7$	$+1 \pm 8$
D_2	-48 ± 7	-33 ± 8
D_3	-28 ± 8	$+257 \pm 10$
$a_{2,0}^{e}$	$+7 \pm 9$	-59 ± 12
$a_{2,0}^{m}$	$+29 \pm 6$	-151 ± 9
$a_{2,1}^{e,Re}$	$+23 \pm 8$	$+20 \pm 10$
$a_{2,1}^{e,Im}$	$+48 \pm 9$	-11 ± 10
$a_{2,1}^{m,Re}$	-16 ± 8	-3 ± 9
$a_{2,1}^{m,Im}$	$+25 \pm 9$	$+3 \pm 9$
$a_{2,2}^{e,Re}$	$+6 \pm 3$	$+7 \pm 4$
$a_{2,2}^{e,Im}$	$+5 \pm 3$	-1 ± 4
$a_{2,2}^{m,Re}$	-14 ± 4	-0 ± 5
$a_{2,2}^{m,Im}$	-0 ± 4	-7 ± 6

Table 5.32: VSH parameters up to degree 2 between ICRF3 solutions in K and Ka band and Vie18-GA2015-RayTrace-noAbsGradConst-ErrorInflated.

the ICRF3k band solution, see Table 5.32, are generally below 50 µas. In total 765 intersecting sources are found. Using the outlier elimination technique described in Section 4.2 with a threshold of $\chi > 3.9$ 26 outliers are found.

The same procedure was performed with the ICRF3ka band solution, see Table 5.32 for the VSH parameters. For the Ka band solution 614 sources are found. Using the same outlier detection procedure with a threshold of $\chi > 3.8$ 172 outliers are flagged which is a total of 28% of all sources. This number is high when considering that, with a threshold of $\chi > 3.8$ and 614 sources, less than one source should have a statistically significant normalized separation. When looking at Table 5.32 one can see that high systematic deformations are present in the D_3 and $a_{2,0}^{m}$ parameter, which is most likely also the reason for the high number of outliers. Since the VLBI solutions in K and X/S band agree reasonably well and the X/S band solutions agree with Gaia-CRF2 it is most likely that the Ka band solution experiences systematic deformations. The most likely source of this error is the weak network geometry of the Ka band solution.

Chapter 6

Summary and Conclusion

Estimating a celestial reference frame from VLBI data requires the analyst to choose between a large variety of models and estimation parameters. In order to test these choices an external validation is needed. Testing the CRF derived with VLBI was a difficult task in the past, since no independent CRF with comparable accuracy existed. Therefore, the quality of the CRF was evaluated with the aid of its auxiliary products, such as the TRF and EOP. However, with the launch of the Gaia satellite this changed. Although Gaia was designed to observe the Milky Way, it also observes extragalactic sources, such as quasars. A reference frame constructed from quasars is one of the products published by the Gaia Collaboration. Its most recent release is the Gaia-CRF2, which was published within the second data release in April 2018. For the first time in VLBI history, a fully independent realization of the ICRS with comparable accuracy exists. This independent reference frame is the perfect external source to assess systematic effects in the VLBI frame. It has to be noted here that care has to be taken when these reference frames are compared, since they observe in completely different wavelengths. However, systematic effects such as the core shift are believed to change the positions along the jet direction and, since the jet direction is arbitrary, this change in position would result in a larger number of outliers rather than a systematic deformation of the whole frame.

After removing these outliers, one has to decide on the method of comparison. The state of the art tool to compare astrometric catalogs is the vector spherical harmonic decomposition. It uses base function to approximate the vector field, which is the result of subtracting common sources of two astrometric catalogs. The degree of expansion of the VSH can be chosen with large-scale deformations reflected by lower degrees. Since large scale deformations are of interest when looking at systematic differences the expansion is stopped at degree 2. Degree 1 represents a dipole, which can be further divided into a rotation and deformation. The deformation of degree 1 can be described as a flow from a source to a sink and is called glide in the literature. Degree 2 represents a quadrupole.

When comparing the standard CRF solution from the Vienna group, here called Vie18, to the ICRF2 large deformations are found with an amplitude of more than 100 µas. Further,

the $a_{2,0}^e$ parameter of degree 2 was found to be highly significant. A similar comparison can be conducted using the Gaia-CRF2 frame as a reference. The glide between Vie18 and Gaia-CRF2 is much smaller with an amplitude of 36 µas. However, as for ICRF2 the $a_{2,0}^e$ was found to be highly significant. This result indicates that the new realization of the ICRF fits better to the Gaia-CRF2 than to the ICRF2. Consequently, this means that the reported declination bias, is most likely a problem inherent to ICRF2. However, it has to be noted that the $a_{2,0}^e$, which is highly significant, is purely declination dependent, hence, not all declination dependent deformations between the catalogs are resolved.

Using this method of comparison many models and analysis parameters set by the analyst can be tested against Gaia-CRF2. Many of the tested models and parameterizations have small or no influence on the VSH. The models with small impact are the antenna axis offset altitude correction model and using different or no a priori gradients models. The parameterization can be divided into single session analysis and global analysis. Among the analysis options in the single session analysis that do not deformations the frame significantly are the shortening of the sampling interval of the zenith wet delay estimation and changing the clock constraints and estimation interval. When the normal equation system of the global solution is composed, several analysis choices do not affect the deformation of the celestial reference frame. These are the estimation of the antenna axis offsets, changing the strength of the no-net-rotation constraints, using different defining sources, estimating the special handling sources as global parameters and estimating stations seasonal harmonics.

However, it was also found that some of the models and parameterizations significantly affect the VSH between individual solutions and the Gaia-CRF2. A large difference in glide was found when the galactic aberration was estimated or corrected. Correcting the effect of GA from the VLBI data removes most of the glide between the VLBI solution and the Gaia-CRF2. The parameters D_2 and D_3 are affected most.

Ray-tracing was found to have a large impact on the $a_{2,0}^e$ and D_3 parameters. However, the impact is not as clear since ray-tracing succeeds in reducing the $a_{2,0}^e$ parameter significantly while increasing the D_3 parameter at the same time.

The gradient parameterization is another analyst choice that affects the D_3 parameter. Especially, the absolute constraints on gradients have an effect on the D_3 parameter. Loosening the absolute constraints on gradients generally reduces the D_3 parameter. Using a shorter sampling interval has the opposite effect (it increases the D_3 parameter). However, it was found that the sampling interval of gradient estimates has no effect, if the absolute constraints on gradients are loosened at the same time.

A systematic azimuth dependent effect was found in the data of the station Hobart12. It was established that this effect could influence the declination of sources. When a simple model is used to correct for this effect the $a_{2,0}^e$ and D_3 parameters are influenced. Correcting this effect decreases the $a_{2,0}^e$ while the D_3 parameter is increased.

The D_3 parameter can be significantly reduced when elevation dependent noise is used in the analysis. In VieVS the standard value for elevation dependent noise is 6 ps (scaled with

$\frac{1}{\sin e}$). However, it was found that this value is most likely too small, since the overall session fit of the solution increases to 1.7 (0.9 without elevation dependent noise). Therefore, the noise was increased to 12 ps, which results in a session fit of 1.0 with similar results.

Another small effect can be observed when the errors are inflated. When formal uncertainties are inflated the D_3 and $a_{2,0}^e$ become less significant. It has to be noted here that error inflation is a necessary part of the global solution, which is needed to derive realistic uncertainties. Therefore, inflating the errors is not an analyst option but rather a vital part of the analysis.

When looking at the previous paragraphs a couple of conclusions can be drawn. First, the D_3 parameter which is directly connected to the source declination is influenced by many of the modeling and analysis choices. The reason for that is the weak network geometry of the VLBI network, which lacks stations in the Southern Hemisphere, which are needed to collect data of southern sources under high elevation angles. Consequently, this means that the D_3 parameter determined with VLBI is susceptible to systematic effects, which in turn means that the significance of this value is questionable. Second, the only model which succeeds in reducing the D_2 parameter is the galactic aberration. Therefore, it can be concluded that applying the galactic aberration model removes a systematic effect between Gaia-CRF2 and the VLBI solution. Third, using ray-traced delays a priori and using the simple phase calibration model both succeed in reducing the highly significant $a_{2,0}^e$ parameter. However, when both models are used the $a_{2,0}^e$ does not decrease further but rather increases a little. Applying ray-traced delays a priori to decrease the $a_{2,0}^e$ parameter seems to be the better choice since the phase calibration effect is not yet fully understood and the model far from mature.

It is now possible to combine the knowledge gained by the different investigations and create a VLBI CRF, which fits best to the Gaia-CRF2. In order to do this the galactic aberration has to be corrected, ray-traced delays have to be used, the absolute constraints on gradients have to be loosened and, of course, the errors have to be inflated. It was found that adding elevation dependent weighting to the analysis does not change the parameters much. Applying these models and analysis strategies results in a celestial reference frame with an insignificant glide with an amplitude of 6 µas w.r.t. the Gaia-CRF2. Further, the $a_{2,0}^e$ parameter is reduced from 68 µas to 38 µas. However, even though the $a_{2,0}^e$ parameter can be significantly reduced it remains highly significant.

When different outlier elimination schemes are used to calculate the VSH the conclusion from the previous paragraph changes a little. First, ray-tracing affects some other second order parameters as well. Second, the D_2 parameter is small to begin with and the correction of GA makes this parameter negative. This demonstrates the suceptibility of the VSH parameters on the source selection and shows that definitive statements are not possible at this stage. However, it is still possible to conclude that deformations of degree 1 can be removed by changing models and analysis strategies within the VLBI estimation technique. Further, the $a_{2,0}^e$ parameter stays highly significant no matter which models, analysis strategies, outlier

tests are used. This indicates that this is a real difference between the frames. Future work will show, if this difference is inherent to the VLBI reference frame or the Gaia reference frame.

Comparing different Vienna solutions to the ICRF3 reveals that the K and S/X band solution agree reasonably well. However, it can be shown that the Ka band solution suffers from zonal errors on the magnitude of 200 µas. These zonal deformations are most likely due to the limited network geometry of the Ka band observing network.

Chapter 7

Outlook

ICRF3 was published in 2018 and will be the IAU recommended celestial reference frame until a new resolution is passed. In the same year the celestial reference frame derived from Gaia data was published. It is a realization of the ICRS with an accuracy similar to ICRF3. However, the Gaia celestial reference frame has a much higher density than the ICRF3 with 500,000 sources and 4500 sources respectively. Further, the VLBI celestial reference frame is affected by zonal errors, which is likely not the case for the Gaia celestial reference frame. For these reasons, it can be expected that the Gaia frame will be part of the next realization of the ICRS, the ICRF4. However, it is not clear, if ICRF4 will be a Gaia only solution or, if it will be a collection of celestial reference frames in different wavelengths. From a geodesists point of view the second option would be preferable, since high accuracy geodetic VLBI is in need of an accurate celestial reference frames in radio wavelengths, e.g. for the determination of EOP. The reason for this is the fundamentally different way these two techniques work. While Gaia is sensitive to the intensity of the whole galaxy, including host stars, accretion disc etc. the VLBI technique is only sensitive to the most compact structure at the center of the observed galaxy. For various reasons these two positions do not always intersect. Hence, accurate celestial reference frame solutions in radio wavelengths will always be important and improving them is essential for the quest of highest accuracy.

Some effort has been made during the creation of ICRF3 to assess problems, which were identified. First, the uneven distribution of observations of sources was reduced by dedicated observing campaigns such as the VCS-II, see Gordon *et al.* (2016) for more information. These efforts improved the formal uncertainties of many sources tremendously. However, the distribution of observations over sources is far from even. Therefore, continuing such endeavors will be necessary for future releases of VLBI celestial reference frames. Second, the spatial distribution of sources in the far south was improved by dedicated observing programs, see McCallum *et al.* (2017) and the SOAP program[1]. However, more must be done to increase the number of sources in the far south. This includes building new telescopes on the Southern

---

[1]http://astrogeo.org/soap/soap_proposal.pdf

Hemisphere and observing as much as possible to close the gap in data between the north and the south. Third, zonal errors and other systematic effects, such as the declination bias or the effect of galactocentric acceleration, were investigated and corrected. However, as described in this thesis, a systematic difference between the VLBI and Gaia CRF can be observed in the $a_{2,0}^e$ parameter. Finding and describing, possibly correcting, the origin of this systematic effect will prove vital for future releases of the ICRF. Further, strengthening the VLBI CRF in declination direction will result in a less variable D_3 parameter, which will make the VLBI CRF less vulnerable to zonal errors. This can be achieved by observing sources with long north south baselines. Fourth, a new list of defining sources was prepared trying to find the most stable sources while keeping the spatial distribution even. However, some of the sources, which define the ICRF3, are only observed in a couple of sessions. In particular, these sources have to be observed more often to increase the stability of the CRF. Furthermore, for various reasons, some of the defining sources do not have images. This is a problem, since images are used to assess, if the source is point-like. Therefore, observing at least the defining sources with astrometric type sessions should be emphasized in the near future.

Usually, the formal errors of the VLBI CRF solutions must be rescaled in order to derive realistic formal uncertainties. This was done for ICRF3. However, the reason for scaling the solution is an assumption in the beginning of the LSM, which does not correspond to reality, namely, that all errors are Gaussian. This is obviously not the case with temporal and spatial correlations being present. Including these correlations into the stochastic model will result in more realistic formal errors and should, therefore, be included into the various analysis software in the future. In geodetic VLBI, many analysts use a variety of different software to derive the CRF. This should be viewed as a resource, which could be harnessed in future by combining the different solutions to one single combined CRF.

List of Figures

List of Tables

Bibliography

ALTAMIMI, Z., REBISCHUNG, P., MÉTIVIER, L. AND COLLILIEUX, X. (2016). ITRF2014: A new release of the international terrestrial reference frame modeling nonlinear station motions. *Journal of Geophysical Research: Solid Earth*, 121, 6109–6131.

BACHMANN, S., THALLER, D., ROGGENBUCK, O., LÖSLER, M. AND MESSERSCHMITT, L. (2016). IVS contribution to ITRF2014. *Journal of Geodesy*, 90, 631–654.

BEASLEY, A.J., GORDON, D., PECK, A.B. *et al.* (2002). The VLBA Calibrator Survey-VCS1. *The Astrophysical Journal Supplement Series*, 141, 13.

BIZOUARD, C., LAMBERT, S., GATTANO, C., BECKER, O. AND RICHARD, J.Y. (2018). The IERS EOP 14C04 solution for Earth orientation parameters consistent with ITRF 2014. *Journal of Geodesy*, 1–13.

BÖCKMANN, S., ARTZ, T. AND NOTHNAGEL, A. (2010). VLBI terrestrial reference frame contributions to ITRF2008. *Journal of Geodesy*, 84, 201–219.

BÖHM, J., WERL, B. AND SCHUH, H. (2006). Troposphere Mapping Functions for GPS and Very Long Baseline Interferometry from European Centre for Medium-Range Weather Forecasts Operational Analysis Data. *Journal of Geophysical Research: Solid Earth*, 111.

BÖHM, J., BÖHM, S., BOISITS, J. *et al.* (2018). Vienna VLBI and Satellite Software (VieVS) for Geodesy and Astrometry. *Publications of the Astronomical Society of the Pacific*, 130, 1–6.

CAMPBELL, J. (2000). Very Long Baseline Interferometry - a high precision tool for geodesy and astrometry. *Comptes Rendus de l'Académie des Sciences - Series IV - Physics*, 1, 1255 – 1265.

CHARLOT, P. (1990). Radio-source structure in astrometric and geodetic very long baseline interferometry. *The Astronomical Journal*, 99, 1309–1326.

CHARLOT, P., JACOBS, C.S., GORDON, D. *et al.* (2018). The Third Realization of the International Celestial Reference Frame by Very Long Baseline Interferometry. *Astronomy & Astrophysics*, to be submitted.

CONDON, J.J., DARLING, J., KOVALEV, Y.Y. AND PETROV, L. (2017). A Nearly Naked Supermassive Black Hole. *The Astrophysical Journal*, 834, 184.

DELLER, A.T., TINGAY, S.J., BAILES, M. AND WEST, C. (2007). DiFX: A Software Correlator for Very Long Baseline Interferometry Using Multiprocessor Computing Environments. *Publications of the Astronomical Society of the Pacific*, 119, 318.

DELLER, A.T., BRISKEN, W.F., PHILLIPS, C.J. *et al.* (2011). DiFX-2: A More Flexible, Efficient, Robust, and Powerful Software Correlator. *Publications of the Astronomical Society of the Pacific*, 123, 275.

ERIKSSON, D., MACMILLAN, D.S. AND GIPSON, J.M. (2014). Tropospheric delay ray tracing applied in VLBI analysis. *Journal of Geophysical Research: Solid Earth*, 119, 9156–9170.

ESA, ed. (1997). The HIPPARCOS and TYCHO catalogues. Astrometric and photometric star catalogues derived from the ESA HIPPARCOS Space Astrometry Mission. Vol. 1200 of *ESA Special Publication*.

FEY, A.L. AND CHARLOT, P. (1997). VLBA Observations of Radio Reference Frame Sources. II. Astrometric Suitability Based on Observed Structure. *The Astrophysical Journal Supplement Series*, 111, 95–142.

FEY, A.L., BOBOLTZ, D.A., GAUME, R.A., EUBANKS, T.M. AND JOHNSTON, K.J. (2001). Extragalactic Radio Source Selection for Use in Directly Linking Optical Astrometric Observations to the Radio Reference Frame. *The Astronomical Journal*, 121, 1741.

FEY, A.L., GORDON, D., JACOBS, C.S. *et al.* (2015). The Second Realization of the International Celestial Reference Frame by Very Long Baseline Interferometry. *The Astronomical Journal*, 150, 58.

FOMALONT, E.B., PETROV, L., MACMILLAN, D.S., GORDON, D. AND MA, C. (2003). The Second VLBA Calibrator Survey: VCS2. *The Astronomical Journal*, 126, 2562.

FRICKE, W., SCHWAN, H., LEDERLE, T. *et al.* (1988). Fifth fundamental catalogue (FK5). Part 1: The basic fundamental stars. *Veroeffentlichungen des Astronomischen Rechen-Instituts Heidelberg*, 32, 1–106.

FROUARD, J., JOHNSON, M.C., FEY, A., MAKAROV, V.V. AND DORLAND, B.N. (2018). Toward the ICRF3: Astrometric Comparison of the USNO 2016A VLBI Solution with ICRF2 and Gaia DR1. *The Astronomical Journal*, 155, 229.

GAIA COLLABORATION, BROWN, A.G.A., VALLENARI, A. *et al.* (2016a). Gaia Data Release 1 - Summary of the astrometric, photometric, and survey properties. *Astronomy & Astrophysics*, 595, A2.

GAIA COLLABORATION, PRUSTI, T., DE BRUIJNE, J.H.J. *et al.* (2016b). The Gaia mission. *Astronomy & Astrophysics*, 595, A1.

GAIA COLLABORATION, BROWN, A.G.A., VALLENARI, A. *et al.* (2018a). Gaia Data Release 2 - Summary of the contents and survey properties. *Astronomy & Astrophysics*, 616, A1.

GAIA COLLABORATION, MIGNARD, F., KLIONER, S.A. *et al.* (2018b). Gaia Data Release 2 - The celestial reference frame (Gaia-CRF2). *Astronomy & Astrophysics*, 616, A14.

GIPSON, J. (2010). An Introduction to Sked. In D. Behrend and D. Baver, eds., *Proceedings of the IVS 2010 General Meeting*, 77–84.

GORDON, D., JACOBS, C., BEASLEY, A. *et al.* (2016). Second Epoch VLBA Calibrator Survey Observations: VCS-II. *The Astronomical Journal*, 151, 154.

GREISEN, E.W. (2002). AIPS, the VLA, and the VLBA. *Information Handling in Astronomy - Historical Vistas*, 109–125.

GWINN, C.R., EUBANKS, T.M., PYNE, T., BIRKINSHAW, M. AND MATSAKIS, D.N. (1997). Quasar Proper Motions and Low-Frequency Gravitational Waves. *The Astrophysical Journal*, 485, 87–91.

HERRING, T.A., SHAPIRO, I.I., CLARK, T.A. *et al.* (1986). Geodesy by radio interferometry: Evidence for contemporary plate motion. *Journal of Geophysical Research*, 91, 8341–8347.

HOFMEISTER, A. (2016). Determination of path delays in the atmosphere for geodetic VLBI by means of ray-tracing. *PhD thesis at Department f. Geodäsie u. Geoinformation / Höhere Geodäsie, Vienna, Austria*.

HOFMEISTER, A. AND BÖHM, J. (2017). Application of ray-traced tropospheric slant delays to geodetic VLBI analysis. *Journal of Geodesy*, 91, 945–964.

HØG, E. (2017). Astrometric accuracy during the past 2000 years. *ArXiv e-prints*, arXiv:1707.01020.

IAU (1999). Chapter IV: Resolutions of the General Assembly. *Transactions of the International Astronomical Union*, 23, 25–51.

KELLERMANN, K.I. AND MORAN, J.M. (2001). The Development of High-Resolution Imaging in Radio Astronomy. *Annual Review of Astronomy and Astrophysics*, 39, 457–509.

KOVALEV, Y.Y., PETROV, L., FOMALONT, E.B. AND GORDON, D. (2007). The Fifth VLBA Calibrator Survey: VCS5. *The Astronomical Journal*, 133, 1236.

KOVALEV, Y.Y., LOBANOV, A.P., PUSHKAREV, A.B. AND ZENSUS, J.A. (2008). Opacity in compact extragalactic radio sources and its effect on astrophysical and astrometric studies. *Astronomy & Astrophysics*, 483, 759–768.

KOVALEV, Y.Y., PETROV, L. AND PLAVIN, A.V. (2017). VLBI-Gaia offsets favor parsec-scale jet direction in active galactic nuclei. *Astronomy & Astrophysics*, 598, L1.

KRÁSNÁ, H. (2013). Estimation of solid Earth tidal parameters and FCN with VLBI. *PhD thesis at Department f. Geodäsie u. Geoinformation / Höhere Geodäsie, Vienna, Austria*.

KRÁSNÁ, H. AND TITOV, O. (2017). Determining the Galactocentric Acceleration Vector from VLBI and its Impact on the Reference Frames. In R. Haas and E. G., eds., *Proceedings of the 23rd European VLBI Group for Geodesy and Astrometry Working Meeting*, 162–166, May 2017.

KRÁSNÁ, H., MALKIN, Z. AND BÖHM, J. (2015). Non-linear VLBI station motions and their impact on the celestial reference frame and Earth orientation parameters. *Journal of Geodesy*, 89, 1019–1033.

LAMBERT, S. (2014). Comparison of VLBI radio source catalogs. *Astronomy & Astrophysics*, 570, A108.

LANDSKRON, D., HOFMEISTER, A. AND BÖHM, J. (2015). Refined Tropospheric Delay Models for CONT11. In van Dam, T., ed., *REFAG 2014*, 1–5, Springer Berlin Heidelberg, Berlin, Heidelberg.

LINDEGREN, L. AND BASTIAN, U. (2011). Basic principles of scanning space astrometry. *Eas Publications Series*, 45, 109–114.

LINDEGREN, L., LAMMERS, U., HOBBS, D. *et al.* (2012). The astrometric core solution for the Gaia mission - Overview of models, algorithms, and software implementation. *Astronomy & Astrophysics*, 538, A78.

LINDEGREN, L., HERNANDEZ, J., BOMBRUN, A. *et al.* (2018). Gaia Data Release 2 - The astrometric solution. *Astronomy & Astrophysics*, 616, A2.

LIU, N., ZHU, Z. AND LIU, J.C. (2018). Possible systematics in the VLBI catalogs as seen from Gaia. *Astronomy & Astrophysics*, 609, A19.

LOBANOV, A.P. (1998). Ultracompact jets in active galactic nuclei. *Astronomy & Astrophysics*, 330, 79–89.

LOVELL, J.E.J., MCCALLUM, J.N., REID, P.B. *et al.* (2013). The AuScope geodetic VLBI array. *Journal of Geodesy*, 87, 527–538.

MA, C. AND FEISSEL, M., eds. (1997). Definition and realization of the International Celestial Reference System by VLBI astrometry of extragalactic objects. Paris: Central Bureau of IERS - Observatoire de Paris, IERS Technical Note 23.

MA, C., CLARK, T.A., RYAN, J.W. *et al.* (1986). Radio-source positions from VLBI. *The Astronomical Journal*, 92, 1020–1029.

MA, C., ARIAS, E.F., EUBANKS, T.M. *et al.* (1998). The International Celestial Reference Frame as Realized by Very Long Baseline Interferometry. *The Astronomical Journal*, 116, 516–546.

MA, C., ARIAS, E.F., BIANCO, G. *et al.* (2009). The Second Realization of the International Celestial Reference Frame by Very Long Baseline Interferometry. *IERS Technical Note*, 35.

MACMILLAN, D.S. (1995). Atmospheric gradients from very long baseline interferometry observations. *Geophysical Research Letters*, 22, 1041–1044.

MACMILLAN, D.S. (2005). Quasar Apparent Proper Motion Observed by Geodetic VLBI Networks. In J. Romney and M. Reid, eds., *Future Directions in High Resolution Astronomy*, Vol. 340 of *Astronomical Society of the Pacific Conference Series*, 477.

MACMILLAN, D.S. (2014). Determination of Galactic Aberration from VLBI Measurements and Its Effect on VLBI Reference Frames and Earth Orientation Parameters. *AGU Fall Meeting Abstracts*, G21A–0429.

MACMILLAN, D.S. AND MA, C. (1997). Atmospheric gradients and the VLBI terrestrial and celestial reference frames. *Geophysical Research Letters*, 24, 453–456.

MALKIN, Z. (2009). On comparison of the Earth orientation parameters obtained from different VLBI networks and observing programs. *Journal of Geodesy*, 83, 547–556.

MAYER, D., BÖHM, J., COMBRINCK, L., BOTAI, J. AND BÖHM, S. (2014). Importance of the Hartebeesthoek Radio Astronomy Observatory for the VLBI network. *Acta Geodaetica et Geophysica*, 49, 313–325.

MAYER, D., BÖHM, J. AND KRÁSNÁ, H. (2015). Investigation of Earth Orientation Parameters for VLBA Calibrator Survey sessions. In R. Haas and F. Colomer, eds., *Proceedings of the 22nd European VLBI Group for Geodesy and Astrometry Working Meeting*, 193–197.

MAYER, D., BÖHM, J., LOVELL, J. *et al.* (2015). Scheduling Strategies for the AuScope VLBI network. *Vermessung & Geoinformation*, 2+3/2015, 162–168.

MAYER, D., BÖHM, J., KRÁSNÁ, H. AND LANDSKRON, D. (2017). Tropospheric delay modelling and the celestial reference frame at radio wavelengths. *Astronomy & Astrophysics*, 606, A143.

MAYER, D., BÖHM, J., KRÁSNÁ, H. AND MCCALLUM, L. (2017). The influence of phase calibration at the station Hobart12 on the ICRF. In R. Haas and E. G., eds., *Proceedings of the 23rd European VLBI Group for Geodesy and Astrometry Working Meeting*, 177–180.

McCallum, L., Mayer, D., Le Bail, K. *et al.* (2017). Star Scheduling Mode - A New Observing Strategy for Monitoring Weak Southern Radio Sources with the AuScope VLBI Array. *Publications of the Astronomical Society of Australia*, 34, e063.

McCarthy, D. and Petit, G., eds. (2004). IERS Conventions (2003). Frankfurt am Main: Verlag des Bundesamts für Kartographie und Geodäsie, IERS Technical Note No. 32.

McCarthy, D. D., ed. (1996). International Earth Rotation Service (IERS) Annual Report 1995. Observatoire de Paris„ Paris, France.

Mignard, F. and Klioner, S. (2012). Analysis of astrometric catalogues with vector spherical harmonics. *Astronomy & Astrophysics*, 547, A59.

Mignard, F. and Morando, B. (1990). Motion of Celestial bodies, Astrometry and Astronomical Reference Frames. In N. Capitaine, ed., *Proceedings of the Journées 1990, Systèmes de Référence spatio-temporels*, 151.

Mignard, F., Klioner, S., Lindegren, L. *et al.* (2016). Gaia Data Release 1. Reference frame and optical properties of ICRF sources. *Astronomy & Astrophysics*, 595, A5.

Niemeier, W. (2008). Ausgleichungsrechnung: Statistische Auswertemethoden.

Nothnagel, A. (2009). Conventions on thermal expansion modelling of radio telescopes for geodetic and astrometric VLBI. *Journal of Geodesy*, 83, 787–792.

Nothnagel, A., Alef, W., Amagai, J. *et al.* (2015). The IVS data input to ITRF2014. In *GFZ Data Services, Helmoltz Centre, Potsdam, Germany*.

Nothnagel, A., Artz, T., Behrend, D. and Malkin, Z. (2017). International VLBI Service for Geodesy and Astrometry. *Journal of Geodesy*, 91, 711–721.

Pany, A., Böhm, J., MacMillan, D. *et al.* (2011). Monte Carlo simulations of the impact of troposphere, clock and measurement errors on the repeatability of VLBI positions. *Journal of Geodesy*, 85, 39–50.

Perryman, M. (2012). The history of astrometry. *The European Physical Journal H*, 37, 745–792.

Petit, G. and Luzum, B., eds. (2010). IERS Conventions 2010. Frankfurt am Main: Verlag des Bundesamts für Kartographie und Geodäsie, IERS Technical Note No. 36.

Petrachenko, B., Niell, A., Behrend, D. *et al.* (2009). Design Aspects of the VLBI2010 System. Progress Report of the IVS VLBI2010 Committee, June 2009.

Petrov, L. and Boy, J.P. (2004). Study of the atmospheric pressure loading signal in very long baseline interferometry observations. *Journal of Geophysical Research: Solid Earth*, 109.

PETROV, L. AND KOVALEV, Y.Y. (2017). Observational consequences of optical band milliarcsec-scale structure in active galactic nuclei discovered by Gaia. *Monthly Notices of the Royal Astronomical Society*, 471, 3775–3787.

PETROV, L. AND KOVALEV, Y.Y. (2017). On significance of VLBI/Gaia position offsets. *Monthly Notices of the Royal Astronomical Society: Letters*, 467, L71–L75.

PETROV, L., KOVALEV, Y.Y., FOMALONT, E. AND GORDON, D. (2005). The Third VLBA Calibrator Survey: VCS3. *The Astronomical Journal*, 129, 1163.

PETROV, L., KOVALEV, Y.Y., FOMALONT, E.B. AND GORDON, D. (2006). The Fourth VLBA Calibrator Survey: VCS4. *The Astronomical Journal*, 131, 1872.

PETROV, L., KOVALEV, Y.Y., FOMALONT, E.B. AND GORDON, D. (2008). The Sixth VLBA Calibrator Survey: VCS6. *The Astronomical Journal*, 136, 580.

PETROV, L., KOVALEV, Y.Y. AND PLAVIN, A.V. (2019). A quantitative analysis of systematic differences in positions and proper motions of Gaia DR2 with respect to VLBI. *Monthly Notices of the Royal Astronomical Society*, 482, 3023–3031.

PLANK, L., LOVELL, J.E.J., MCCALLUM, J.N. *et al.* (2017). The AUSTRAL VLBI observing program. *Journal of Geodesy*, 91, 803–817.

PLAVIN, A.V., KOVALEV, Y.Y. AND PETROV, L. (2018). Dissecting the AGN disk-jet system with joint VLBI-Gaia analysis. *Astrophyscial Journal Letters*.

ROGERS, A.E.E. (1970). Very Long Baseline Interferometry with Large Effective Bandwidth for Phase-Delay Measurements. *Radio Science*, 5, 1239–1247.

SCHARTNER, M. AND BÖHM, J. (2018). VieSched++: A new Scheduling Tool in VieVS. In *Proceedings of the IVS 2018 General Meeting*.

SCHUH, H. AND BÖHM, J. (2013). *Very Long Baseline Interferometry for Geodesy and Astrometry*, 339–376. Springer Berlin Heidelberg, Berlin, Heidelberg.

SECREST, N.J., DUDIK, R.P., DORLAND, B.N. *et al.* (2015). Identification of 1.4 Million Active Galactic Nuclei in the Mid-Infrared using WISE Data. *The Astrophysical Journal Supplement Series*, 221, 12.

SOJA, B. (2016). Anwendung eines Kalman-Filters in der Auswertung von VLBI-Daten. *PhD thesis at Deutsches GeoForschungsZentrum, Potsdam, Germany*.

SOVERS, O.J., FANSELOW, J.L. AND JACOBS, C.S. (1998). Astrometry and geodesy with radio interferometry: experiments, models, results. *Reviews of Modern Physics*, 70, 1393–1454.

SPICAKOVA, H., PLANK, L., NILSSON, T., BÖHM, J. AND SCHUH, H. (2011). Terrestrial reference frame solution with the Vienna VLBI Software VieVS and implication of tropospheric gradient estimation. In W. Alef, S. Bernhart and A. Nothnagel, eds., *Proceedings of the 20th Meeting of the European VLBI Group for Geodesy and Astronomy*, 118–122.

SUN, J., BÖHM, J., NILSSON, T. *et al.* (2014). New VLBI2010 scheduling strategies and implications on the terrestrial reference frames. *Journal of Geodesy*, 88, 449–461.

THALLER, D. (2008). Inter-technique combination based on homogeneous normal equation systems including station coordinates, Earth orientation and troposphere parameters. *PhD thesis at Technische Universität München, München, Germany*.

TITOV, O. AND KRÁSNÁ, H. (2018). Measurement of the solar system acceleration using the Earth scale factor. *Astronomy & Astrophysics*, 610, A36.

TITOV, O. AND LAMBERT, S. (2013). Improved VLBI measurement of the solar system acceleration. *Astronomy & Astrophysics*, 559, A95.

TITOV, O. AND LAMBERT, S. (2016). Search for the primordial gravitational waves with Very Long Baseline Interferometry. In *Proceedings of the 28th Texas Symposium on Relativistic Astrophysics, Geneva, Switzerland*.

TITOV, O., LAMBERT, S. AND GONTIER, A.M. (2011). VLBI measurement of the secular aberration drift. *Astronomy & Astrophysics*, 529, A91.

WALTER, H.G. AND SOVERS, O.J. (2000). Astrometry of Fundamental Catalogues: The Evolution from Optical to Radio Reference Frames.

WIJAYA, D., BÖHM, J., KARBON, M., KRÁSNÁ, H. AND SCHUH, H. (2013). Atmospheric Pressure Loading. *Atmospheric Effects in Space Geodesy*, 137–157.

XU, M.H., WANG, G.L. AND ZHAO, M. (2012). The solar acceleration obtained by VLBI observations. *Astronomy & Astrophysics*, 544, A135.

XU, M.H., WANG, G.L. AND ZHAO, M. (2013). A new concept of the International Celestial Reference Frame: the epoch ICRF. *Monthly Notices of the Royal Astronomical Society*, 430, 2633–2637.